SUNFLOWER ARRAY ANTENNA FOR MULTI-BEAM SATELLITE APPLICATIONS

Cover Back: ‘Kreis - Kreise’ by Guenther Uecker, Germany, 1967.

SUNFLOWER ARRAY ANTENNA
FOR MULTI-BEAM SATELLITE APPLICATIONS

PROEFSCHRIFT

ter verkrijging van de graad van doctor
aan de Technische Universiteit Delft,
op gezag van de Rector Magnificus Prof. ir. K. C. A. M. Luyben,
voorzitter van het College voor Promoties,
in het openbaar te verdedigen op maandag 10 januari 2011 om 10.00 uur

door

Maria Carolina VIGANÓ

Laurea in Ingegneria delle Telecomunicazioni
Universitá di Ingegneria di Firenze, Firenze, Italia
geboren te Florence, Italië

Dit proefschrift is goedgekeurd door de promotor:
Prof.dr.ir. L.P. Ligthart

copromotor:
Dr. ing. I.E. Lager

Samenstelling promotiecommissie:

Rector Magnificus,	voorzitter
Prof. dr. ir. L. P. Ligthart,	Technische Universiteit Delft, promotor
Dr. ing. I. E. Lager,	Technische Universiteit Delft, copromotor
Prof. G. A. E. Vandenbosch,	Katholique Universiteit Leuven
Prof.dr. P. S. Kildal,	Chalmers University of Technology
Prof. dsc. dr. A. P. Yarovoy,	Technische Universiteit Delft
Dr. G. Toso,	European Space Agency
Dr. Y. Cailloce,	Thales Alenia Space France
Prof. dr. ir. P. M. Van den Berg,	Technische Universiteit Delft, reservelid

Sunflower array antenna for multi-beam satellite applications
Maria Carolina Viganó.

Thesis Delft University of Technology.
With references and with summary in Dutch.

ISBN 978–94–6113–030–3

Subject headings: antenna synthesis techniques, non-uniform array antenna, planar array, satellite antennas, antenna measurements.

Printed by Wohrmann Print Service, The Netherlands

This PhD research has been sponsored by the European Space Agency (ESA ESTEC), Thales Alenia Space France (TAS-F) and the Technical University of Delft (TU Delft). The work has been supervised and coordinated by Giovanni Toso (ESA ESTEC), Cyril Mangenot (ESA ESTEC), Gerard Caille (TAS-F) and Ioan Lager (TU Delft).

To My Family and Friends

Contents

1 Introduction **11**

1.1 Satellite communication: an overview 11

1.2 Lines of research 14

1.3 State of the art 15

1.4 Main achievements 18

1.5 Research framework 19

1.6 General choices and notations in the thesis 21

2 Uniform and nonuniform array antenna: theory **23**

2.1 Antenna definitions and parameters 23

2.1.1 Central frequency and bandwidth 24

2.1.2 Efficiency 24

2.1.3 Antenna mutual coupling 24

2.1.4 Antenna pattern 25

2.1.5 Beamwidth 26

2.1.6 Directivity and gain 27

2.1.7 Polarization 27

2.2 General theory of linear array 28

2.2.1 Uniform linear arrays 30

2.3 General planar array theory 32

2.3.1 Uniform planar arrays 33

2.4 Non uniform Direct Radiating Array 39
2.5 Concluding considerations 40

3 Non-uniform array synthesis techniques 41
3.1 Non-uniform arrays 41
3.2 Genetic Algorithm synthesis technique 42
3.3 Null matching synthesis technique 44
3.4 Perturbative synthesis technique 46
3.5 Auxiliary array function synthesis technique 48
3.6 Concluding considerations 50

4 A deterministic synthesis technique for planar non-uniform arrays 51
4.1 Spirals 51
4.2 Uniform spiral array 53
4.3 Spiral array with density tapering 57
4.3.1 Procedure for the case of apertures populated by identical elements 58
4.3.2 Procedure for the case of apertures populated by differently sized elements 61
4.3.3 Equi-power condition 63
4.4 Numerical validation of the technique 64
4.4.1 Completely filled array - equi-amplitude 65
4.4.2 Non-completely filled array - equi-amplitude 69
4.4.3 Array of hexagonal sub-arrays - equi-amplitude 71
4.4.4 Array of hexagonal sub-arrays - equi-power 75
4.5 Concluding considerations 79

5 Physical validation of the 'sunflower' placement strategy 81
5.1 Experimental setup 82
5.1.1 The choice for the sub-array configuration 82

5.1.2 Manufactured basic sub-array – the tile 84
5.1.3 The mounting panel for measurements 85
5.1.4 Measurement setup 87
5.2 Measurement results 88
5.2.1 Measurement of the tile parameters 88
5.2.2 Radiation pattern measurement results 93
5.3 Sunflower final results 99
5.3.1 Design choices 99
5.3.2 Demonstrator performances 100
5.3.3 Concluding considerations 106

6 Conclusions **107**
6.1 General conclusions and major result 107
6.2 Novelty aspects 109
6.3 Future work 110

Bibliography **113**

A Mission requirements **121**

B Side lobe level and Grating lobe level in uniform lattice arrays **125**
B.1 Grating Lobes 125
B.2 Rectangular lattice array antennas 127
B.3 Triangular lattice array antennas 130
B.4 Hexagonal lattice array antennas 132

C Design and optimization techniques **137**
C.1 Stochastic approaches 137
C.1.1 Simulated Annealing 137
C.1.2 Particle Swarm Optimization 138

C.1.3 Genetic Algorithms 138
C.2 Null matching procedure 141
C.3 Perturbative technique 142
C.4 Array synthesis using the Auxiliary Array Function 143
C.4.1 Auxiliary Array Function 144
C.4.2 Evaluation of the Array Tapering Functions 146

D Spirals: Fermat and Fibonacci spirals **149**

E Taylor amplitude distribution **153**

F Patch design **157**
F.1 Radiator design 157

Chapter 1

Introduction

The need for communication is born with man, and the ways to communicate evolved with him, starting from smoke signals and drums covering some kilometres, to internet and satellite communications connecting the complete Earth. Nowadays, thanks to these developments, some perceptions of distances have to be redefined: for example the time you need to talk or even see a person on the other side of the Earth is now just a few seconds. This space barrier has not been broken down but seriously reduced by the use of satellite communication, changing everybody's' life both in the working and the social environments. In the coming years more and more services will be provided through the satellite network, making space antenna an even more actual and interesting field of research.

1.1 Satellite communication: an overview

Some present and future generations of communication satellites use multiple beam antennas providing down-link and up-link coverages over a field of view for personal communication, and direct broadcast over linguistic areas. High gain, multiple overlapping spot beams, employing both frequency and polarization reuse, will provide the needed coverage. In order to generate high gain spot beams, electrically large antenna apertures are required. These apertures may be generated in different ways, from reflectors to lenses and phased arrays.

Nowadays the preferred choice consists of reflector-based multiple beam antennas adopting, for up and down links, one feed per beam architecture. With this type of configuration, depicted in Fig. 1.1(a), adjacent beams are

generated by different reflectors fed by one or several horns [6]. This leads to three or four reflector antennas for European or CONUS (CONtiguous United States) coverage receive and transmit functions.

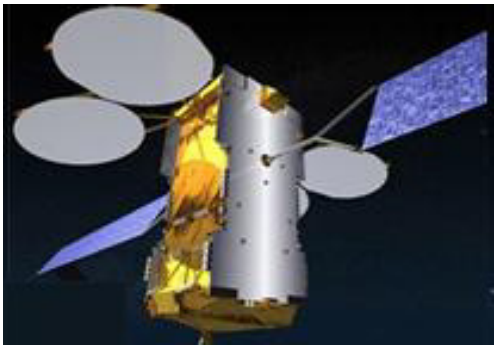

(a) Multi-reflector antenna architecture on board of satellite

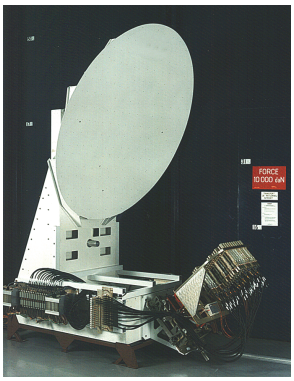

(b) Example of FAFR antenna, courtesy of Thales Alenia Space

Figure 1.1: Most used configurations on board of satellites.

The described multiple-aperture antenna architecture is the one usually implemented since, when a single aperture is used, inter-feed spacing requirements and feed diameter lead to inefficient illumination of the reflector and insufficient performance in terms of isolation levels. The volume required to accommodate the multi reflectors is very large. Moreover the system does not allow for much flexibility in terms of coverage.

A possible solution to generate a multi-beam coverage using a single aperture is the Focal Array Fed Reflector (FAFR) described in [8, 55], (see Fig. 1.1(b)). This concept is based on overlapped beam footprints in the reflector focal plane. This overlapping is performed by connecting individual feeds using a beamforming network, some of these feeds being used for several beams. This antenna concept is quite complex at focal array level but, with limitation on the maximum number of beams, has the advantage to allow the generation of different beams sizes and shapes with only one aperture. An alternative approach based on a single aperture and consisting of overlapping contiguous feeds in a completely radiative way, i.e. without any bulky beamforming network, has been proposed in [7, 9]. Some recent studies have demonstrated that this radiative overlapping is achievable using EBG materials or Fabry-Perot resonators positioned in front of an array [48, 49].

Lately the possibility to exploit active lenses to generate a multiple spot continuous beam coverage has also been investigated [63]. This type of architecture is composed of a first array of radiating elements on one side of the lens, which transmit and receive energy from free space, and a second array located at the back surface, i.e. the surface in front of the feeds. Each radiating element of the back array is connected to the corresponding element of the front array by two coaxial cables of variable length (one for each linear polarization), two attenuators and two high power amplifiers. This type of configuration has been usually discarded for its high volume, weight, deployment issues and thermo-elastic problems.

All mentioned concepts suffer from severe accommodation or implementation difficulties; for example, in the first case discussed (one feed per beam) 3-4 large reflectors area used in transmission and in reception have to be accommodated on board of a satellite and to share the available, reduced space facing the Earth. In the case of employing a FAFR architecture it is possible to avoid using several reflectors but at the expense of a limited number of realizable spot beams and increased complexity of the beamforming network (BFN) . The lens architecture is, as already mentioned, bulky and complicated too. For these reasons it is necessary to investigate, in a long term perspective, solutions based on a single planar aperture that could offer important advantages, especially in terms of costs, mass and spacecraft accommodation.

Phased arrays would be a natural choice to generate multiple beams but they have been often discarded essentially because of their complexity and cost [51]. In transmission, one way to make the array more competitive consists of reducing as much as possible the number of active elements and having all High Power Amplifiers (HPA) operating at the same level, while maintaining under control the main radiative characteristics.

Uniformly spaced antenna arrays have been extensively studied and several methods have already been formulated in order to obtain a desired radiation pattern [14, 69]. All these pattern shaping methods require an amplitude distribution and phase distribution law to be applied to the radiators, resulting in an amplifier and a phase shifter for each array element.

In order to reduce the number of controls, non-uniform arrays can be considered but have not yet received much attention [54, 85]. Non-uniformly spaced arrays will be a major theme in this PhD thesis.

1.2 Lines of research

The aim of this investigation is to identify different array configurations characterized by a reduced complexity and cost with respect to conventional arrays or to reflector configurations, able to satisfy the stringent requirements of a communication mission from GEOstationary satellite, catalogued in Appendix A, and solving some existing problems formulated in Paragraph 1.1. In particular, the PhD thesis will focus on transmit, planar, direct radiating arrays (DRA) with non-uniform element placing and a reduced number of controls. In order to limit the price and to diminish the losses on board of the satellite, the design will aim at minimizing the number of amplifiers. Moreover all amplifiers (driving) the non-uniform configuration will have to operate at the same, optimised point. This last choice has been adopted in such a way to solve some problems and limitations that affect amplifiers on boards of satellites. More in detail, if a configuration using one kind of amplifiers only is selected, in order to create a taper in the amplitude distribution on the aperture, some of the amplifiers would be used not at their optimum operational point, and for this reason some wasted power would be transformed into heat and create additional problems related to the heat dissipation [72]. If, instead, different kinds of amplifiers are used in the array configuration, problems may arise as their behaviour with temperature and also their non-linearities are not the same. For these two reasons, the usage of identical amplifiers working all at the same point is considered of high interest in the satellite antenna community.

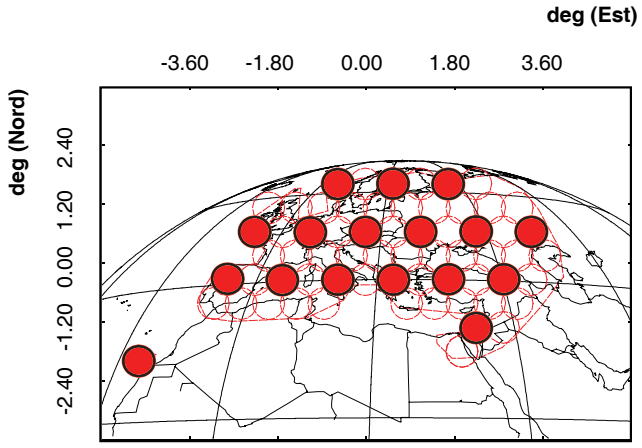

Figure 1.2: European coverage divided into 64 overlapping spots. The circular spots filled with red color represent the areas where the same frequency sub-band is used.

The transmitting antenna under study will have a high EIRP (Effective Isotropic Radiated Power) defined as the amount of power that a theoretical isotropic antenna would emit to produce the peak power density observed in the direction of maximum antenna radiation. The reason for this becomes obvious considering the Friis formulas for transmission [2] (p. 88): this expression clearly evidences that a high EIRP allows for a small receiving effective aperture resulting in an antenna easier to be embedded in a receiving terminal.

Furthermore, in order to improve the system capacity, the frequency band in use has been split into 4 sub-bands and each of them has been used several times according to the scheme in Fig. 1.2, where the red circles represent the spots (out of the total 64 in which Europe is divided in this example) using the same frequency sub-band. To apply this frequency re-use scheme, stringent requirements in terms of inter-beam isolation have to be satisfied.

In order to shape the beam without resorting to an amplitude taper of the amplifier excitations, non-regular lattices have to be considered (see Chapter 2.2). By randomising the element spacing or using unequal subarray sizes and shapes, good results may be achieved [53, 67]. The unequal spacing with a low element density at the array periphery is considered as of major interest for arrays with medium to high number of elements. Besides acting on the element positions, the partition of a complete large array in several sub-arrays could allow reducing the cost of the array antenna. Problems due to the possible grating lobes (GL) appearance or scan-blindness are avoidable thanks to the non-regular spacing, making this array category even more appealing for the application addressed in this thesis.

1.3 State of the art

Sparse array antennas are widely appreciated in the antenna community for several interesting properties. Firstly, even without resorting to an element amplitude taper, it is possible to shape the pattern and control the Side Lobe Level (SLL) by varying in a proper way the position of the radiators. Having all amplifiers working at the same, optimised point will ensure a minimum waste of energy in the transmitting front-end if a configuration with all identical amplifiers is considered. Secondly, as the elements are not deployed on a regular uniform lattice, the GL are spread over a certain region [30], related to the maximum and the minimum spacing, and not concentrated in a particular direction. Thanks to this effect, it is often possible to reduce the number of controls by increasing the average inter-

element distance [54] that, usually, is taken as half the free space wavelength in uniform arrays in order to prevent the appearance of GL in the complete visible space.

In many applications, like for example satellite communication, a reduction of the needed controls is highly desirable (for the impact on cost and weight of the complete structure) and non-uniform arrays are a suitable way to implement such a reduction. Consider, for example, the case of a transmitting DRA for satellite applications. The required main-beam is really narrow, as the dimension of each spot to be covered is extremely small when compared to the distance between the satellite and the Earth. This would naturally lead to a large radiating aperture (see [51] pp.19-21) and, in case of a uniform placement of the elements, would request the usage of more than 900 antennas. In Chapter 4 it will be demonstrated that this figure can be reduced to about 300 if non-uniformly spaced arrays are employed.

Recent design techniques focus on two categories of non-uniform arrays: the ones with non-uniformly spaced elements and the uniformly spaced ones in which some of the elements are selectively switched off or removed from the uniform array. While in the first category, the spacings are not multiples of the same quantity and, for this reason, a large inter-element spacing can be employed while GL appearance may be avoided, for the second category this is not the case. This drawback is compensated by an easier technological implementation and manufacture due to the regular positioning of the elements. Moreover, the mutual coupling effects between the elements are easier to compute and can be taken into account during the simulations in the design phase.

The analysis of unequally spaced antenna arrays originated with the work of Unz [76], who developed a matrix formulation in order to obtain the current distribution necessary to generate a prescribed radiation pattern from an unequally spaced linear array (with prespecified geometry). The synthesis of the positions of space tapered arrays, i.e. non-uniformly spaced arrays, has been studied since the sixties when some of the best works on this topic were presented. Willey [85] analytically derived a space taper equivalent to a given amplitude taper by dividing the aperture in annular rings and integrating the amplitude taper in each of this zones. In this way, he obtained the number of elements to be placed in each annular ring as a fraction of the total number of elements: the radiator percentage in the ring is an approximation of the integral over the considered ring divided by the integral over the complete aperture. The antenna elements are then placed uniformly on a circle inside the corresponding annular region.

The papers from Maffet describe, in a different way, a similar proce-

dure [54], introducing for the first time the concept of 'cumulative current distribution' (see Appendix C).

Tang [71], in the same period, solved the problem of approximating the pattern of an amplitude tapered, uniformly spaced array with a uniformly excited, space tapered array by minimizing the difference between the spatial/amplitude taper distributions of the two. Firstly, the amplitude distribution of a uniform array is expressed as a summation of linear piece-wise terms and then the taper distribution of the non-uniform array is represented as a staircase function, with the bases of the steps replicating the antenna position in the linear array, while the steps heights being taken such that all areas are identical. The difference between the two distributions is finally minimized in order to obtain the antenna element positions.

Other analytical or quasi-analytical methods have been proposed, resulting in a variety of interesting works. One of the possibilities analysed is to express the positions of the non-uniform array antenna elements as the ones of a uniform array plus some perturbation terms [23, 27]. In this way, if these terms are sufficiently small, it is possible to expand the field as a Fourier series and to minimize, with some iterative techniques, the L_2 norm of the difference between the achieved field and the targeted one. The aim of this particular method is the reduction of the SLL in a discrete number of angular directions according to a given reduction law. These algorithms, even if analytic, require some computational time as they resort to iterative solving techniques. Moreover they can only be applied when the distances between the elements are not too different from those in an uniform array, thus excluding the large category of highly non-uniform arrays. Another limitation is that the achieved accuracy in the array synthesis strongly depends on the number of iterations and on the choice of the reduction functions.

Other particular assumptions have been made by Ishimaru and Chen in [30, 31], where by expressing the spacings as a function of the type $x + c\sin(\pi x)$, where x is the element position in the linear array and c is a properly chosen constant value, they were able to compute the field in terms of Anger functions [35].

Most of the recent works on this subject are related to the use of stochastic optimisation [3, 10, 37, 74]. The most used ones, Simulated Annealing (SA), Particle Swarm Optimisation (PSO) and Genetic Algorithms (GA), use natural laws as the minimization of the energetic level, the sharing of information in an animal group and the evolution of a species, respectively, to optimise antenna configurations. All these techniques are able to find the global optimum of a specified objective function, without being trapped in local minima as it may happen with non-stochastic techniques. Such tech-

niques are usually effective in finding the global optimum also in complex problems and are particularly useful if the starting point is sufficiently close to the global optimum solution. Unfortunately, these algorithms are quite time and CPU consuming especially for large array problems characterized by a significant number of unknowns to be optimised. Hence, to overcome this limitation, analytically based approaches are surely to be preferred, especially in the first phase of the optimisation. Some different synthesis techniques, developed in the frame of this investigation, will be introduced in Chapter 3 and then further analysed in Appendix C.

1.4 Main achievements

The main novelties presented in this thesis, are here after summarized:

- *Sunflower antenna positioning law*: a new law for determining the element positions in a non-uniform array antenna has been developed. This *sunflower* non-uniform array is characterized by excellent pattern behaviour and it is recognized as a household name in the international antenna engineering community.
- *Number of controls*: The sunflower array antenna makes use of a strongly reduced number of controls when compared to a classic array antenna with similar pattern behavior. A reduction of the number of active chains of about 70% and 50% was proven possible.
- *Taper function*: In this work it has been proved that element positions, amplitudes, phases and type of elements can contribute to the beam shaping, in a different and predictable way.
- *Synthesis techniques*: Different analytical and non-analytical techniques for the non-uniform antenna array synthesis have been developed (Chapter 3 and in Appendix C) and succesfully applied to satellite communication problems.
- *A truly non-uniform array*: With *sunflower* analytical design technique, the spacing between the elements is truly non-uniform and not, as in other presented methods, the multiple of a basic inter-element distance.
- *Simple one dimensional law*: The particular placement of the elements in a planar array is provided according to two simple independent equations, one for the distance of the elements from the centre and

one for their angles. It has been proved possible to mimick a reference amplitude taper with a reduced computation time.

- *Natural laws*: The concept of optimal angular spreading, inherited from the natural world, has been applied to the sunflower array antenna in order to guarantee the sparsity of the element positions both in the radial and angular coordinates.

- *Efficient antenna aperture usage*: The chosen synthesis technique has been applied to a satellite communication problem and for the first time the formulation for non-uniform radiating arrays has been generalized and used for employing in the same array differently sized sub-arrays, all fed with the same input power. In this way, a better use of the available antenna aperture is possible.

- *Feasibility*: The sub-arrays for the real demonstrator have been implemented, certifying the feasibility of a 'low cost' non-uniform array realized with off the shelf technology. The behaviour of the proposed sub-arrays has been simulated and measured (Chapter 5).

1.5 Research framework

This PhD investigation has been carried out within the frame of a three parties collaborative research effort entitled "Innovative non-uniform array architectures for space applications". The three parties in this scientific undertaking are:

IRCTR (the International Research Centre for Telecommunication and Radar), part of the Faculty of Electrical Engineering, Mathematics and Computer Science of the Delft University of Technology, is a project-driven institute and performs research projects in the field of telecommunications and radar.

ESA and more precisely the European Space Technology and Research Centre (**ESTEC**) is a research organization whose mission is to shape the development of Europes space capability and ensure that investment in space continues to deliver benefits to the citizens of Europe and the world.

Thales Alenia Space **TAS** is a leading European company for satellite systems and orbital infrastructures, involved in both civil and defence sectors.

The dissertation is organized as follows:

- Chapter 2 introduces, from a theoretical point of view, uniform and non-uniform array antennas. The main differences and potentialities of the two are analysed and formulations for both cases are presented.
- Chapter 3 discusses different ways to design non-uniformly spaced arrays. An outline of each technique is given (with more details being included in Appendix C) and some representative results are compared.
- Chapter 4 focuses on a particular non-uniform array, following a characteristic spiral element placement, referred to in this thesis as the 'sunflower array antenna'. To begin with, the uniform 'sparse' array is introduced and the concept of density taper is explained and applied to this particular configuration. The formulation presented takes into account the possibility to design an array populated by differently sized radiators. Some examples of how this techniques has been applied to the design of a non-uniform array antenna for satellite application are shown.
- Chapter 5 provides an overview on the design and manufacturing of the selected sub-array tiles. Measured results concerning the radiated patterns and coupling are presented. Moreover, different ways to group the tiles into sub-arrays are considered and the relevant pattern of the chosen configurations are assessed. In the same chapter the extremely favourable solution obtained by employing the sub-arrays (as studied in Chapter 5) within non-uniform arrays and assembled by means of the synthesis technique described in Chapter 4 is analysed.
- Chapter 6 gives the conclusions about this research and some possible future extensions of this PhD work.
- Appendix A contains the requirements for the satellite communication antenna problem at the core of the "Innovative non-uniform array architectures for space applications" project.
- Appendix B describes the properties of regular arrays; particular attention is given to the GL position, insisting on the formulation presented in Chapter 2.
- In Appendix C a more detailed description of the mathematical formulation used in the design techniques presented in Chapter 3 is given.
- Appendix D provides details on the Fibonacci and Fermat spirals and their properties.

- Appendix E recalls the well-know formulation for the Taylor amplitude distribution in the case of linear and circular arrays.
- In Appendix F the design of the patch used to simulate the complete array performance of some configurations in Chapter 4 is introduced and the patch's behaviour is discussed.

This chapter is now concluded by outlining some general choices, the employed reference system among them, and by summarizing the notational conventions utilized throughout this work on innovative non-uniform array architectures for space applications.

1.6 General choices and notations in the thesis

All examined configurations are considered with respect to a background orthogonal Cartesian reference frame with the origin O and the three mutually perpendicular base vectors $\hat{\boldsymbol{i}}_{\boldsymbol{x}}$, $\hat{\boldsymbol{i}}_{\boldsymbol{y}}$, $\hat{\boldsymbol{i}}_{\boldsymbol{z}}$ of unit length each (see Fig. 1.3). In the indicated order, the base vectors form a right-handed system. Whenever appropriate, vectors are indicated by boldface symbols, with $\boldsymbol{r}$ denoting the position vector

$$\boldsymbol{r} = x\hat{\boldsymbol{i}}_{\boldsymbol{x}} + y\hat{\boldsymbol{i}}_{\boldsymbol{y}} + z\hat{\boldsymbol{i}}_{\boldsymbol{z}} \tag{1.1}$$

of the observation point of coordinates $\{x, y, z\}$. The modulus $r = \mid \boldsymbol{r} \mid$ of the vector $\boldsymbol{r}$ represents the distance (L_2 norm) between the observation point P and the origin O. The time coordinate is denoted as t. For expressing far-field quantities ([2], p. 28), a polar reference frame $Or\theta\phi$ is considered (see Fig. 1.3), with θ ($0^\circ \leqslant \theta \leqslant 180^\circ$) measuring the tilting with respect to the $Oz-$axis, and ϕ ($0^\circ \leqslant \phi < 360^\circ$) measuring the rotation from the $Ox-$axis in the $xOy-$plane. The three mutually perpendicular base vectors $\hat{\boldsymbol{i}}_{\boldsymbol{r}}$, $\hat{\boldsymbol{i}}_{\boldsymbol{\theta}}$, $\hat{\boldsymbol{i}}_{\boldsymbol{\phi}}$ of unit length each form, in this order, a right-handed system, as well. In the course of this work, the θ dependence of certain radiation parameters will be examined in planes defined by the relation $\{(r, \theta, \phi)|\phi = \phi_0\} \cup \{(r, \theta, \phi)|\phi = \phi_0 + 180^\circ\}$, with $\phi_0 < 180^\circ$. These planes will be generically referred to as '$\phi-$cuts' and will be identified by the ϕ_0 value. For simplifying the notation in the plots depicting θ dependencies in arbitrary $\phi-$cuts, the θ coordinate will be conventionally taken to assume negative values in the half-planes where $\phi > 180^\circ$.

Throughout this work, the time dependence will be taken to be time-harmonic, with constant frequency f and angular frequency $\omega = 2\pi f$. All considered problems refer to free-space radiation in which the wave velocity is c_0=299792458 m/s, for which the technical approximation c_0=3 10^8 m/s

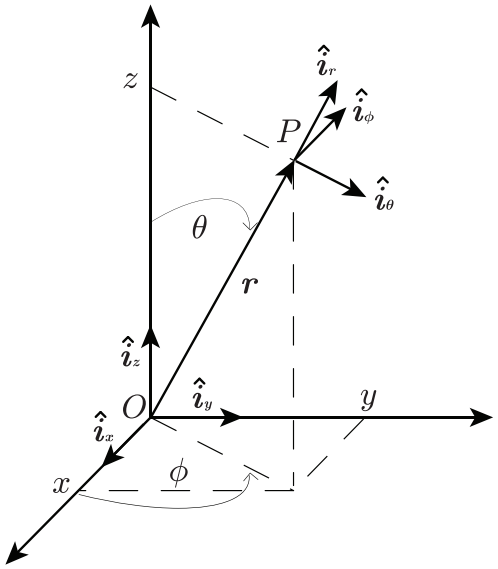

Figure 1.3: Cartesian reference system used in this work.

will be consistently accounted for. In the free-space, the permeability and permittivity are μ_0 and ϵ_0, respectively, with $\mu_0 = 4\pi 10^{-7}$ H/m and $\epsilon_0 = (c_0^2\mu_0)^{-1}$ F/m. The combination of frequency and wave velocity gives rise in the standard way to a wavelength $\lambda = c_0\nu$ m, a propagation constant $k_0 = \frac{\omega}{c_0}$ m^{-1} and a free-space wave impedance $\eta_0 = \sqrt{\frac{\mu_0}{\epsilon_0}} \approx 120\pi\Omega$.

The antenna radiation pattern, a "mathematical function or a graphical representation of the radiation properties of the antenna as function of the space coordinates" [2] (p. 27), is usually subdivided and described in terms of lobes. Two particular regions in the pattern will receive special attention in this work, namely the region of the so-called main lobe, "the radiation lobe containing the direction of maximum radiation", and the region of the sidelobes "the radiation lobes in any direction other than the intended lobe" [2] (p. 31).

When referring to the far field characteristics of an antenna they will always be intended the behaviours of the field in the region where the normalized angular field distribution does not depend anymore on the distance between the antenna and the observation point P in Fig. 1.3 (see [2] p. 35), i.e. for distances

$$|\boldsymbol{r}| \geq \frac{2D^2}{\lambda} \tag{1.2}$$

where D is the antenna aperture dimension. Throughout this analysis, the International System of Units (SI) [70] is used .

Chapter 2

Uniform and nonuniform array antenna: theory

In this chapter some basic notions about antennas and some definitons that will be used throughout this thesis are introduced. Particular emphasis will be placed on the definition of some antenna parameters, particularly useful to have a clear understanding of the requirements applying to the antenna design addressed in this investigation (see Appendix A). In Paragraphs 2.2 and following more concepts and formulas for array antennas, needed for the array synthesis techniques introduced in Chapter 4, will be discussed.

2.1 Antenna definitions and parameters

An antenna is a device reciprocally translating conducted and radiated electromagnetic energy: it converts circuit currents into propagating electromagnetic waves and, by reciprocity, collects power from electromagnetic waves and converts it into circuit currents [58]. The term antenna was used to indicate this transducer for the first time in 1895 by Guglielmo Marconi when, during one of his first tests on wireless communications on the Mont Blanc, he tried to use as transmitting and receiving device a long wire attached to a pole, referred to in Italian as *antenna*. The radiation of an antenna conforms, as any electromagnetic phenomenon, to the well-known Maxwell's equations [57]. While these equations provide a general, comprehensive description of the behaviour of this device, over the years a series of synthetic parameters have been introduced in order to provide practical handles useful to describe the antenna performances and capabilities.

Hereafter some of the most commonly used parameters are introduced, starting with the ones related to the circuit characteristic of the device and following with the parameters expressing the radiation antenna behaviour.

2.1.1 Central frequency and bandwidth

An antenna is usually designed to work at a specific frequency, denoted as *central frequency* or, more generally, in a frequency range constituting its operational *bandwidth*. In this bandwidth, the main radiative characteristic of the antenna are supposed to satisfy specified criteria (usually in terms of reflection coefficient and pattern). Antennas are frequently classified according to their bandwidth into narrowband, broadband and frequency-independent antennas. The first ones are used when it is important to realize stable long-range communication, e.g. in satellite communication, . The second ones, spreading the transmitted information over a large bandwidth and allowing for high value of range resolution are mainly used for short range wireless communication [65] and high resolution and ground penetrating radars [13]. The last category of antennas is mainly used as feeds for reflectors and lenses and for surveillance of the frequency spectrum.

2.1.2 Efficiency

The antenna *efficiency* η is a quality factor of the radiator and represents how much of the input power P_{in} is effectively radiated P_{rad} [38], namely

$$\eta = \frac{P_{\text{rad}}}{P_{\text{in}}}. \tag{2.1}$$

The losses, always present and not allowing for $\eta = 100\%$, are mainly due to possible mismatching between the feeding line and the antenna, internal losses in the antenna or, in the case of having more than one radiator to mutual coupling.

2.1.3 Antenna mutual coupling

When several radiators are placed in (close) proximity, a part of the field radiated by each element is captured by its neighbours, a phenomenon referred to as antenna *coupling*. A quantitative measure of this parameter, in case of N individual radiators, can be expressed as

$$C_{m,n} = \frac{P_{\text{in},n}}{P_{\text{out},m}} \text{ for m,n = 1, 2, ..., N} \tag{2.2}$$

where, considering the case in which only the m^{th} antenna is transmitting and all the other ones are closed on matched loads, $P_{\text{out},m}$ is the power that feed the m^{th} antenna and $P_{\text{in},n}$ is the power measured on the matched load connected to the n^{th} antenna. The total effect due to all antennas constituting the array is quantified by collecting the $C_{n,m}$ coefficients in the so-called scattering matrix [22].

While being relatively easy to be measured, the antenna coupling is not easy to be predicted. It depends on several parameters such as: the antenna type, the relative positioning of the elements and in which way the elements are fed [2] (p. 478). An even more accurate description of this phenomenon can be provided by considering the decoupling efficiency of the different antennas in the array environment [38, 21]. In order to simplify the simulations and the design of antennas composed of several elements, the mutual coupling between the radiators is frequently neglected. This simplification, resulting in the computation of the total radiated field as the superposition of the field of each single element, can be implemented only if the values of the mutual coupling are sufficiently low. In all other cases, usually where the element spacing are less or equal to $\lambda/2$ (see [39] and [33]) this simplification would lead to the calculation of a radiation pattern quite different from the real (measured) one. More in details, usually the coupling between antennas in a system composed of different elements is a phenomenon that deteriorates the expected radiation pattern or, more in general, changes it in a not easily predictable way.

Different techniques to reduce the mutual coupling have been developed in the last years. The most frequently used methods involve procedures to isolate every antenna element from the others and then use, in the total array simulation, the radiation properties measured or computed without the influence from the other antennas. When baffles or absorbers between the antennas are introduced [59], only a reduced scanning of the beam can be performed. For printed technology, solutions resorting to cavities are usually preferred. These cavities may be generated by either metallized holes around the radiating elements (usually referred to as vias) or for example by real metal shielding [52]. This second option will be used in this investigation and will better exploited in Chapter 5.

2.1.4 Antenna pattern

As already mentioned, electromagnetic radiation is described by the Maxwell equations [57]. Under the assumption of free-space, far field approximation,

the electric and magnetic field strenghts are related as

$$\frac{\boldsymbol{E}}{\eta_0} = \boldsymbol{H} \times \boldsymbol{i_r} \tag{2.3}$$

where E and H represent the electric and magnetic fields respectively. The electric field of an antenna deployed on the $xOy-$plane and composed of N radiators, under the hypothesis of no mutual coupling, can be expressed as

$$E(r,\theta,\phi) = -\mathrm{j}\omega\mu_0 \sum_{n=1}^{N} I_n f_n(\theta,\phi) \frac{\exp\left(\mathrm{j}k_0 \boldsymbol{r}\cdot\boldsymbol{d_n}\right)}{4\pi r} \tag{2.4}$$

where I_n represents the excitation of the n^{th} radiator, $f_n(\theta,\phi)$ is the Element Factor expressing the behaviour of the individual n^{th} radiator, and $\boldsymbol{d_n}$ is the vector describing the position of the n^{th} radiator with respect to the origin O. When all radiators composing the antenna are identical the expression in (2.4) is usually factored as

$$\begin{aligned} E(r,\theta,\phi) = &-\mathrm{j}\omega\mu_0 \frac{\exp\left(\mathrm{j}k_0 r\right)}{4\pi r} \tilde{f}(\theta,\phi) \\ &\sum_{n=1}^{N} I_n \exp\left\{\mathrm{j}k_0\left[x\sin(\theta)\cos(\phi) + y\sin(\theta)\sin(\phi)\right]\right\} \end{aligned} \tag{2.5}$$

the first term accounting for the free-space (wave) propagation, the second $\tilde{f}(\theta,\phi)$ term describing the (isolated) element radiation pattern and the last one, termed as Array Factor, reflecting the radiation properties due to the positions and alimentation of the several elements composing the antenna. All examples in this work will be confined to the product of the last two terms in (2.5), an expression that is referred to as the *antenna pattern*.

2.1.5 Beamwidth

With the term *beamwidth* it is usually described the angular distance between two points on the pattern. This vague definition may lead to misunderstandings and it is important, for this reason, to specify which points are referred to, using for example the term Half-Power BeamWidth (HPBW) or First-Nulls BeamWidth (FNBW). These two are the angular distances, measured in a plane containing the maximum of the main beam, between the two points at which the radiation intensity is half of the maximum one and the angular distance between the first two nulls enclosing the main beam, respectively.

2.1.6 Directivity and gain

The *directivity* $D(\theta, \phi)$ of an antenna is defined as the ratio between the radiation intensity $U(\theta, \phi)$ in a given direction (θ, ϕ) and the radiation intensity averaged over all directions.

It can also be equivalently defined as the ratio between the power density that the antenna radiates in a direction and the power density radiated by an ideal isotropic antenna radiating the same total power. It means that

$$\mathcal{D}(\theta, \phi) = \frac{4\pi U(\theta, \phi)}{P_{rad}(\theta, \phi)} = 4\pi \frac{U(\theta, \phi)}{\int_{\Omega} U(\theta, \phi) d\Omega} \tag{2.6}$$

where Ω is the solid angle defined as in [2] (p. 38).

Under the far-field assumption, the electromagnetic wave transmitted (or received) by the antenna can be considered as a uniform plane wave. In this case the electric field $\boldsymbol{E}(\theta, \phi)$ and the magnetic field $\boldsymbol{H}(\theta, \phi)$ are perpendicular and the ratio between their modulus is equal to the characteristic impedence of the medium in which the wave is propagating, as already presented in (2.3). Then it is possible to write the directivity as

$$\mathcal{D}(\theta, \phi) = \frac{4\pi E(\theta, \phi)^2}{\int_{\Omega} E(\theta, \phi)^2 d\Omega} \tag{2.7}$$

The *gain* parameter $\mathcal{G}(\theta, \phi)$ is similar to the directivity [58] but it takes into account the efficiency of the antenna considered.

$$\mathcal{G}(\theta, \phi) = \eta \mathcal{D}(\theta, \phi) \tag{2.8}$$

A more precise definition of this function, would lead to the definition of three different gain function [87]

2.1.7 Polarization

With the term *polarization* of an antenna it is usually indicated a feature that is put in correspondence with the apparent temporal rotation of the representative electric field vector due to the time-harmonic variation of its two orthogonal components E_x and E_y (see Fig. 2.1). Depending on the amplitude of the two components and their phase shift, the end point of the vector describes an elliptic trajectory. Two polarization states are

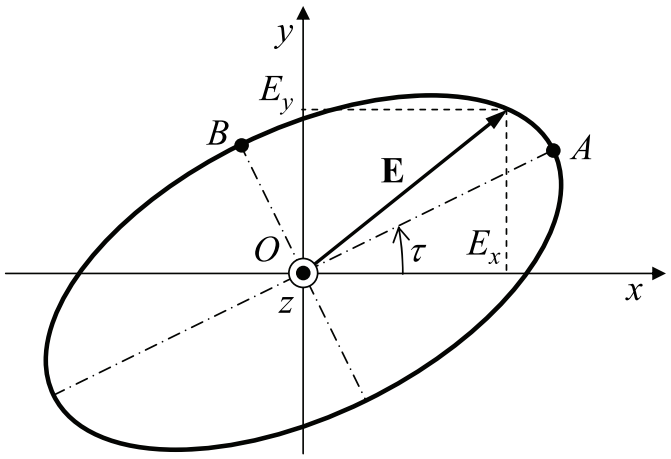

Figure 2.1: Polarization ellipse.

of particular interest. The first refers to the case when the electric field components have equal amplitudes and are shifted in quadrature in time. In this case, the polarization ellipse becomes a circle, the vector rotating clockwise when E_y is shifted 90° ahead - the so-called Right Hand Circular Polarization (RHCP) - or anti-clockwise when that component is shifted 90° behind - the so-called Left Hand Circular Polarization (LHCP) [2]. The second important (remarkable) polarization state corresponds to the linear polarization case when the two components are in phase. In this case, the polarization ellipse becomes a line segment, the angle τ being determined by the ratio between E_x and E_y.

The polarization parameter is usually constant for angle directions within the main beam but it can significantly change in the secondary lobes region.

2.2 General theory of linear array

An array antenna can be defined as a collection of individual elements in which the location and feeding are properly selected such that to enforce a desired far field pattern. Usually, array antennas are used when it is important to have a directive beam and, at the same time, suppress the radiation in other directions [50].

Array antennas were not extensively used in the past due their difficult feeding network and costly implementation. Nevertheless, present day tech-

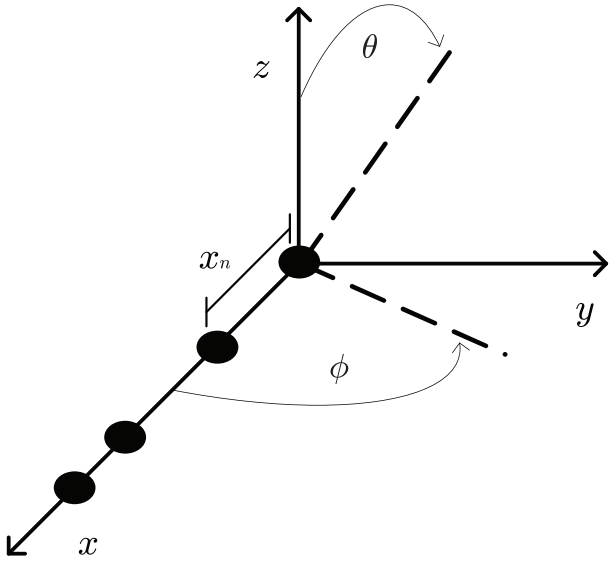

Figure 2.2: Example of linear array.

nology advancements render this category of antennas a suitable alternative to other more common antenna choices. One of the classes of applications where array antennas are particularly adequate is that concerning the systems requiring both beam shaping and beam scanning. In that case the electronic phase shifting allows for scanning the beam devoid of a mechanical movement of the antenna. This class of antenna front-ends are frequently encountered in radar applications and, increasingly, in space platforms where mechanical movement is to be avoided.

Linear arrays are antenna configurations in which the elements are deployed along a straight line (see Fig. 2.2).

The linear array architecture allows for the control of the radiation pattern in planes containing the Ox axis, only, the field distribution in planes parallel to yOz being determined by the element pattern. This limitation can be overcome by resorting to planar arrays that provide full control over the complete space (over a full hemisphere in the case of uni-directional radiation), as it will be demonstrated in Paragraph 2.3.

The far field radiated in the free space from a linear array composed by N elements can be written as

$$E(\theta,\phi) = \sum_{n=0}^{N-1} I_n f_n(\theta,\phi) \exp\left[\mathrm{j}k_0 \sin(\theta)\ x_n\right] \tag{2.9}$$

x_n represents the x coordinate of the n^{th} element, the term $f_n(\theta, \phi)$ represents its element factor and I_n is a complex number accounting for its feeding as

$$I_n = a_n \exp(\mathrm{j}\alpha_n) \tag{2.10}$$

When $\alpha_n = 0$ for $n = 1,...N$, the array pattern points at boresight ($\theta = 0°$); more in general if their values are equal to $\alpha_n = -kx_n \sin(\beta)$, where β is a preferred pointing direction, then the all antennas contributions are summing up coherently in that particular direction β [2] (p. 267). The quantities a_n, α_n, and x_n are variables that can be optimized in order to obtain a radiation pattern able to satisfy given directional requirements.

Hereafter the particular case of the antenna elements being equally spaced is discussed in detail.

2.2.1 Uniform linear arrays

When the antenna elements used are identical and the coordinates x_n are multiple of a constant spacing $d_n = n\tilde{d_x}$, as shown in Fig. 2.3, Eq. (2.9) becomes

$$E(\theta, \phi) = \sum_{n=0}^{N-1} f_n(\theta, \phi) \exp\left[\mathrm{j}k_0 n\tilde{d_x} \sin(\theta)\right] \tag{2.11}$$

Uniform linear array: directivity

In a generic linear array the maximum directivity $\mathcal{D}_M$ of the array is derived from Eq. (2.6). In the case of identical radiators in a phased array pinting at boresight, it can be expressed as ([51] at p. 79)

$$\mathcal{D}_M = \frac{\left|\sum_{n=1}^{N} a_n\right|^2}{\sum_{n=1}^{N}\sum_{m=1}^{N} a_n a_m \exp\left[\mathrm{j}(\alpha_n - \alpha_m)\right] \operatorname{sinc}\left[k(x_n - x_m)\right]} \mathcal{D}_{M_{\text{elem}}} \tag{2.12}$$

where $\mathcal{D}_{M_{\text{elem}}}$ is the maximum directivity of the single radiators. Sometimes this last term is not taken into account in the formulation regarding the array theory as it is related to the element radiative properties and not to

the array. If these identical antenna elements are also equi-spaced, then (2.12) reduces to the well know expression

$$\mathcal{D}_M = \frac{\left|\sum_{n=1}^{N} a_n\right|^2}{\sum_{n=1}^{N} a_n^2} \mathcal{D}_{M_{\text{elem}}} \tag{2.13}$$

and furthermore for equi-fed element $a_n = 1$ [17] (p. 155)

$$\mathcal{D}_M = N\mathcal{D}_{M_{\text{elem}}} = \frac{2D}{\lambda}\mathcal{D}_{M_{\text{elem}}} \tag{2.14}$$

where D is total array length.

In this case the first (highest) SLL associated to the pattern in planes containing the Ox axis is equal to $13.2\,dB$ under the maximum value (see [51] at p. 20).

Uniform linear array: grating lobes

Depending on the choice of $\tilde{d}_x$ and assuming isotropic radiating elements one or more side lobes, as high as the main one, can appear in the visible

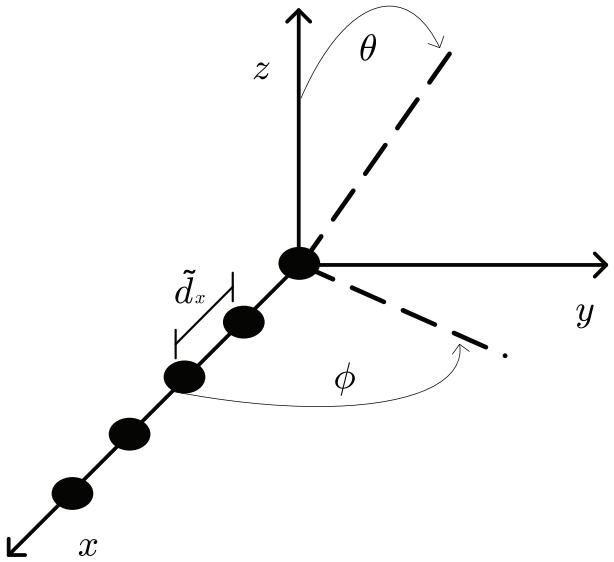

Figure 2.3: Example of linear uniform array.

space: This is due to the electromagnetic waves radiated from each antenna element adding up in phase at several angles, depending on the argument of the exponential in (2.11). The angles at which these copies of the main lobe occur are usually referred to as Grating Lobe (GL) angles [22].

Upon assuming that the main beam points in the direction θ_0, the GL occur at angles θ_{GL} [22]

$$\frac{\tilde{d_x}}{\lambda} = \frac{p}{\sin\theta_0 - \sin\theta_{GL}} \quad p = \pm 1, \pm 2, \ldots \; . \tag{2.15}$$

By accounting for the fact that the absolute value of the sine function is bounded up by 1, (2.15) indicates that no GL is generated as long as $\tilde{d_x} \leq \frac{\lambda}{2}$.

Alternatively, when a spacing $\tilde{d_x} = \lambda$ is chosen, grating lobes will appear at $\theta = 90^\circ$ when the main beam is pointing at boresight. For a more detailed description of the GL angles, see Appendix B.

According to the requirements for antenna beam scanning, it is clear that a proper element spacing has to be selected in order to avoid the GL occurrence.

2.3 General planar array theory

As already mentioned in the previous section, planar arrays are useful to address more general antenna problems where the pattern needs to be shaped and controlled in the complete visible space.

In order to describe the radiative properties of a planar array (see Fig. 2.4), it is convenient to use polar coordinates, with the polar axis normal to the plane containing the array, as already stated in Paragraph 1.6.

The general expression for the far-field generated by N antenna elements and measured on a sphere of constant radius can be expressed, assuming no mutual coupling, in a similar way to that employed for linear arrays as

$$E(\theta, \phi) = \sum_{n=0}^{N-1} I_n f_n(\theta, \phi) \exp\left[\mathrm{j}k \sin(\theta)\ \boldsymbol{d_n} \cdot \boldsymbol{r}\right] \tag{2.16}$$

where, with reference to Fig. 2.4, $\boldsymbol{d_n}$ represents the position of the n^{th} element with respect to the origin O, and I_n is, as in (2.10), a complex number representing the current fed to the n^{th} antenna element.

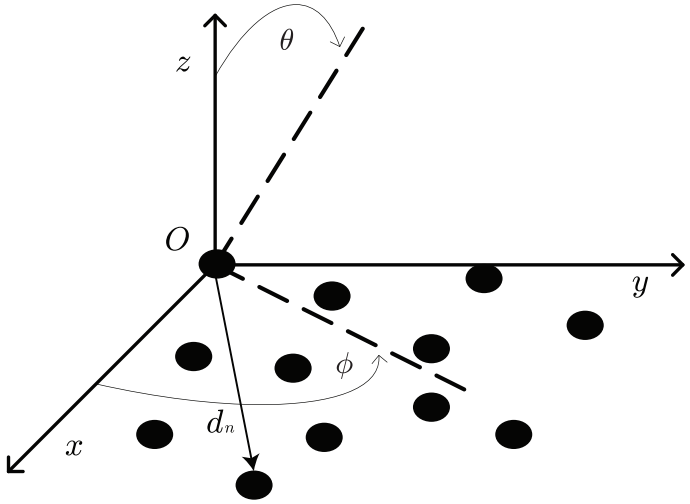

Figure 2.4: Example of a generic planar array.

Usually the term $f_n(\theta, \phi)$, representing the element factor of the n^{th} antenna, is considered constant for all array elements, resulting in a simpler formulation

$$E(\theta,\phi) = \tilde{f}(\theta,\phi) \sum_{n=0}^{N-1} I_n \exp\left[\mathrm{j}k\sin(\theta)\ (x_n\cos(\phi) + y_n\sin(\phi))\right]$$
$$= \tilde{f}(\theta,\phi) AF(\theta,\phi) \tag{2.17}$$

where x_n and y_n are the projections of $\boldsymbol{d_n}$ along the Ox axis and Oy axis respectively, the term AF indicates the Array Factor and takes into account all radiative properties that depend on excitation and element location (see Paragraph 1.6). For sake of completeness and since in this PhD investigation several different elements will be considered in the same array, the formulation used in this thesis will include the Element Factor f_n in the summation as depending on index n.

2.3.1 Uniform planar arrays

In most of the cases studied thus far in literature, [14, 43, 68, 69] the pattern shaping was done by applying properly chosen amplitudes and relative phases to the array antenna elements. In these cases the elements are deployed on a linear or planar, "regular" lattice, with the attribute "regular" indicating that the lattice is chosen such that the element locations partition the antenna surface into identical regular polygonal cells. Only three

regular polygons can ensure a complete, uniform sub-division of the antenna surface [12, 81], namely squares, equilateral triangles and hexagons that lead to square, hexagonal and triangular lattices, respectively. The nodes of the lattices are located at the centers of the relevant polygons.

Hereafter, a short description of the radiative properties of rectangular (as extension of the square lattice), triangular and hexagonal lattice arrays will follow. For a more detailed analysis see Appendix B.

Rectangular lattice, uniform arrays

The most frequently used planar array layout is the one where the elements are deployed on a regular grid of perpendicular lines (see Fig. 2.5). In this case, the n^{th} element distance from the origin, d_n, can be expressed as

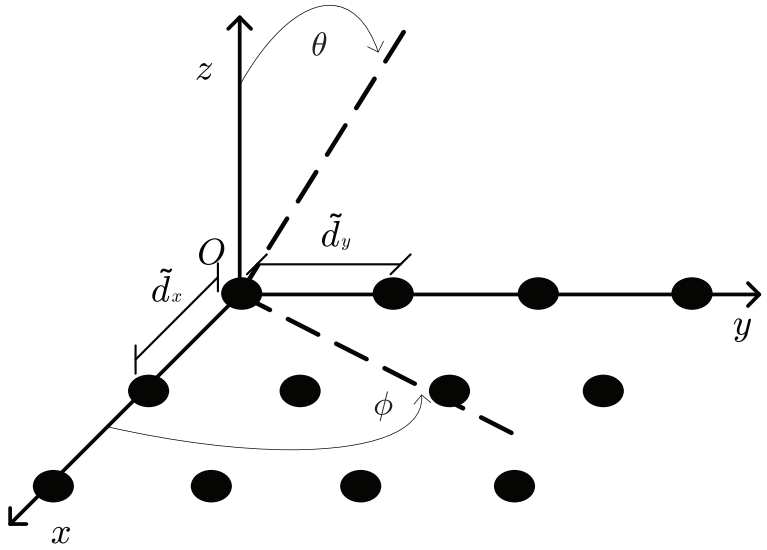

Figure 2.5: Example of array antenna with elements deployed on a rectangular lattice.

$$\boldsymbol{d_n} = l\tilde{d_x}\hat{\boldsymbol{i}}_{\boldsymbol{x}} + m\tilde{d_y}\hat{\boldsymbol{i}}_{\boldsymbol{y}} \tag{2.18}$$

in which $\tilde{d_x}$ represents the fixed distance between two consecutive elements along the Ox axis, $\tilde{d_y}$ represents the fixed distance between two consecutive elements along the Oy axis, $l = 1, \ldots, L$ and $m = 1, \ldots, M$, with L the total number of lines of linear arrays parallel to the y axis and M the total number of linear arrays parallel to the x axis, respectively (see Fig. 2.6).

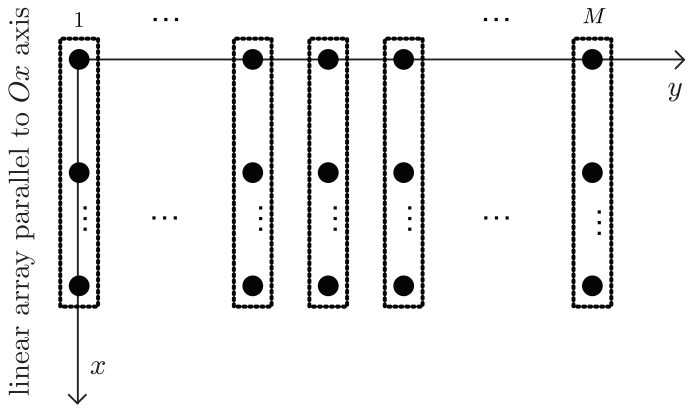

Figure 2.6: Planar array as a series of M linear arrays parallel to the x axis.

Considering the particular case of a rectangular aperture with identical antenna elements deployed on a rectangular lattice, the pattern expression becomes

$$E(\theta,\phi) = \tilde{f}(\theta,\phi)\sum_{l=0}^{L-1}\sum_{m=0}^{M-1} I_{lm}\exp\left\{\mathrm{j}k\left[l\tilde{d_x}\sin(\theta)\cos(\phi) + m\tilde{d_y}\sin(\theta)\sin(\phi)\right]\right\} \tag{2.19}$$

with I_{lm} the excitation of the element with coordinates $(l\tilde{d_x}, m\tilde{d_y})$.

Rectangular lattice, uniform array: directivity

In order to compute the directivity of a uniform planar array the general formula (2.7) has to be taken into account if no simplifying hypotheses are made. If, instead, a relatively large planar array is considered, the beamwidth and directivity are related to the following approximate equation [16]

$$\mathcal{D}_M \approx 32,400\frac{\cos(\theta_0)}{\theta_{x3}\theta_{y3}} \tag{2.20}$$

where θ_{x3} and θ_{y3} are the 3-dB beamwidths of the pencil or elliptical beam at broadside and θ_0 is the direction in which the beam points. In this formula, the beamwidths are in degrees. Elliott [17] (p. 206) shows that for a relatively large rectangular array, with a separable distribution and not scanned too close to endfire, the directivity is approximately given by the following expression

$$\mathcal{D}_M = \pi\mathcal{D}_x\mathcal{D}_y\cos(\theta_0) \tag{2.21}$$

that further reduces to

$$\mathcal{D}_M = \pi LM\mathcal{D}^2_{M_{\text{elem}}} \cos(\theta_0) \tag{2.22}$$

by using Eq. (2.14) and assuming all elements being equally fed.

In this particular case, the first (highest) SLL associated to the pattern, if a circular aperture is considered, is equal to 17.6 dB under the maximum value [51] (p. 21).

Rectangular lattice, uniform array: grating lobes

For this configuration GL may occur along the two main directions ($\phi = 0°$ and $\phi = 90°$) i.e. where the projections of the element positions create the regular linear array [78], an effect that can be easily understood based on the configuration shown in Fig. 2.6. Upon invoking Eq. (2.15), the respective conditions along the Ox and Oy axes become

$$\frac{\tilde{d_x}}{\lambda} = \frac{p_1}{\sin(\theta_0)\cos(\phi_0) - \sin(\theta_{\text{GL}\phi=0°})} \quad p_1 = \pm 1, \pm 2, ... \tag{2.23}$$

$$\frac{\tilde{d_y}}{\lambda} = \frac{p_2}{\sin(\theta_0)\sin(\phi_0) - \sin(\theta_{\text{GL}\phi=90°})} \quad p_2 = \pm 1, \pm 2, ... \tag{2.24}$$

where (θ_0, ϕ_0) is the direction where the beam is pointing.

Triangular lattice, uniform array

Triangular grid uniform arrays are antenna configurations in which the elements are deployed on a regular triangular grid. In such configurations, the distance between a generic element and its six immediate neighbours is constant and equal to d_t, as shown in Fig. 2.7. An expedient artifice for facilitating the evaluation of the radiative characteristics of uniform triangular arrays is to resort to a superposition of two regular rectangular lattices, as suggested by the use of the empty and full circles in Fig. 2.7. It is important to note that this lattice entails a higher element density than that obtainable with a square lattice of identical inter-element distance. Consequently, triangular lattices are preferred in the case when the available area estate is limited. Hence the formulas relating the radiated field and the element positions can be readily obtained as (see Appendix B) [78]:

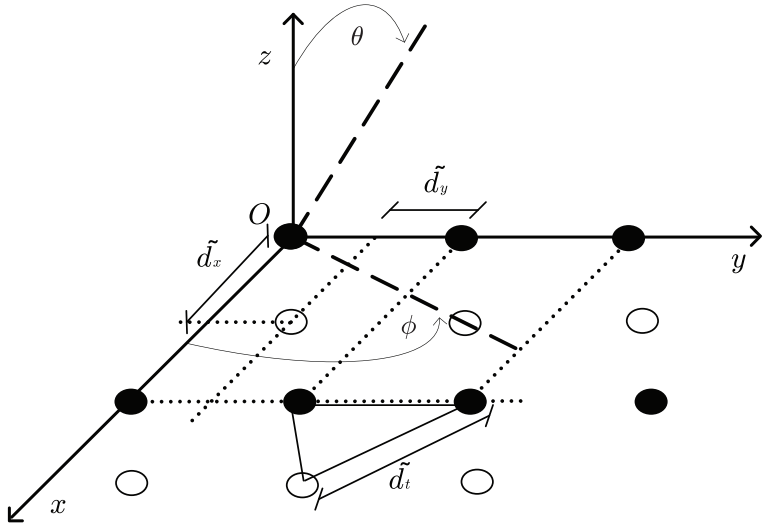

Figure 2.7: Example of array antenna with element deployed on a triangular lattice

$$E(\theta,\phi) = \tilde{f}(\theta,\phi)\sum_{l_1=0}^{L_1}\sum_{m_1=0}^{M_1} I_{l_1 m_1}\exp\Big\{\mathrm{jk}\Big[\mathrm{l}_1\tilde{\mathrm{d}}_{\mathrm{x}}\sin(\theta)\cos(\phi) + m_1\tilde{d}_y\sin(\theta)\sin(\phi)\Big]\Big\}\sum_{l_2=0}^{L_2}\sum_{m_2=0}^{M_2} I_{l_2 m_2}\exp\Big\{\mathrm{jk}\Big[(\mathrm{l}_2\tilde{\mathrm{d}}_{\mathrm{x}} + \delta_x)\sin(\theta)\cos(\phi) + (m_2\tilde{d}_y + \delta_y)\sin(\theta)\sin(\phi)\Big]\Big\} \tag{2.25}$$

where $d_x = \sqrt{3}d_t$, $d_y = d_t$ and one of the two rectangular, identical lattices is shifted, when compared to the other one, over $\delta_x = \sqrt{3}/2d_t$ along the Ox axis and over $\delta_y = d_t/2$ along the Oy axis.

For this configuration GL occur along several directions, namely, $\phi = 0^\circ + s_1 60^\circ$ with $s_1 = 1, 2, ...$ and $\phi = 30^\circ + s_2 60^\circ$ with $s_2 = 1, 2, ...$ The angles θ_{GL} can be derived from

$$\frac{\tilde{d}_t\sin(60^\circ)}{\lambda} = \frac{p_1}{\sin(\theta_0)\cos(\phi_0) - \sin(\theta_{\mathrm{GL}\ \phi=0^\circ})} \quad p_1 = \pm 1, \pm 2, ... \tag{2.26}$$

for $\phi = 0^\circ + s_1 60^\circ$, and

$$\frac{\tilde{d}_t\cos(60^\circ)}{\lambda} = \frac{p_2}{\sin(\theta_0)\sin(\phi_0) - \sin(\theta_{\mathrm{GL}\phi=30^\circ})} \quad p_2 = \pm 1, \pm 2, ... \tag{2.27}$$

for $\phi = 30° + s_2 60°$ where (θ_0, ϕ_0) is the direction where the beam is pointing (see [51], p. 184).

The triangular lattice is often used, especially in antenna designs where the space available for the antenna aperture is limited, because, by using this instead of, for example, a rectangular lattice with the same inter-element distance, it is possible to accommodate more antenna radiators in the same space.

Hexagonal lattice, uniform array

Another interesting uniform lattice is the hexagonal one (see Fig. 2.8). It should be noted that this lattice is less frequently used as the polygonal cell resulting from this lattice are equilateral triangles.

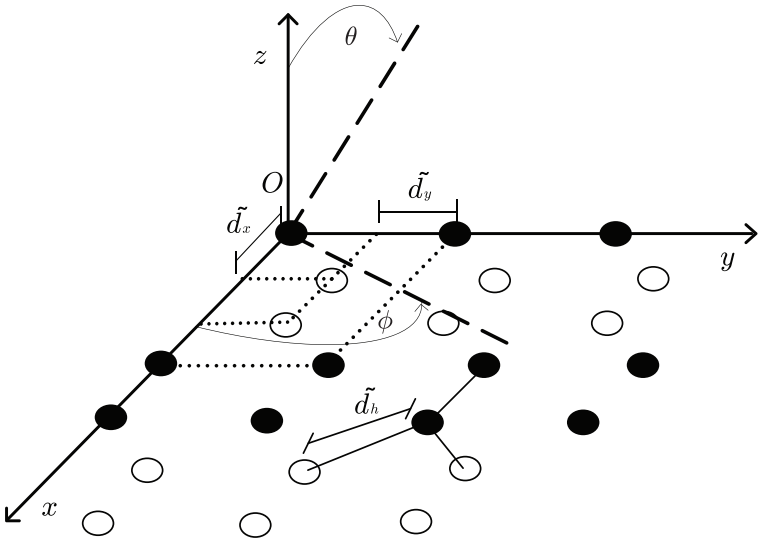

Figure 2.8: Example of array antenna with element deployed on a hexagonal lattice.

In this case each element is surrounded by three equi-distant ones at $d = \tilde{d}_h$. If we now consider the fix spacing along the axis and $\tilde{d}_x = \tilde{d}_h/2$ and $\tilde{d}_y = \sqrt{3}/2\tilde{d}_h$ it is possible to write the field in a compact manner as (see [66] and Appendix B)

$$E(\theta,\phi) = \tilde{f}(\theta,\phi) \sum_{l=0}^{L-1} \sum_{m=0}^{M-1} I_{lm} \exp\left\{ \mathrm{j}k \left[(\mathrm{mod}(m,2) + 4l)\, \tilde{d}_x \sin(\theta)\cos(\phi) + \right.\right.$$
$$\left.\left. + \; m\tilde{d}_y \sin(\theta)\sin(\phi) \right] \right\} \tag{2.28}$$

where the operator $\mathrm{mod}(q, w)$ gives the rest of the entire division q/w and the element identified by the indexes (l, m) is the $(l+1)^{\text{th}}$ radiator along the $(m+1)^{\text{th}}$ column parallel to the Ox axis.

As just stated, each element is surrounded by three equi-distant neighbours spaced at a distance $\tilde{d}_h$. It is interesting to note that for the same characteristic spacing d the cell area is 50% larger in the case of the hexagonal lattice when compared to the triangular one (see Appendix B, p. 130). This element density reduction has a twofold beneficial effect: on the one hand, it simplifies the feeding network; on the other hand, it allows the use of larger elements, potentially increasing the individual antenna gain [66].

The grating lobe positions and the positions of high lobes (HL), whose level is not the same as the grating ones but still may affect heavily the pattern performance, can be computed as (see Appendix B)

$$\theta_{\mathrm{GL}} = \sin^{-1}\left(\frac{\lambda m}{d/2}\right) \quad \text{for} \quad \phi = k60^\circ,\ k = 1, 2, ...,\ \text{and}\, m = 1, 2, ... \tag{2.29}$$

$$\theta_{\mathrm{HL}} = \sin^{-1}\left(\frac{\lambda n}{3d/2}\right) \quad \text{for} \quad \phi = k60^\circ,\ k = 1, 2, ...,\ \text{and}\, n \neq 3, 6, 9... \tag{2.30}$$

$$\theta_{\mathrm{GL}} = \sin^{-1}\left(\frac{\lambda}{d\sqrt{(}3)/2}\right) \quad \text{for} \quad \phi = 30^\circ + k60^\circ,\ k = 1, 2, ... \tag{2.31}$$

2.4 Non uniform Direct Radiating Array

When the positions of the elements are not a multiple of a fixed quantity or easily expressed according to a known law, it is not possible to use the simplified formulations presented in the previous sections. Regarding the radiated field, the general formula presented in Eq. (2.9) for the linear case, and Eq. (2.16) for the planar one, has to be used. For a general expression of the directivity, [45] is still one of the few published results.

Regarding the grating lobes level values (or better high SLL values as in non-periodic array, as already discussed, GL are not appearing), many formulations have been presented in the past years for particular classes of non-regular arrays. For example, formulas relating the GL positions with the elements distances can be found in case the elements are spaced according to specific laws [30] or their placement is completely random [67].

2.5 Concluding considerations

After this overview on uniform and non-uniform arrays it is possible to draw some conclusions:

- In order not to have GL appearing in the angles of interest a maximum spacing between the elements in a regular lattice configuration has to be imposed. This leads to a fixed, high number of elements to be used for covering the available antenna aperture. In case of non-uniform arrays the inter-element distance can be increased and, in this way, the number of radiators reduced.
- If the excitations of the different antennas are to be the same, then, in case of regular lattice array, the SLL is -13 dB for a linear array and -17 dB for a circular shaped aperture array. If a lower SLL is required the only opportunity is resorting to a proper non-uniform spacing of the elements.

Chapter 3

Non-uniform array synthesis techniques

In this chapter different synthesis techniques developed by the author for the design of non-uniform arrays will be presented. From evolutionary methods to analytic design procedures for linear and planar arrays, a selection of possibilities will be presented and compared.

In view of enhancing the readability of this account, this chapter will be confined to discussing a number of significant examples that have been dealt with by the author during this PhD research. The pertaining mathematical details are collected in Appendix C.

3.1 Non-uniform arrays

Various techniques for the synthesis of non-uniform arrays are available in the literature; some of them try to solve a particular class of non-uniform array problems in an analytical way [30, 85]; others resort to perturbative methods, describing the position of the elements as the one of an initial configuration plus a small increment, moving every iteration closer to the solution optimized according to certain requirements and cost functions. Other methods, called probabilistic techniques, like for example the Particle Swarm Optimization (PSO), the Ant Colony Optimization (ACO) and the Genetic Algorithms (GA), make use of laws mimicking the natural world to find the globally optimal solution. A particularly beneficial feature of this last category of techniques is that they don't get trapped in local minima: such a phenomenon can happen depending on the behaviour of the cost

function, in other non-probabilistic algorithms.

Hereafter, an illustrative selection of the categories mentioned before, will be presented. It has to be noted that the examples shown in the following sections have been obtained imposing requirements that can deviate from the ones reported in Appendix A. This is due to the fact that these synthesis methods have been developed over a large time span and not always for the same specific application.

3.2 Genetic Algorithm synthesis technique

The first synthesis technique presented is an evolutionary algorithm called Genetic Algorithm (GA). It is a versatile technique that has been lately applied to the optimization of problems in different research areas. More details on the general method are reported in Paragraph C.1.

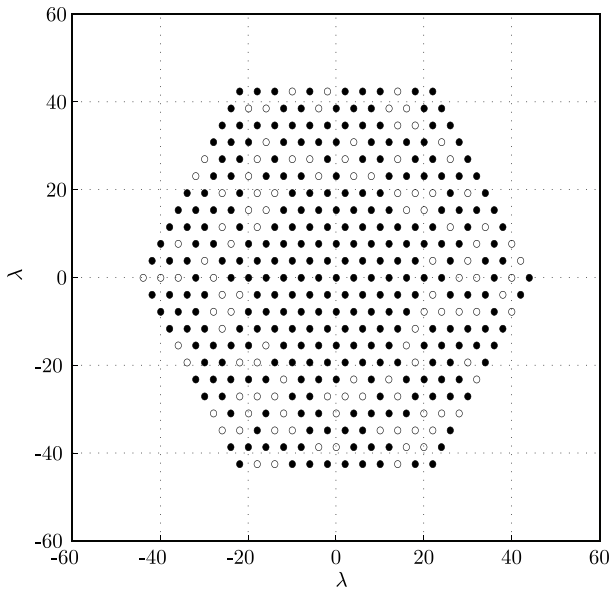

Figure 3.1: Thinned, optimized planar array designed by using the GA. The filled and empty circles represent the on and off elements, respectively.

The most important step in this algorithm is the definition of a cost function, i.e. of a law that gives the possibility to asses the suitability of a particular configuration. From a genetic point of view, this value measures the capacity of a certain individual of the generation to survive and procreate. From an antenna point of view it expresses how well a particular

configuration satisfies the imposed requirements.

In most of the papers published on the application of GA to antenna optimization problems [18] [25] the main objective is the pattern shaping according to a given mask. The technique discussed in this work approaches a multi-objective optimization task [79, 80]. Besides reducing as much as possible the number of elements used in the array configuration, the array shall guarantee a fixed gain value at the end of coverage (EOC) of each beam, and a maximum interfering isolation (C/I) in adjacent beams reusing the same frequency and polarization (see Appendix A for the definitions of EOC and C/I).

This technique developed by the author has been applied to selecting the element to be switched off in a large array with elements deployed on a regular triangular lattice (see Fig. 3.1 for the complete aperture). In Fig. 3.2 the radiation pattern of the proposed hexagonal array is depicted; the SLL values are in good agreement with the requirements of SLL $= -20$ dB with respect to the main lobe. A significant part of the elements of the initially

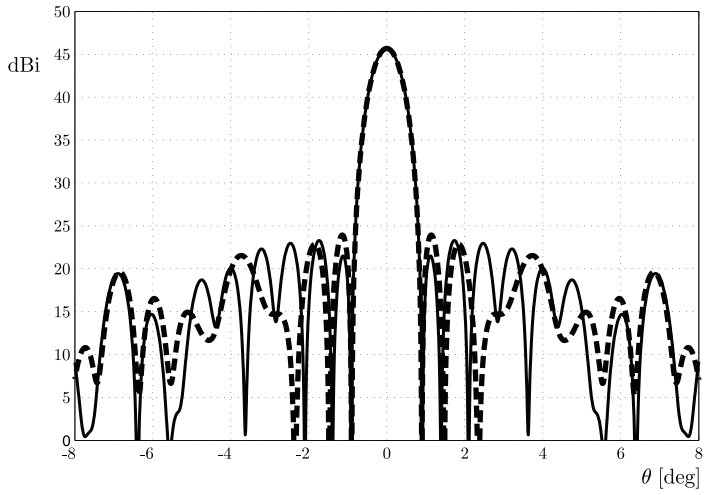

Figure 3.2: Pattern of the hexagonal array antenna shown in Fig. 3.1 for two ϕ cuts. $\phi = 0°$ – dotted line; $\phi = 90°$ – continuous thin line.

fully populated array can be switched off (the empty circles in Fig. 3.1, about 30% of the intial 397 elements), while maintaining the array beamwidth and improving the radiation characteristics in the sidelobe region in order to comply with stringent constraints. Moreover, the final configuration permits having all High Power Amplifier (HPA) operating at the same point, optimized for the efficiency.

The application of the Genetic Algorithms to selecting the elements to be switched off in a uniform array is particularly straightforward, since these techniques, in their standard implementation, deal with binary data and the one presented before is inherently binary [20] [26]. Unfortunately, the possibilities to shape the pattern, while guaranteeing a minimum gain level in determined areas, are quite limited. Using this technique for finding the position of the elements in a non-uniformly spaced array is not as direct and simple as finding which of the elements have to be switched off to properly shape the pattern. Some of the papers published so far on this subject, [10, 64] codify in the chromosome (possible solution of the problem) the position of the elements. In this case, since the positions are real numbers, depending on how many bits are used, the results become a more or less accurate approximation of the optimal solution. It is evident that using longer chromosomes implies a larger solution space and an increased computational burden, rendering this method not efficient especially if compared with deterministic techniques.

3.3 Null matching synthesis technique

The aim of the synthesis technique presented in this section is to design a non-uniform array in such a way that its nulls occur exactly at some given angles. With this technique, as already seen with the zero crossing sampling [36], it is possible to reproduce, without taking into account mutual coupling effects, the radiative properties not only close to the null positions but everywhere in the pattern. The rigorous approach would imply the solution of a set of real, transcendental equations which can be practically solved when the number of array elements is considerably limited. With the algorithm proposed here (see [73] and Paragraph C.2), based on a similar zero-matching strategy, the design of non-uniform arrays is achievable for an arbitrary number of elements. Moreover, the technique has been extended to the case of planar array design, as demonstrated in [56].

Most of the techniques presented so far for the design of arrays with deep nulls occurring at certain angles in the radiation pattern [32, 64] make use of iterative perturbations of the element position (see next section). On the contrary, the technique presented here [56, 73] is able to achieve good results just by applying a simple minimization procedure.

The method has been applied to the design of non-uniform arrays for satellite communications by using the formulation in Paragraph C.2. In the hereby considered case, a set of nulls are imposed over Europe's coverage; the aim is to obtain a deep null in the radiation pattern exactly at the angular

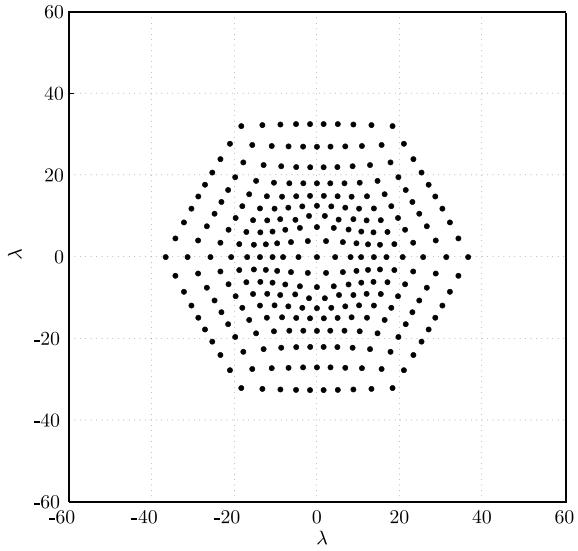

Figure 3.3: Planar non-uniform array consisting of 271 elements, designed by using the optimization technique of Paragraph 3.3.

position where the beam using the same frequency is located. Starting from a regular triangular lattice array, the positions have been modified as in Fig. 3.3, according to the formulation described at p. 141, the array factor corresponding to the synthesized array being shown in Fig. 3.4. In the same figure it is possible to notice how, by using this technique, it becomes possible to enforce nulls in the pattern, the desired position of them being represented by the triangles and dots for $\phi = 90°$ and $\phi = 0°$, respectively.

The null-matching synthesis technique is quite useful in the design of linear non-uniformly spaced arrays. In the simple case of extending the technique to a planar array by specifying the positions of some of the interfering spot beams and enforcing a null in that area, it provides good results in terms of SLL only in the neighborhood of the considered angles. The main disadvantage of this technique is that, in order to obtain a good agreement between the pattern of the achieved non-uniform array and the one of the reference array, one can only specify requirements in terms of nulls in the radiation pattern. If locations and values other than nulls are used, the pattern behaviour is not able to match the reference one. This is also the main difference when compared with the previously discussed GA technique, where depending on the cost function definition, different requirements could be included for steering the optimization. The null-match synthesis method is anyway faster then the GA one and effective for some particular applications where the attention is focused on the nulls in the radiation pattern.

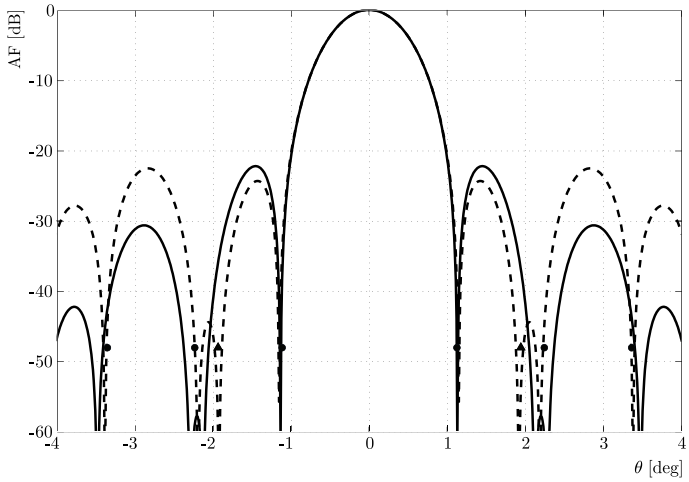

Figure 3.4: Array Factor along $\phi = 0°$ – continuous line and $\phi = 90°$ – dotted line, obtained with the min-max technique described in this section. The triangles represent the null position for $\phi = 90°$, the circle the ones for $\phi = 0°$.

3.4 Perturbative synthesis technique

Another interesting category of synthesis techniques is the pertubative one. This category encompasses a family of methods that reach an optimum configuration by starting from a given one and altering at each iteration the position of the elements by small increments.

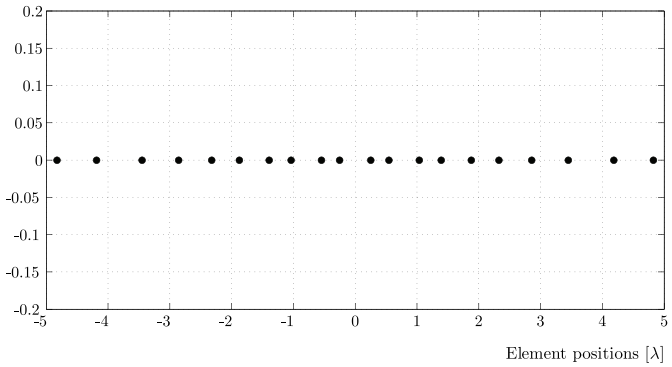

Figure 3.5: Linear array antenna designed with the perturbative synthesis technique.

In the past years this method was, in conjunction with the null-matching

technique, the author's desing method of choice for linear arrays. Starting from the positions found by the previously described algorithm it was possible to find, in a fast and accurate way, the best solution close to the one achieved with the null-matching technique.

A detailed mathematical description of the employed strategy is given in Paragraph C.3. Several examples of perturbative approaches can be found in the literature. Some of them, like [23, 27], aim at the reduction of the SLL in a discrete number of angular directions according to a given reduction law, by starting from an initial uniform array and introducing a perturbation at each step. Other techniques change the position of the radiators, by means of small increments, in order to impose deep nulls in the pattern [32],[64]. This is also the case of the synthesized example discussed in this section.

The perturbative technique is applied to the design of a linear non-uniform array with nulls matching the ones of a Tchebyschev distribution [14]. In this example the design of an array with 20 elements, whose zeros are to match the ones of a Tchebyschev distribution with SLL $= -21\,\mathrm{dB}$, is addressed. The position of the radiators in the non-uniform array have been depicted in Fig. 3.5; these positions have been obtained starting from a uniform array configuration. All antenna elements are fed with an equal amplitude. As it can be noticed from Fig. 3.6, the nulls are exactly matching the reference ones (black dots in the figure), while all sidelobes have a SLL $\leqslant -21\,\mathrm{dB}$.

It is stressed that the perturbative variant presented in this section can

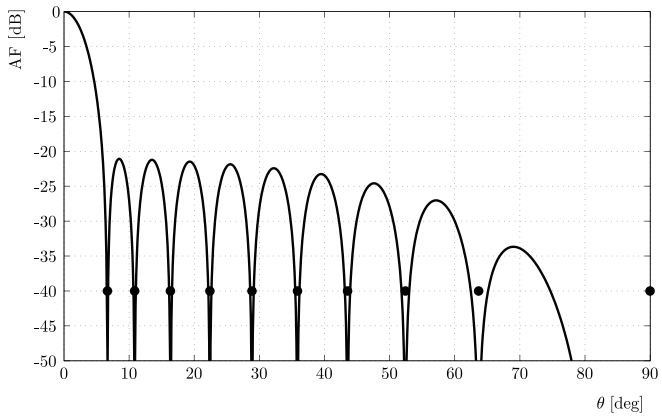

Figure 3.6: The Array Factor of the non-uniform array in Fig. 3.5 The continuous line represents the Array Factor and the black dots the position of the Tchebyschev nulls.

be applied by starting from a configuration already optimized with other techniques, thus close to the optimal one, or by starting from a uniform configuration. In that case, larger computation times or, alternatively, limited accuracy in the replicated pattern should be expected. In order to apply rigorously this technique, it has to be ensured that the positions found at each iteration are not too far from the ones achieved at the previous step. It has to be noticed that the presented technique can be applied also to the design of non-uniform arrays that satisfy a required radiation level at pre-determined angles and not necessary for matching the radiation pattern nulls. The achieved accuracy in the array synthesis strongly depends on the number of iterations.

3.5 Auxiliary array function synthesis technique

This section focuses on a design technique aimed at synthesizing a non-uniform linear array having a desired array factor. The method is completely analytic and can take into account requirements in terms of minimum spacing. The technique, discussed in detail in Paragraph C.4, makes use of the continuous counterpart of the array factor, here denoted as the Auxiliary Array Function (AAF). Thanks to a proper piece-wise linearization of the continuous normalized positioning, amplitude and phase functions, it is possible to equate the transform of the AAF to the one of the objective function in the Fourier domain. This leads to a rigorous and straightforward procedure to compute the array element positions without resorting to any optimization procedure. More details on this method are provided in Appendix C.

It should be noted that the use of a normalized source position function of the type employed by this method was already proposed in [30]. Nevertheless, the hereby advocated synthesis technique brings in a clear conceptual progress and functional effectiveness by resorting to an analytical relationship of the Fourier transform of the AAF and the objective function.

The capabilities of the Array Factor Function (AAF) synthesis technique are now exemplified by discussing the design of a linear non-uniformly spaced array for uniform radio coverage of the Earth surface from geosynchronous satellites. The resulting antenna configuration, consisting of 10 radiators, has been then used for planar array implementation, as shown in Fig. 3.7. Two cuts of the AF pattern have been plotted in Fig. 3.8. The continuous line represents the pattern for $\phi = 0^\circ$ or $\phi = 90^\circ$, i.e. along the main axes Ox and Oy, where the projections of the array position correspond to the designed linear array. In these particular directions the pattern

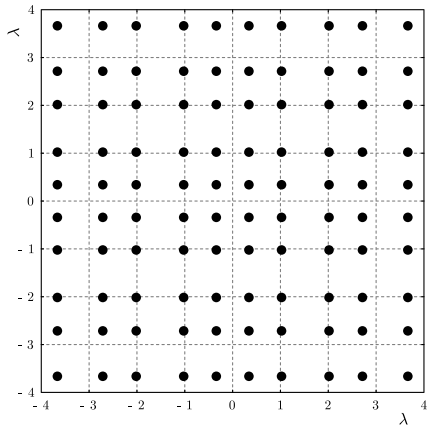

Figure 3.7: Position of the radiators in a two-dimensional array configuration for Earth radio coverage from a GEO satellite.

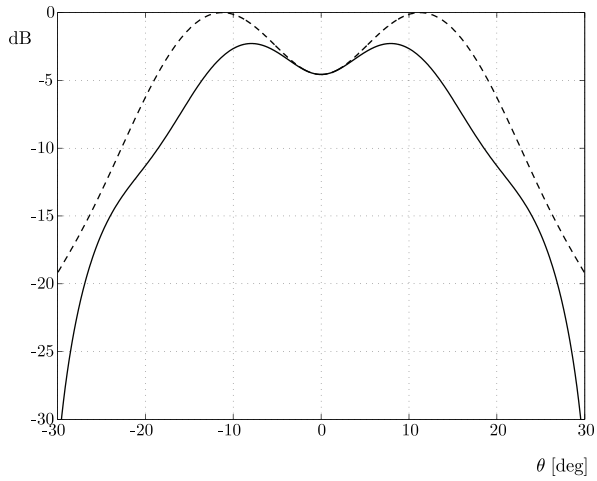

Figure 3.8: Array Factor of the designed rectangular array configuration in Fig. 3.7. Continuous line – pattern for $\phi = 0°$, dotted line – pattern for $\phi = 45°$.

properly matches the imposed mask, while in all the other intermediate cuts, like for example $\phi = 45°$, plotted in the figure in dotted line, the match is only partial.

This technique has been developed for linear non-uniform arrays and has been extended to planar arrays by using the pattern multiplication method only. Unfortunately, the pattern multiplication method is not the best way to design a planar array, A proper extension of this technique to

the planar case would make it a really powerful tool to be used every time a desired pattern has to be obtained.

3.6 Concluding considerations

The techniques catalogued in this chapter are quite useful for some applications. However, none of them is satisfactory for the antenna design at the core of this work for any of the following reasons:

- The GA based synthesis techniques, even if they have been extended to the case of continuous variables [10], are more suited for problems like switching off some of the elements in a uniform array, where the parameter to be optimized is easily convertible into a binary number. Moreover the time needed for an optimization and the computation burden associated to each of them are quite demanding.
- The null-matching synthesis technique is particularly efficient when the aim of the design is to obtain nulls in the pattern for specified angles but fails in cases where requirements like the minimum directivity in specified angular region and a maximum SLL have to be guaranteed.
- The pertubative technique, as evident from the formulation in Appendix C, needs to start the optimization from a point that is not too far from the optimal solution in order to give fast and good results. In this case, in order to apply the technique rigorously, the user has also to ensure that, at each step, small increments are added to the positions.
- The AAF method is quite general, dealing both with an excitation taper and element positions. Unfortunately it has been extended to planar arrays by means of a simple, pattern multiplication, algorithm. This approach results in a square array whose pattern along the principal planes is satisfying the desired specifications, but not in other ϕ planes. This technique is powerful in order to replicate a desired pattern but not when the requirements are expressed in terms of several SLL as for example with reference masks, as the method aims to replicate the Fourier transform of the objective function.

For these reasons a new synthesis algorithm has been developed and it will be presented in the following chapter.

Chapter 4

A deterministic synthesis technique for planar non-uniform arrays

In this chapter an array antenna synthesis technique inspired by natural spiral shapes is presented. Firstly, a spiral element positioning law is introduced and its properties are discussed. The case of a spiral uniform placement, already partially presented in [4], is investigated and used as a starting point for an original synthesis method that is elaborated upon in this chapter. Thanks to a non-uniform density taper of the element positions, it is hereafter shown how it is possible to shape the array antenna pattern without resorting to any taper on the element excitations. In this way it is possible to achieve the same pattern performances in terms of SLL, obtainable by means of applying an amplitude taper to the element illumination.

4.1 Spirals

Spirals are among the most common regular shapes in nature: from the snail shell, to the sunflower seed placement, to the Milky way arms. Different kinds of spirals are known in the literature.

A particular type of spiral, frequently encountered in nature, turns out to be extremely beneficial for array antenna synthesis. Concretely, it was observed that, by relating the radial and the angular spacing in the spiral to the Golden Ratio , an irrational number known also as the Fibonacci number, the generated subdivision of the space has a remarkable uniformity. This

Figure 4.1: Example of spiral placement of the seeds in a sunflower.

feature can straightforwardly be recognized in nature where, for example, the leaves around a stem or the seeds in a sunflower (see Fig. 4.1), use this positioning to share in an optimal way space and light [1]. Due to the visual similarity between the array elements positions determined by the laws to be presented hereafter, and the sunflower seed positions, the original synthesis method discussed in this work and the antennas designed in this manner will be termed as *sunflower law* and *sunflower antennas*, respectively. Details on the specific properties of this spirals are discussed at length in Appendix D. Hereafter, it will be shown how the features of this kind of spiral can be effectively used for synthesizing planar arrays that allow for large inter-element spacing while preventing the onset of Grating Lobes (GL) (see Paragraph 2.4). By then using an original artifice, the good GL-free characteristic of the pattern will be supplemented by a proper spatial tapering. The resulting antennas will be shown to combine extremely low sidelobe levels, GL-free scanning capabilities and large inter-element spacing allowing for radiators characterized by high gain to be accommodated. All these positive characteristics recommend the presented type of antennas, among others, for space applications.

4.2 Uniform spiral array

Consider the elements in a planar array to be placed along the spiral according to the following equations (see Fig. 4.2 for the significance of the employed geometric parameters)

$$\rho_n = s\sqrt{\frac{n}{\pi}}, \quad \text{for } n = 1, \ldots, N \tag{4.1}$$

$$\phi'_n = 2\pi n \beta_1, \quad \text{for } n = 1, \ldots, N \tag{4.2}$$

where ρ_n is the distance from the spiral center to the n^{th} element, $n = 1, \ldots, N$, with N denoting the total number of elements, the parameter s relates to the distance between neighbour elements [4] and the parameter β_1 controls the angular displacement ϕ' between two consecutive elements.

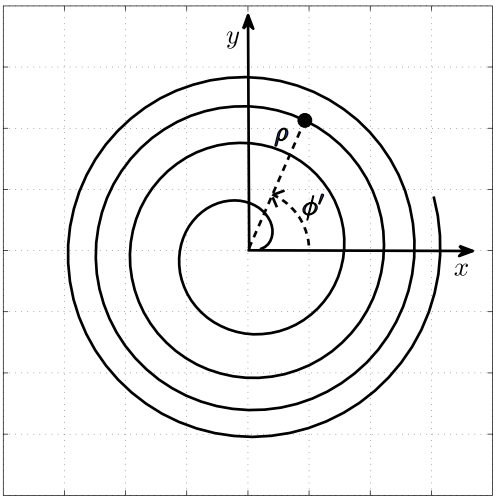

Figure 4.2: The Fermat spiral. The location of the current point is specified in polar coordinates ρ, ϕ'.

Next we assume a non-uniform array deployed on a circular aperture of radius R_{ap} along the proposed spiral (usually referred to as a Fermat spiral, see Appendix D), with element locations given by Eqs. (4.1) and (4.2).

Let us now introduce a normalized element density function

$$\tilde{d}(\rho_n) = \frac{K_n}{\pi \left(R_n^2 - R_{n-1}^2\right)}, \quad \text{for } n = 1, \ldots, N \tag{4.3}$$

where R_{n-1} and R_n are the inner and outer radii of the annular ring enclosing the n^{th} element, respectively, and K_n represents the amount of current distribution $A(r, \psi)$ enclosed by that annular region, namely

$$K_n = \int_0^{2\pi} \int_{R_{n-1}}^{R_n} A(r, \psi)\, r \, \mathrm{d}r \, \mathrm{d}\psi, \quad \text{for } n = 1, \ldots, N. \tag{4.4}$$

Note that R_0 will be always taken equal to zero. By taking A as being a rotationally symmetric amplitude taper it is possible to write Eq. (4.4) as

$$K_n = 2\pi \int_{R_{n-1}}^{R_n} A(r)\, r \, \mathrm{d}r \quad \text{for } n = 1, \ldots, N. \tag{4.5}$$

Now, since it was assumed that each annular ring contains one radiator only, the normalized density function in Eq. (4.3) corresponds, in fact, to the current of a single element divided by the area of the relevant annular ring.

With the assumption that each element n is fed by the same amount of current the quantities K_n read

$$K_n = \frac{2\pi}{N} \int_0^{R_{ap}} A(r) r \mathrm{d}r = K \quad \text{for } n = 1, \ldots, N. \tag{4.6}$$

By taking the radii R_n as

$$R_n^2 = \frac{\rho_{n+1}^2 + \rho_n^2}{2} \quad \text{for } n = 1, \ldots, N \tag{4.7}$$

the substitution of Eqs. (4.1) and (4.6) in Eq. (4.3) yields a normalized element density function

$$\tilde{d}(\rho_n) = \frac{K}{\pi \left(\rho_{n+1}^2 - \rho_{n-1}^2 \right)} = \frac{K}{s^2} \quad \text{for } n = 1, \ldots, N, \tag{4.8}$$

that is, evidently, constant. It can now be concluded that an element placement strategy using the choice of radii in Eq. (4.3), this choice being the one adopted in [4], will result into a non-uniform array with a uniform distribution (in the sense of the density function in Eq. (4.3)).

In support of this statement, an array consisting of 250 isotropic radiators is synthesized in this manner, the resulting configuration being shown in Fig. 4.3. A visual inspection of the plot confirms its high degree of uniformity with remarkably similar inter-element spacing. For providing a quantitative

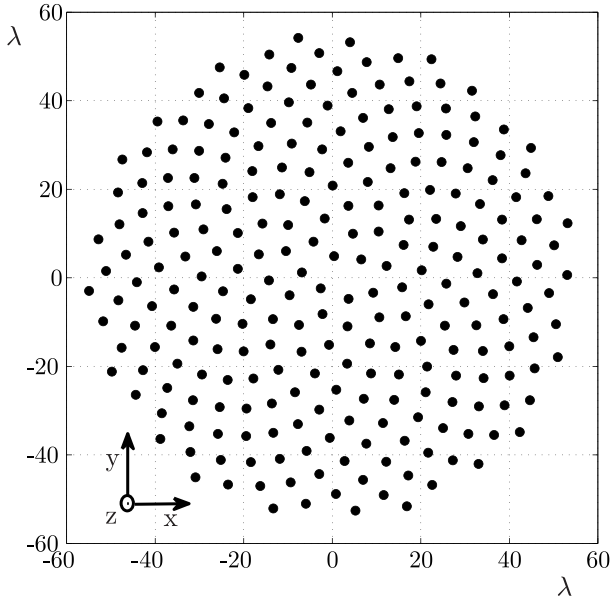

Figure 4.3: Distribution of the 250 elements in the non-uniform array antenna with almost identical inter-element spacings, as reported in [4].

proof of this property, a *normalized density taper* is computed by selecting $P = 25$ equi-pollent annular rings covering the complete aperture, counting the elements in each ring A_p and, finally, normalizing the numbers to the maximum value via $\tilde{A}_p = A_p/\max(A_p)$ (see Fig. 4.4). The result of this operation is shown in Fig. 4.5, demonstrating that the element density is, indeed, uniform. The experiment is rounded off by evaluating the array factor of the array in Fig. 4.3. In the vicinity of the main beam (see Fig. 4.6), the array pattern behaves similarly to a uniformly spaced, uniformly fed array, the maximum first SLL amounting to about -17dB [51]. However, outside the interval $[-5°, 5°]$, the array factor starts deviating from this behaviour, with the SLL rising and, then, remaining approximately constant at a value that depends on the number of radiators [10, 30].

This angular region can be estimated by taking into account the maximum inter-element distance. In fact, while in uniform lattice arrays a large inter-element distance causes the onset of GL, in non-uniform arrays, as the periodicity is broken, the energy of these GL is spread over a larger area, resulting in higher SLL's over a region that depends on the minimum and maximum inter-element spacing.

Concluding: a non-regular lattice array with uniform density taper is attractive when the interest focuses on only avoiding GL, as it was the

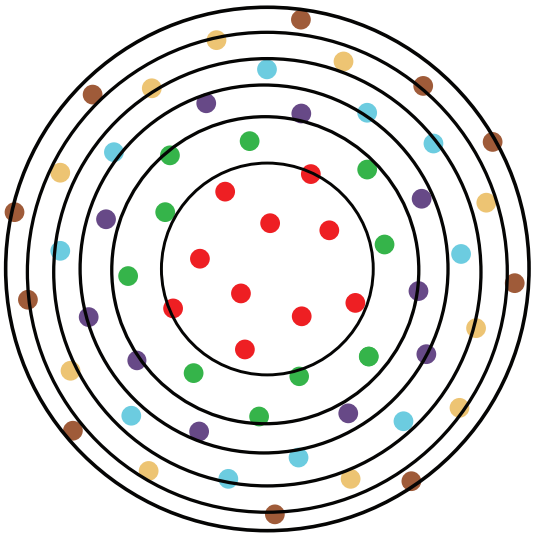

Figure 4.4: Example of the aperture subdivision in equipollent rings. The elements in different rings are in different colors.

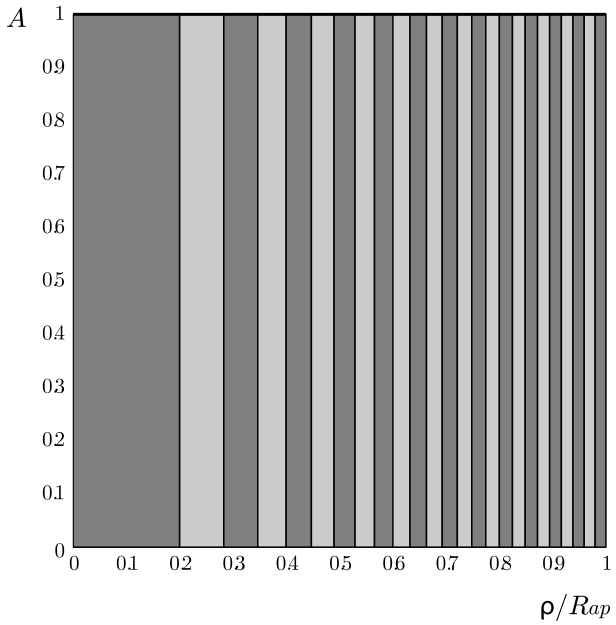

Figure 4.5: Amplitude and density taper for the non-uniform configuration in Fig. 4.3. Thick black line – reference constant amplitude taper; alternate grey rectangles – normalized density taper.

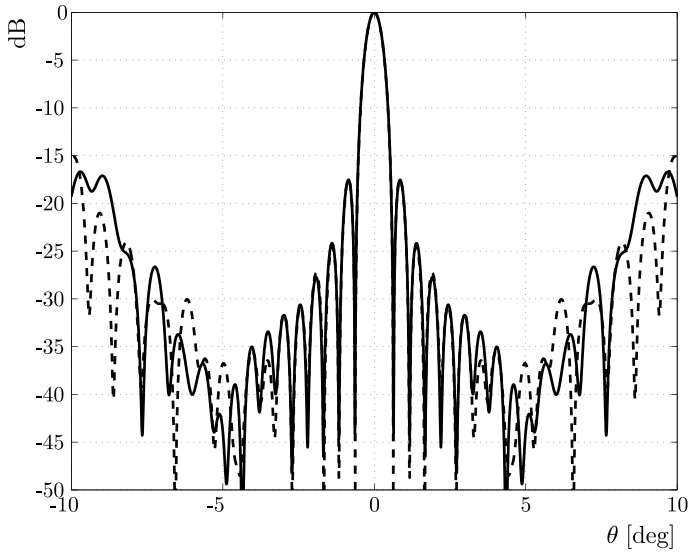

Figure 4.6: Array Factor of the non-uniform array in Fig. 4.3 for two ϕ cuts. $\phi = 0°$ – dotted line; $\phi = 90°$ – black line.

case in [4]. Having elements characterized by the same amplitude, placed in the array such that they all occupy the same area leads to a uniform density taper. This corresponds to a uniform amplitude taper and results in a maximum SLL that remains around -17 dB, irrespective of the number of elements in the array and their spacing.

It is now clear that the only possibility to control the SLL, as well, is by introducing a non-uniform density taper, hence associating a different area to the radiators in the array. In the next section it will be demonstrated how, by translating a Taylor amplitude tapering law [69] (see Appendix E) into a corresponding spatial density law, the SLL can be drastically reduced.

4.3 Spiral array with density tapering

The spiral non-uniform lattice with a uniform element density introduced in the previous paragraph is an excellent starting point to apply a space tapering strategy. The spreading of the elements in the spiral arms guarantees an optimal behaviour in terms of GL even when the inter-element spacing is larger than λ. In order to be able to control the SLL it is possible to vary the elements positions with respect to the array center, thus obtaining an effect similar to an amplitude taper. For reasons that will become clear, it is convenient to implement apertures accommodating elements of different sizes.

However, for facilitating the understanding of the proposed algorithm, it will be firstly assumed that all elements are identical and, subsequently, the strategy will be extended such that to cover the case of different elements.

4.3.1 Procedure for the case of apertures populated by identical elements

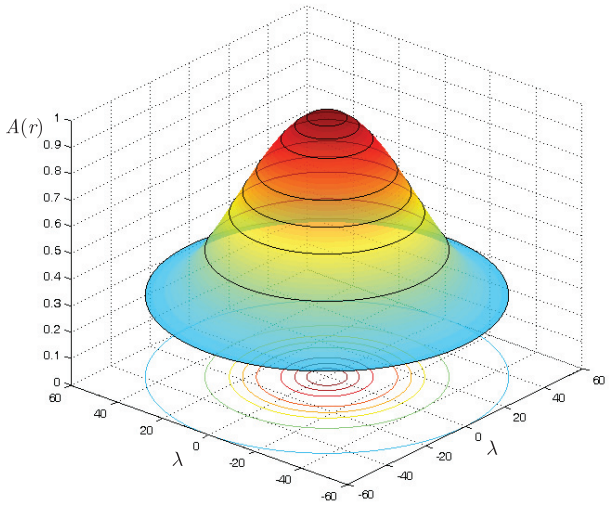

Figure 4.7: Subdivision of the total volume into N equal contribution.

The space taper technique presented here relies on choosing a reference amplitude distribution whose pattern satisfies the assigned requirements and, then, emulating it by varying the radiator distance from the center. Concretely, a Taylor amplitude taper law with a certain SLL and $\bar{n}$ [69] is selected as a reference (see Appendix E). The locations of the elements in the non-uniform array are determined by means of a simple, 2 step algorithm

- Firstly, as shown in Fig. 4.7, N circles of increasing radii ρ_n, n=1, 2 ...N are selected by sequentially applying the relations

$$2\pi \int_{R_{n-1}}^{\rho_n} A(r) r \mathrm{d}r = \frac{2\pi}{2N} \int_0^{R_{ap}} A(r) r \mathrm{d}r \tag{4.9}$$

$$2\pi \int_{R_{n-1}}^{R_n} A(r) r \mathrm{d}r = \frac{2\pi}{N} \int_0^{R_{ap}} A(r) r \mathrm{d}r \tag{4.10}$$

by starting from $R_0 = 0$. Here, $A(r)$ denotes the Taylor amplitude taper and R_{ap} is the radius of the complete (circular) aperture.

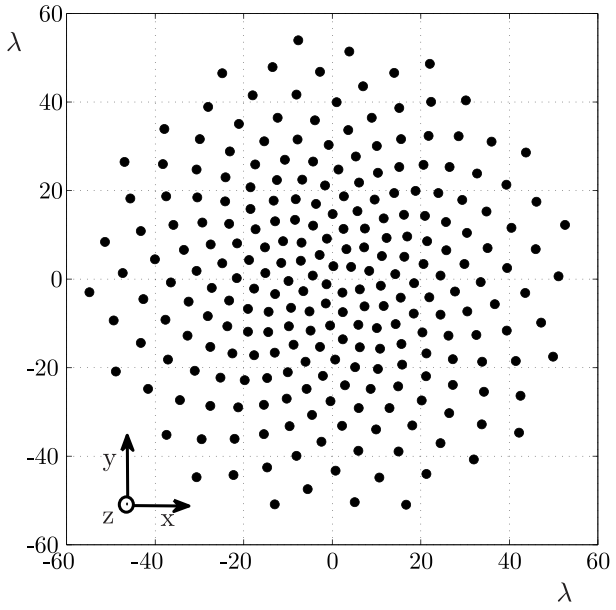

Figure 4.8: Distribution of the 250 elements in the tapered sunflower array antenna.

Note that Eq. (4.9) emulates the desired taper by equating the surface integral over the annular ring delimited by R_{n-1} and ρ_n to half of the N^{th} part of the total aperture excitation.

- Subsequently, the element positions are determined by choosing their pertaining angle ϕ_n according to Eq. (4.2).

The result of this placement strategy is illustrated in Fig. 4.8 where a 56 λ aperture is filled with 250 elements distributed in a manner such that we can obtain a pattern similar to the one achievable with a Taylor amplitude law characterized by SLL=32 dB and $\bar{\text{n}}$=4. A total number $N = 250$ is selected here as an example (see Appendix E).

For verifying the accuracy of the replication of the desired Taylor taper, the *normalized density taper* is calculated in a manner that is similar to the one discussed in Paragraph 4.2. The only difference concerns the normalization that becomes, in this case

$$\tilde{A}_p = \frac{A_p}{\max(A_p)} \frac{2\pi \int_0^{R_{ap}} A(r)/\max\left[A(r)\right] r \mathrm{d}r}{\pi \sum_{q=1}^{P} \left[A_q/\max(A_q)\right] \left(R_q^2 - R_{q-1}^2\right)} \quad \text{for } p = 1, \ldots, P. \tag{4.11}$$

where, as in the previouse case, A_p represents the number of elements enclosed in the equi-pollent annular ring delimited by R_{p-1} and R_p and the second term represents the ratio between the total normalized amplitude distribution and the total normalized density distribution. This last term ensures that the total current following from the reference, continuous Taylor distribution and its discrete counterpart are the same. The continuous and discrete tapers are compared in Fig. 4.9. The plot demonstrates the high accuracy of the obtained spatial density taper. The study of the configuration in Fig. 4.8 is supplemented by evaluating the array factor (see Fig. 4.10). The massive drop in the SLL, according to the chosen Taylor taper distribution characterized by a SLL $= -32$dB, demonstrates the performances of the non-uniform *sunflower* placement. As in the case of the example discussed in Paragraph 4.2, the SLL increases for angles $|\theta| \geq 5°$, creating a kind of plateaux [30].

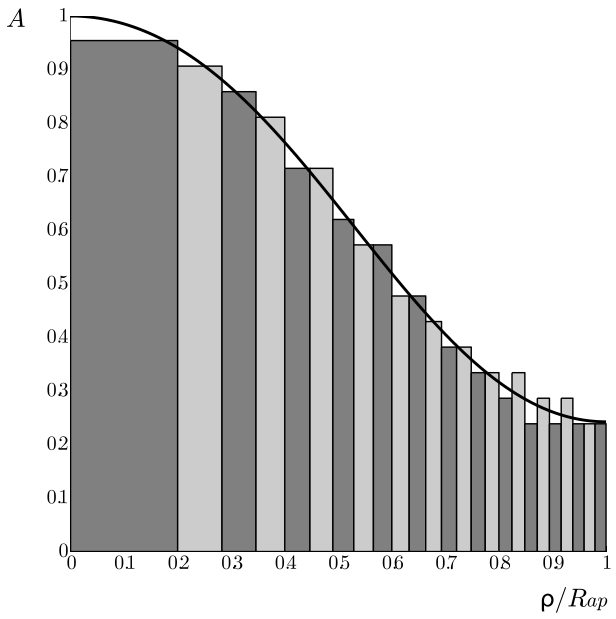

Figure 4.9: Amplitude and density taper for the non-uniform array configuration in Fig. 4.8. Thick black line – reference amplitude taper; alternate grey rectangles – normalized density taper.

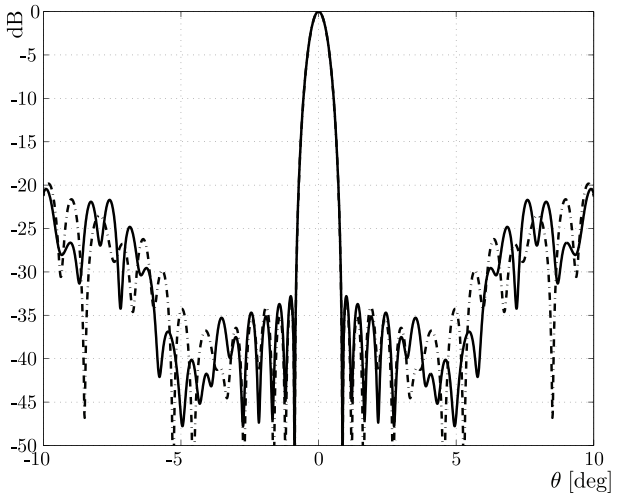

Figure 4.10: Array Factor of the non-uniform array in Fig. 4.8 for two ϕ cuts. $\phi = 0°$ – dotted line; $\phi = 90°$ – black line.

4.3.2 Procedure for the case of apertures populated by differently sized elements

An examination of the configuration in Fig. 4.8 reveals that the elements are quite agglomerated in the center, but the array becomes increasingly sparse when moving towards the periphery. When the element size is chosen in order to fit the dense central distribution it is evident that a lot of empty space will remain at the periphery, this impeding on the overall aperture efficiency. This effect can be counteracted by employing differently sized elements.

At this point it is important to stress that all implementations considered in this work employ *sub-arrays* as 'elementary radiators'. The elements in each sub-array, and the sub-arrays themselves, can be fed such that a given amplitude or a given power are ensured. The first choice has the advantage of resulting into an easier, more flexible design methodology since the designer can group together elements in sub-arrays in an arbitrary manner as long as they are fed with the same amplitude. Nevertheless, this is technologically cumbersome since the distribution networks inside sub-arrays (the most commonly used being Wilkinson dividers [61] (pp. 318–323) and the T-junction power dividers [61] (pp. 315–318)) distribute the *same power*. Assuming all elements in a sub-array to have the same input impedance, ensuring identical elementary amplitudes will require sub-arrays consisting of different numbers of elements to be fed by different input powers, an approach that is

not favorable for the space application aimed at in this work. It then follows that an equi-power sub-array feeding is to be preferred. However, this choice induces some design complications in the sense that the *sunflower* placement requires the total number of sub-arrays of each type to be known *a priori*. In practice, this restriction can be easily circumvented since, the placement being deterministic, possible variants can be evaluated in a fast manner this directly yielding an optimal allocation of sub-arrays per types.

Several options of element grouping were experimented with:

- Completely filled arrays – equi-amplitude. The complete available aperture is populated by elementary radiators deployed on a triangular lattice. The position of the sub-array phase centers are found using Eqs. (4.9) and (4.2). Then the elementary radiators are associated to their closest phase center and grouped. In this way the complete aperture is used, resulting in high directivity. Unfortunately, as each sub-array is different, this configuration is not easy from a technological point of view to be implemented and tested.

- Non-completely filled arrays – equi-amplitude. A procedure similar to the one adopted in the previous example is enforced. In this case just some of the elementary radiators, the closest to the phase centers, are selected and grouped. The farther ones are not employed in the array. For this configuration a reduced number of elementary radiators can be used, still satisfying the requirements in Appendix A. However the same main disadvantage of the previous array configuration has to be faced.

- Arrays composed of hexagonal sub-arrays – equi-amplitude. In this configuration just a few kinds of sub-arrays are employed. Their position can be found with Eqs. (4.9) and (4.2). It is easier to be implemented when compared with the previous two options proposed, but shares with them the difficulty of providing the same amplitude to differently sized sub-arrays. It is for this reason that the hexagonal sub-array configuration with equi-amplitude is considered as a good architecture in case of employing different amplifiers in the same array design.

- Arrays composed of hexagonal sub-arrays – equi-power. In this case the phase center positions of the sub-arrays are found according to the approach further explained below. The approach takes into account, from the beginning of the design, how many elementary radiators compose each sub-array. This results into an easier implementation from a

technological point of view, especially when the requirements impose to use the same amplifier for each sub-array.

The performance of each of these variants will be studied in Paragraph 4.4

4.3.3 Equi-power condition

The enumeration above made a clear distinction between the equi-amplitude and the equi-power placement variants. The identical amplitude condition was seen to allow for a direct use of the formulation presented in Paragraph 4.3.1. Nevertheless, when an equi-power condition needs being enforced, that formulation has to be amended slightly. To this end, let P_{tot} be the total power fed into the array. The equi-power requirement directly yields for N sub-arrays the power injected into each sub-array

$$P_{\text{sub}} = \frac{P_{\text{tot}}}{N}. \tag{4.12}$$

Recall now that the reference taper employed for determining the element location is an *amplitude* condition. By denoting as $\bar{N}_n$ the number of elements in the n^{th} sub-array and assuming an equal power distribution network for the sub-array, the corresponding amplitude for each element in the sub-array will read

$$A_{\text{sub}n} = \sqrt{\frac{P_{\text{sub}}}{\bar{N}_n}} = \sqrt{\frac{1}{N\bar{N}_n}P_{\text{tot}}}, \quad n = 1, ..., N. \tag{4.13}$$

yielding a total sub-array excitation

$$A_{\text{tot,sub}_n} = \bar{N}_n A_{\text{sub}n} = \sqrt{\frac{\bar{N}_n}{N}P_{\text{tot}}}, \quad n = 1, ..., N. \tag{4.14}$$

The quantity $A_{\text{tot,sub}_n}$ in (4.14) represents the area under the reference amplitude taper that corresponds to each of the N sub-arrays. Obviously, the summation of all sub-array contributions will correspond to the total area under the amplitude taper

$$A_{\text{tot}} = \sum_{n=1}^{N} A_{\text{tot,sub}_n} = \sqrt{\frac{P_{\text{tot}}}{N}} \sum_{n=1}^{N} \sqrt{\bar{N}_n}. \tag{4.15}$$

By substituting (4.15) in (4.14) it is now found that

$$A_{\text{tot,sub}_n} = A_{\text{tot}} \frac{\sqrt{\bar{N}_n}}{\sum_{n=1}^{N} \sqrt{\bar{N}_n}} \tag{4.16}$$

that demonstrates that the total sub-array excitation is proportional to the square root of the number of elementary radiators in it. Just like in the case examined in Paragraph 4.3.1, A_{tot} is now equated to the total current on the circular aperture

$$A_{\text{tot}} = 2\pi \int_0^{R_{ap}} A(r) r \mathrm{d}r. \tag{4.17}$$

This immediately allows for determining the phase center positions by means of the expressions

$$2\pi \int_{R_{n-1}}^{\rho_n} A(r) r \mathrm{d}r = \frac{2\pi\sqrt{\bar{N}_n}}{2\sum_{n=1}^{N}\sqrt{\bar{N}_n}} \int_0^{R_{ap}} A(r) r \mathrm{d}r \tag{4.18}$$

$$2\pi \int_{R_{n-1}}^{R_n} A(r) r \mathrm{d}r = \frac{2\pi\sqrt{\bar{N}_n}}{\sum_{n=1}^{N}\sqrt{\bar{N}_n}} \int_0^{R_{ap}} A(r) r \mathrm{d}r \tag{4.19}$$

starting from $R_0 = 0$. As in the equi-amplitude case, after the polar coordinate ρ_n are found, Eq. (4.2) is applied to determine the angular coordinate.

Note that the application of this algorithm requires the *a priori* knowledge of not only the number of sub-arrays but also of the number of elements in each sub-array. From this point of view, it introduces additional complications when compared with the equi-amplitude placement algorithms. Nonetheless, the advantages following from the use of the technologically more convenient equi-power distribution largely compensate for this drawback. Moreover, as it will be shown in Paragraph 4.4.4, an efficient implementation of the sunflower placement calls upon the use of a reduced number of sub-array types (usually 3 or 4). Consequently, the optimization of the total number of sub-arrays and the relative ratio between the different types can be easily implemented.

4.4 Numerical validation of the technique

Several array configurations, corresponding to the four variants catalogued in Paragraph 4.3, will now be examined by assessing their performance against the stringent requirements in Appendix A. The design will constantly strive towards reducing the number of needed controls. In all the examples the arrays will work in circular polarization and will employ the basic patch radiator described in Appendix F. Sub-arrays composed of these patches will not take into consideration the effects of mutual coupling.

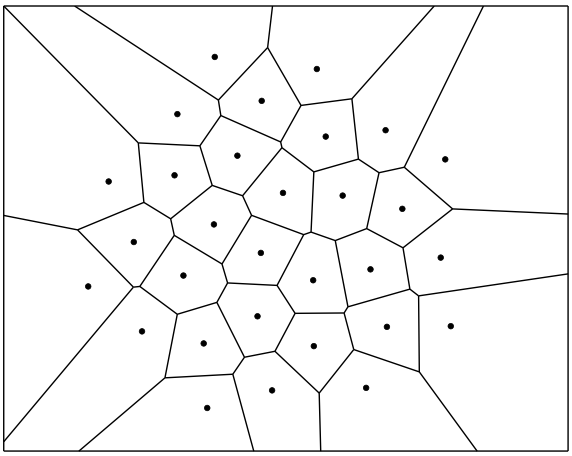

Figure 4.11: Example of Voronoi space subdivision [60]. Lines – the contours of the Voronoi cells; dots – enclosed phase centers.

4.4.1 Completely filled array - equi-amplitude

The idea consists of using the advantages coming from both a uniform tiling, such as a simple element placing, and the ones coming from non-uniform arrays, as the possibility to control SLL without amplitude taper and having no GL for spacing greater than λ between the sub-arrays. The array is composed of several square patches deployed on a regular triangular lattice [1]. Their field has been calculated firstly by implementing a classical analytical formulation [84] in Matlab and then it has been simulated designing the structure with the CST (Computer Simulation Technology) software [88]. Note that all examples cited in this section are based on the use of the square patch radiation patterns that were evaluated by means of the commercial software. Additional details on the design of the patch can be found in Appendix F.

The array is then divided into sub-arrays according to the *sunflower law*, with the position of the phase centers of the sub-arrays being derived with the formulation presented in Section 4.3.1.

Since an equi-amplitude feeding is assumed, Eqs. (4.9) and (4.2) can be straightforwardly applied. Around each phase center a Voronoi cell [60] is drawn (see Fig. 4.11), and all patches inside this cell are grouped into a sub-array. Note that the Voronoi surface division in Fig. 4.11, where each Voronoi cell is formed by grouping all points that are closer to the relevant phase

[1]The triangular lattice has been chosen as it guarantees better performances in terms of SLL and of elements packing (see Paragraph 2.3 and Appendix B).

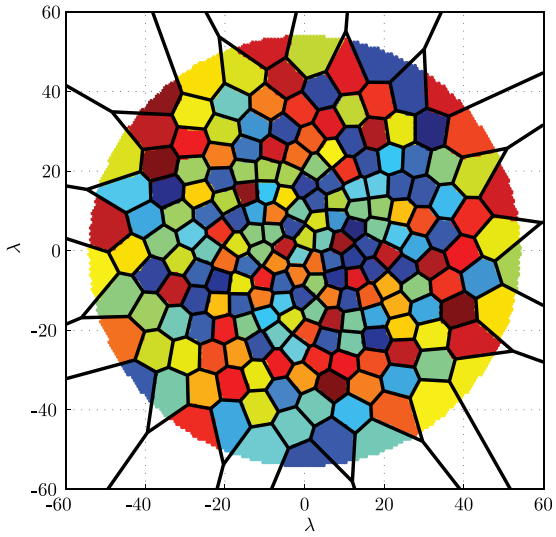

Figure 4.12: Positions of 200 sub-arrays in the 54λ aperture superimposed to the position of the elementary radiators. Different colours are used to distinguish the several sub-arrays.

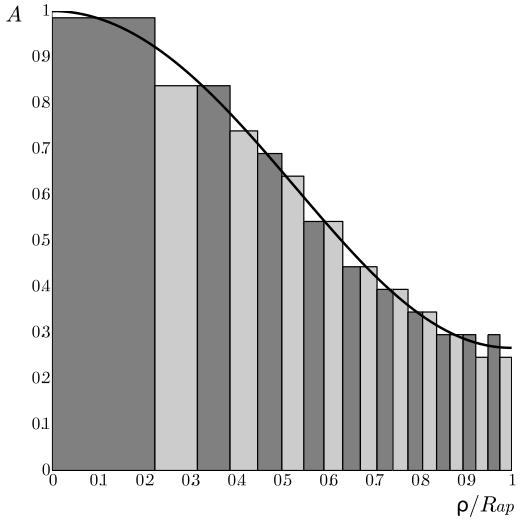

Figure 4.13: Amplitude and density taper for the non-uniform array configuration in Fig. 4.12. Thick black line – reference amplitude taper; alternate grey rectangles – normalized density taper.

center than to any other phase center, provides an optimum subdivision of the available real estate. In order to compute the array radiation pattern, the pattern of each sub-array is evaluated separately and then included in

the aggregate value by accounting for the phase term given by the position of the sub-array phase center in Eq. (2.16).

Since the Voronoi cell shapes are not too far from circular ones, the resulting sub-array patterns are rotationally symmetric. This is an important property when the beam is scanned. With this method the complete surface available is used while, at the same time, a very small number of controls (one for each sub-array) is needed.

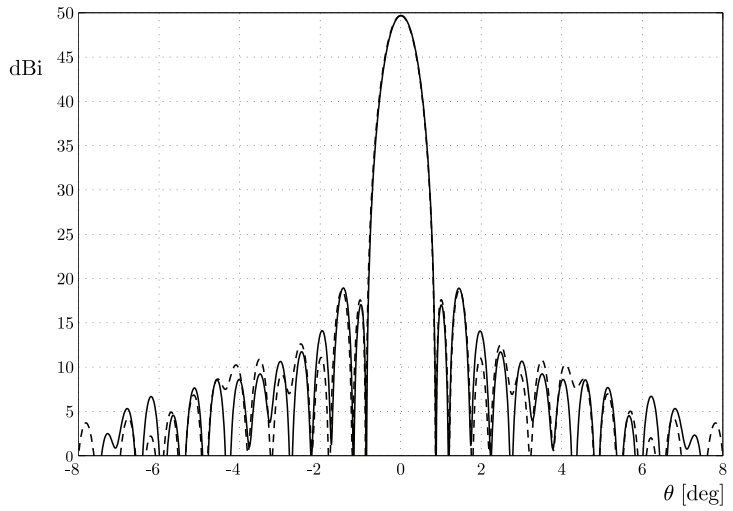

Figure 4.14: Pattern of the completely filled array in Fig. 4.12 for the beam pointed at boresight for two ϕ cuts. $\phi = 0°$ – continuous line; $\phi = 90°$ – dotted line.

The concept is now illustrated by discussing the case of the antenna shown in Fig. 4.12. It consists of 14647 square patches that are deployed on a uniform triangular lattice, the aperture having a circular shape of radius 54λ. The sub-array positions for $N = 200$ have been derived using Eqs. (4.9) and (4.2), following a Taylor taper [69] with SLL = 31 dB and $\bar{n}$=3 (see Appendix E). Note thatdifferent colours were used in the figure for distinguishing the sub-arrays, .

The sub-arrays correspond, in this case, to the Voronoi cells, possibly clipped by the aperture contour in the case of the cells at the periphery. The good agreement between the chosen reference amplitude taper and the achieved density taper is demonstrated in Fig. 4.13. The radiation pattern of the synthesized array is shown in Fig. 4.14. The design completely satisfies the requirements for boresight, maintaining a SLL under 19 dBi in the area of interest. Even when the beam is pointed at Europe's edges (see Fig. 4.16 and 4.15) the pattern remains compliant with the specifications coming from

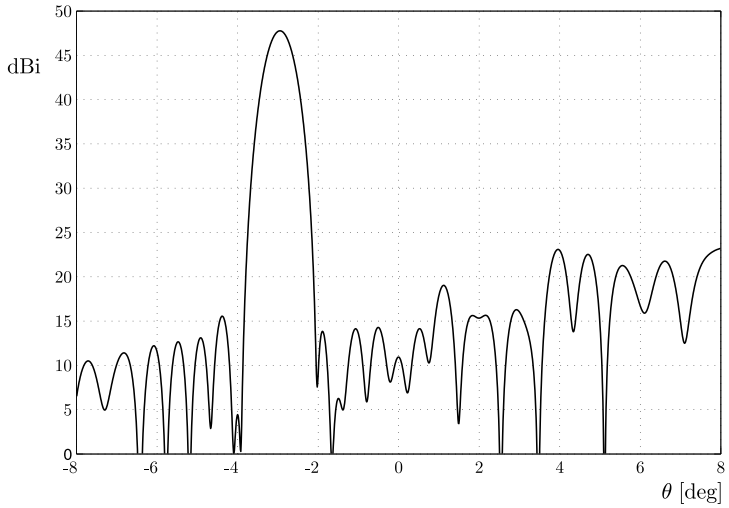

Figure 4.15: Pattern of the completely filled array in Fig. 4.12 for the beam pointed at Europe's edge.

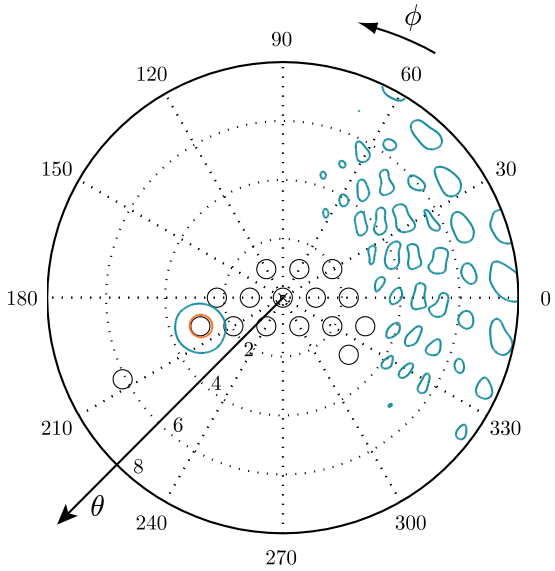

Figure 4.16: Contour plot pattern of the completely filled array in Fig. 4.12 for the beam pointed at Europe's edges. The regions enclosed by the black circles are the ones relevant to the interfering-beams using the same frequency. Red line – contour of the regions with directivity above 43.8dBi; blue line – contour of the regions with directivity above 20dBi.

[6]. From that figure it is evident that the proposed architecture satisfies the requirements:

- the directivity above the level required at the EOC, corresponding to the area enclosed by the red curve, overlaps the area to be illuminated.
- all regions pertaining to the interfering beams fall *outside* the region where the directivity exceeds the 20dBi level, corresponding to the areas enclosed by blue curves.

4.4.2 Non-completely filled array - equi-amplitude

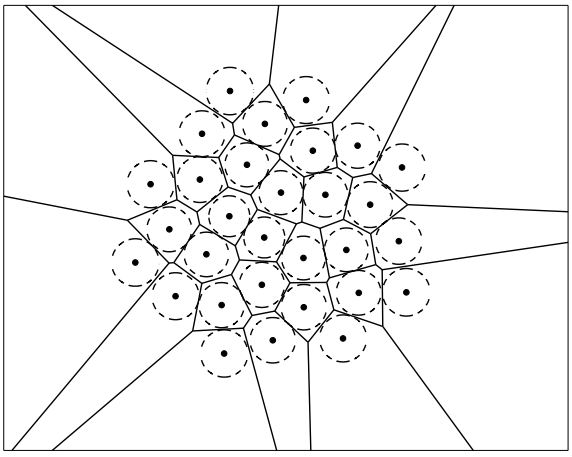

Figure 4.17: Example of Voronoi space tessellation. Lines – the contours of the Voronoi cells; dots – enclosed phase centers; dotted lines – circles inscribed in the Voronoi cells.

The configuration presented previously suffers from various implementation problems, one of them being the irregular shapes of the sub-arrays. In order to guarantee rotationally symmetric patterns, each sub-array should be as close as possible to a circle. As it turns out, generating non-overlapping circles that cover optimally a given (circular) area, can be easily achieved by resorting to a convenient property of the Voronoi tessellation [60], namely that all cells are convex and thus always allow for selecting inscribed circles. Consequently, after generating the Voronoi tessellation as in Paragraph 4.4.1, the relevant inscribed circles are drawn; the result of this operation is shown in Fig. 4.17. The next step is to group together the uniform array patches that are 'inside' any given circle (according to a predefined incidence criterion), while all other patches are discarded. This procedure ensures that

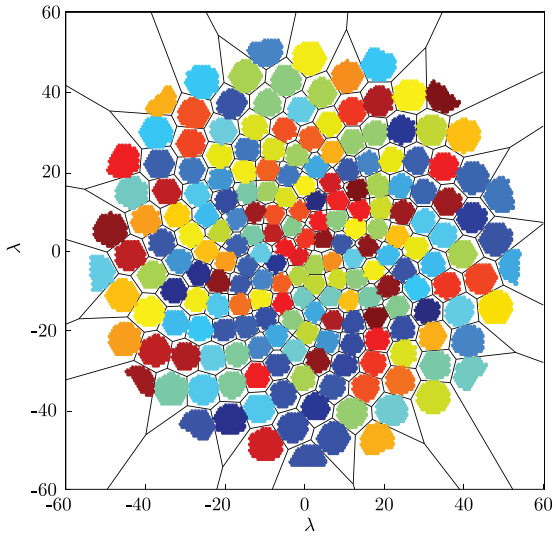

Figure 4.18: Positions of the 200 sub-arrays in the 54λ aperture superimposed to the position of the elementary radiators. Different colours are used to distinguish the several sub-arrays.

all sub-arrays have an (as-close-as-possible) circular shape except for some sub-arrays at the periphery. The same aperture dimension as in the previous example has been considered with a Taylor reference amplitude taper characterized by an SLL $= -30$dB and $\bar{n} = 3$ (see Appendix E).

The concept is now illustrated by discussing the case of the antenna shown in Fig. 4.18. Note that, as in the previous example, different colours were used for indicating distinct sub-arrays. They correspond, in this case, to the largest circles that could be enclosed in the Voronoi cells, possibly clipped by the aperture contour in the case of the cells at the periphery. The number of patches in this case amounts to 9435, that represents approximately 64% of the total number used in the array of Fig. 4.12. As expected, this reduction has an impact on the array pattern (see Figs.4.19). The main beam level drops by about 2 dB when compared with the one in Fig. 4.20. However, even though the number of patches used has been drastically reduced, the total array performance is still satisfying the requirements, as it can be appreciated from Figs. 4.19 and 4.21.

This type of configuration has a similar problem as the previously discussed one, namely since all sub-arrays are different, it is difficult to implement and to test the complete array in a modular fashion procedure.

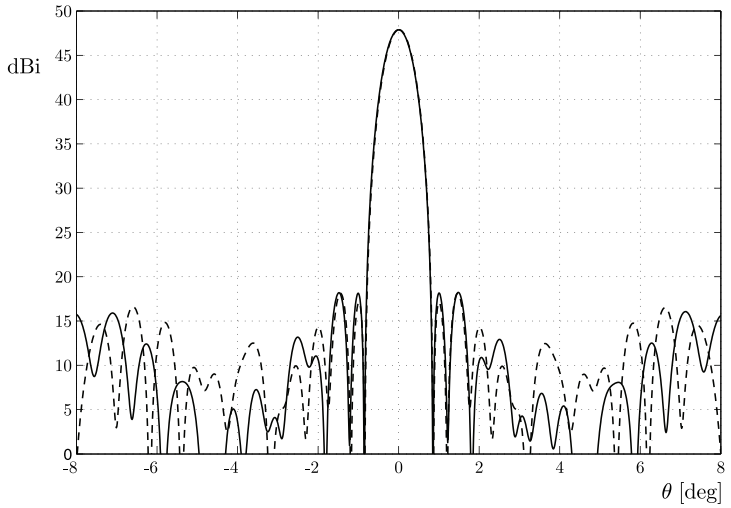

Figure 4.19: Pattern of the not-completely filled array in Fig. 4.18 for the beam pointed at boresight for two ϕ cuts. $\phi = 0°$ – continuous line; $\phi = 90°$ – dotted line.

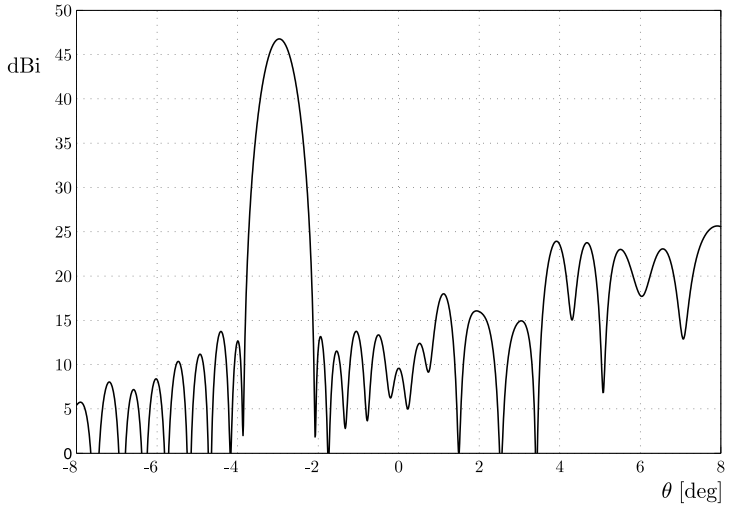

Figure 4.20: Pattern of the not-completely filled array in Fig. 4.18 for the beam pointed at Europe's edge.

4.4.3 Array of hexagonal sub-arrays - equi-amplitude

Although the configurations discussed thus far have an optimal performance in the field of view (FOV), they both are impeded upon by the irregularity of the sub-array shapes,this making their implementation difficult. From an

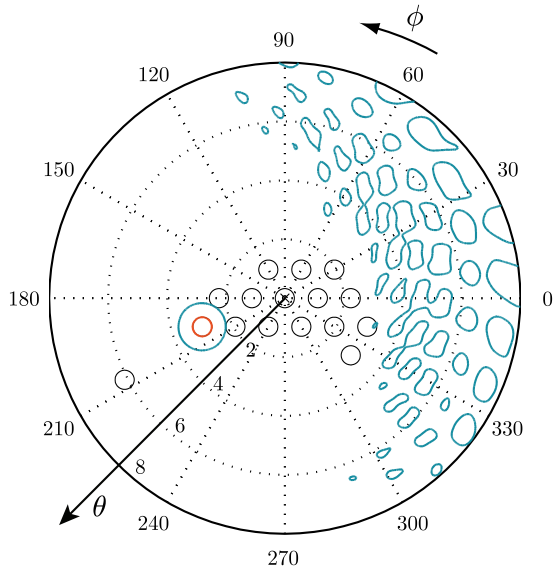

Figure 4.21: Contour pattern of the not-completely filled array in Fig. 4.18 for the beam pointed at Europe's edges. The regions enclosed by the black circles are the ones relevant to the interfering-beams using the same frequency. Red line – contour of the regions with directivity above 43.8dBi; blue line – contour of the regions with directivity above 20dBi.

industrial point of view, it is much more convenient to resort to a modular approach in which the amount of sub-array shapes is strongly reduced (down to 3 or 4). Several such configurations have been experimented with. In all cases the modules employed patch type elementary radiators deployed on uniform lattices. As the triangular lattice guarantees better performances in terms of SLL and of packing (see Paragraph 2.3 and Appendix B), it has been preferred to the rectangular one. Furthermore, it was strived towards ensuring a reduced number of elements per sub-array in order to be able to design the small modules that are needed in the dense central area of the sunflower arrays. With these considerations, the hexagonal modules provided the best approximation of the circular shape.

After selecting the limited number of modules, the placement strategy followed the same approach as in Paragraph 4.4.1. The aperture is initially subdivided according to the Voronoi tessellation and then the module that fits best is accommodated in each cell. In a few cases there were occurrences of sub-arrays that overlapped, a situation that was easily remedied by slightly shifting the relevant sub-arrays.

The concept is now illustrated by discussing the antenna shown in

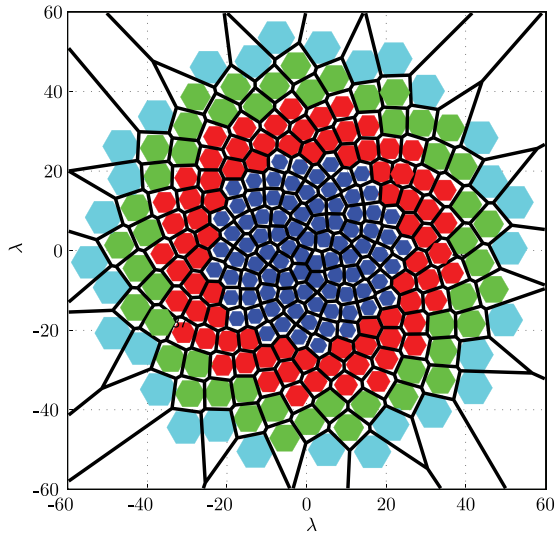

Figure 4.22: Positions of 250 hexagonal, equi-amplitude sub-arrays. Different colours are used to distinguish the several sub-arrays: blue – sub-arrays composed of 19 patches; red – sub-arrays composed of 37 patches; green – sub-arrays composed of 61 patches; light blue – sub-arrays composed of 91 patches.

Fig. 4.22. Four different kind of hexagons were chosen; in all of them the elementary radiators are deployed on a triangular lattice in rings around a central element. The following type of sub-arrays were used:

- 90 sub-arrays composed of 19 patches (two rings around the central element);
- 80 sub-arrays composed of 37 patches (three rings around the central element);
- 50 sub-arrays composed of 61 patches (four rings around the central element);
- 30 sub-arrays composed of 91 patches (five rings around the central element),

the total number of patches ammounting to 10450. This configuration replicates the performances of a 55 λ radius aperture, on which a Taylor taper law with SLL = 33 dB and $\bar{n}$=3 has been applied on the array element excitations (see Appendix E).

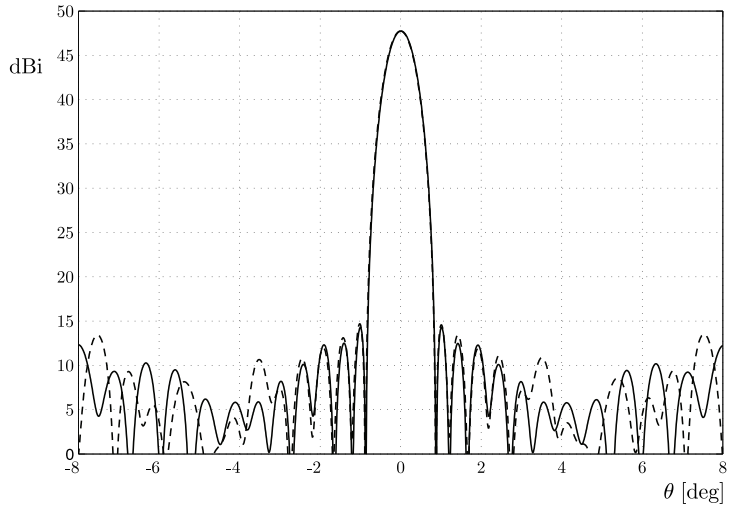

Figure 4.23: Pattern of the hexagonal sub-arrays configuration in Fig. 4.22 for the beam pointed at boresight for two ϕ cuts. $\phi = 0°$ – continuous line; $\phi = 90°$ – dotted line.

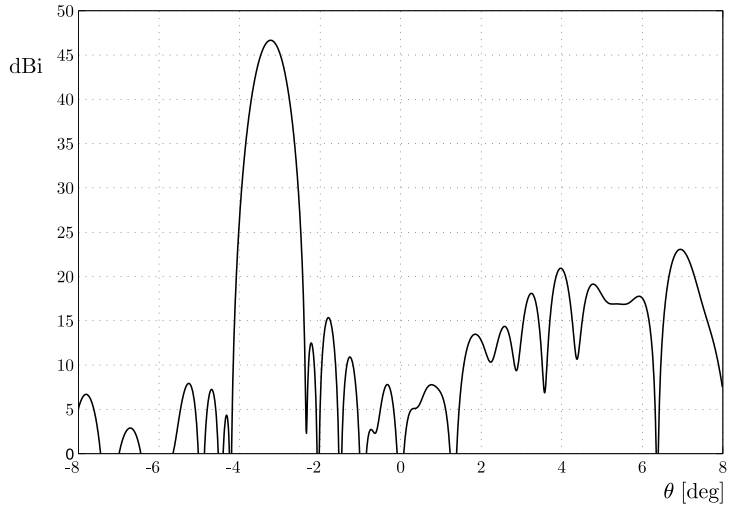

Figure 4.24: Pattern of the hexagonal sub-arrays configuration in Fig. 4.22 for the beam pointed at Europe's edge.

Note that, also in this case, different colours were used for indicating distinct sub-arrays corresponding to the largest hexagonal sub-arrays that could be enclosed in the relevant Voronoi cells.

As it is possible to notice from Figs. 4.23 and 4.24, this type of configu-

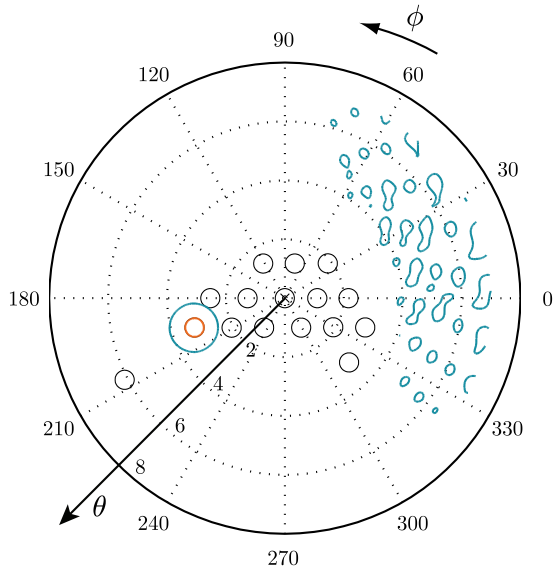

Figure 4.25: Contour pattern of the hexagonal sub-arrays configuration in Fig. 4.22 for the beam pointed at Europe's edges. The regions enclosed by the black circles are the ones relevant to the interfering-beams using the same frequency. Red line – contour of the regions with directivity above 43.8dBi; blue line – contour of the regions with directivity above 20dBi.

ration is performing excellently both when the beam is pointing at boresight and when it is scanned. In this last case, it is possible to note from Fig. 4.25 how the regions where the directivity is higher than the 20 dBi level, imposed by the requirement not to be exceeded in the interfering beam areas, are separeted from the interfering areas enclosed by the black circles. From technological point of view, this option offers the possibility to implement and test just 4 sub-array types and permits satisfying the requirements with a reduced number of controls (N=250). The main drawback of all the configurations presented thus far is that guaranteeing the same level of amplitude to sub-arrays composed of a different number of radiators is difficult to implement without introducing different kinds of amplifiers at array level. This is not desirable from an implementation point of view for which using identical amplifiers that operate at the same, optimized level is to be preferred.

4.4.4 Array of hexagonal sub-arrays - equi-power

In order to overcome the technological difficulties coming from the equi-amplitude choice, an array with equi-power sub-array feeding is here pro-

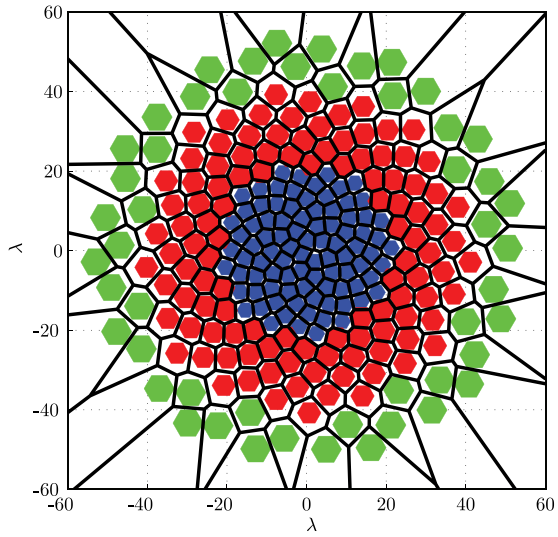

Figure 4.26: Positions of the 250 hexagonal, equi-power sub-arrays. Different colours are used to distinguish the several sub-arrays: blue – sub-arrays composed of 19 patches; red – sub-arrays composed of 37 patches; green – sub-arrays composed of 61 patches.

posed. In the following example only three sub-array configurations were used in the array implementation. In this case the sub-array phase center positions have been found using Eqs. (4.18) and (4.2) and choosing from the beginning the number and kinds of sub-arrays to be employed in the design. Subsequentially, as in the previous examples, the phase center positions are used to draw the pertaining Voronoi cells. In each cell, a hexagon, whose dimensions and properties have been defined before finding the phase center position, is placed. In case of overlapping between hexagons, the sub-array phase centers have been slightly moved.

The concept is now illustrated by discussing the case of the antenna shown in Fig. 4.26. In it, the first type of sub-array consists of 7 patches arranged on a triangular lattice and in an hexagonal shape; the other types have been obtained by adding, still on a triangular lattice, one and two rings more to the first configuration. The total number of controls used equals $N = 250$ and the relevant phase center positions, computed with the formulation introduced in Paragraph 4.3.2, are the centers of the hexagons in Fig. 4.26. Note that, also in this case different colours were used for indicating distinct sub-arrays that correspond, in this case, to the *a priori* chosen hexagonal sub-arrays. As already mentioned, the hexagon dimensions are chosen independently of the pertaining Voronoi cell; for this reason some

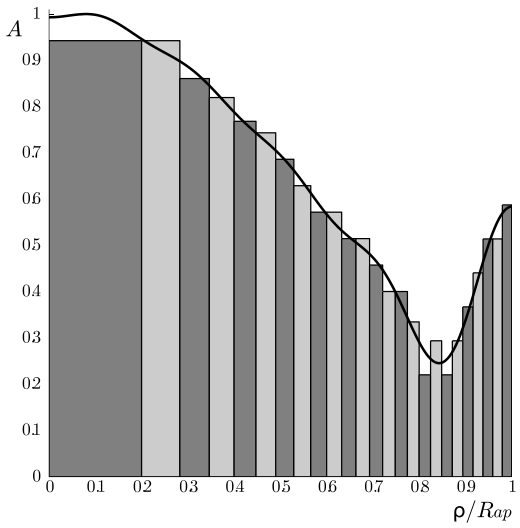

Figure 4.27: Amplitude and density taper for the non-uniform array configuration in Fig. 4.26. Thick black line – reference amplitude taper; alternate grey rectangles – normalized density taper.

overlapping between different sub-array may occurr and thus the hexagons are not always enclosed in the Voronoi cells.

Even in this case the comparison between the reference amplitude taper (here chosen to be a Taylor distribution with SLL = 31 dB, $\bar{n} = 10$), reported in Fig. 4.27, shows that the presented technique is able to match the amplitude taper assigned. According to the formulation developed for the equi-power case and after dividing the available aperture in equi-pollent annular rings, not only the number of elements belonging to each annular ring should be taken into account but also the relative amplitude weight, according to Eq. (4.13). It is important to notice that a good match between amplitude and density taper can be achieved even when the reference amplitude distribution is not monotonically decreasing. Figure 4.28 represents the radiation pattern in dBi for the beam pointing at boresight for two ϕ cuts, $\phi = 0°$ and $\phi = 90°$ in continuous and dotted line, respectively.

Figure 4.28 shows the radiation pattern of the synthesized array. In the central region, up to about 5° the directivity pattern can be considered almost rotationally symmetric; this is due, as in the previously analysed cases, to the particular phase center positioning in the *sunflower* configuration. We note that for boresight the SLL are respecting the requirements with a large margin; when the beam is pointed at Europe's edges (see Figs. 4.29 and 4.30) the area where the SLL is under the imposed level, even if still satisfying the

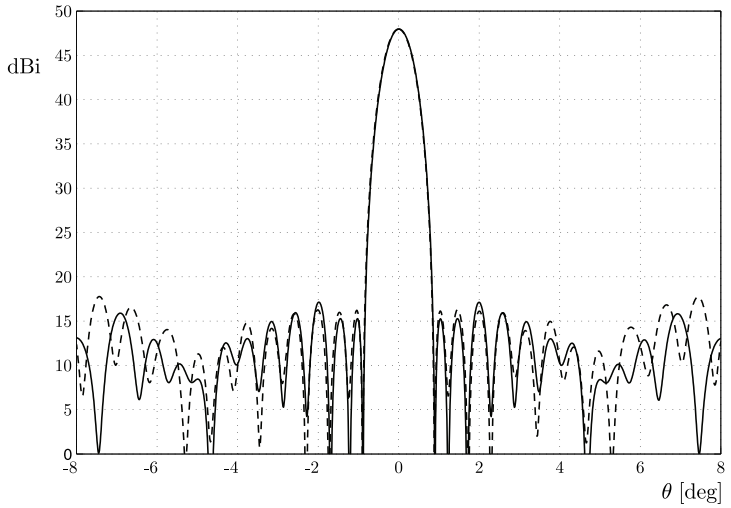

Figure 4.28: Pattern of the hexagonal sub-arrays configuration in Fig. 4.26 for the beam pointed at boresight for two ϕ cuts. $\phi = 0°$ – continuous line; $\phi = 90°$ – dotted line.

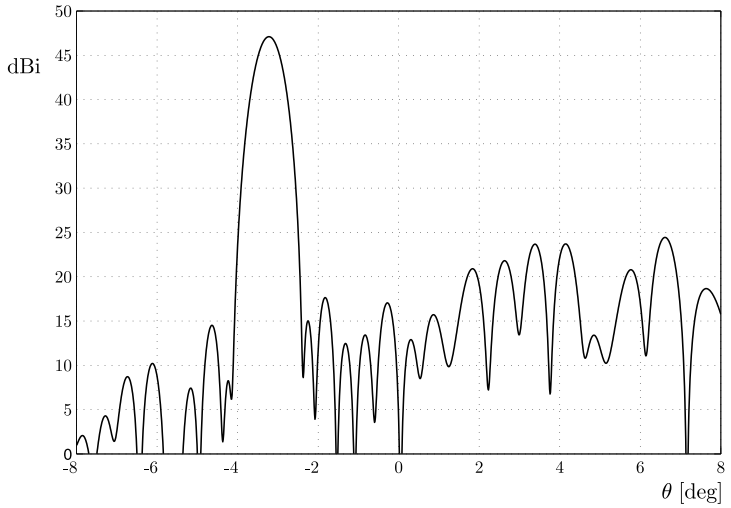

Figure 4.29: Pattern of the hexagonal sub-arrays configuration in Fig. 4.26 for the beam pointed at Europe's edge.

constraints, is quite limited.

We remind that, from a technological point of view, this configuration is the easiest to be implemented among the variants examined in this chapter.

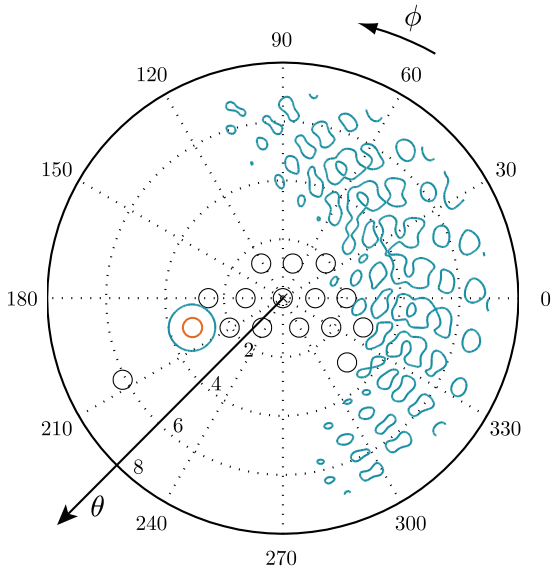

Figure 4.30: Contour pattern of the hexagonal sub-arrays configuration in Fig. 4.26 for the beam pointed at Europe's edges. The regions enclosed by the black circles are the ones relevant to the interfering-beams using the same frequency. Red line – contour of the regions with directivity above 43.8dBi; blue line – contour of the regions with directivity above 20dBi.

4.5 Concluding considerations

In this chapter several innovative concepts were introduced:

- The possibility to shape the pattern resorting to a non-uniform placement of the array elements has been demonstrated.
- A normalized density taper has been defined. This parameter has been shown to allow mapping a reference amplitude taper on a synthesized density taper.
- An analytical law for the placement of identical equi-amplitude elements with a density taper matching a reference amplitude taper, has been developed. The directivity pattern of the proposed synthesized array is in good agreement with the one achievable by imposing the reference amplitude taper on a uniformly spaced array.
- An analytical law for the placement of identical equi-power sub-arrays, with a density taper matching a reference amplitude taper, has been

developed. The directivity pattern of the proposed synthesized array is in good agreement with the one achievable by imposing the reference amplitude taper on a uniformly spaced array.

- Both the innovative placement techniques mentioned before have been extended to the case of differently sized sub-arrays, resulting in the possibility to synthesize arrays with an improved aperture coverage efficiency.

- Several possible configurations, based on the concepts presented in this chapter, have been simulated and their pattern behaviour and technological implementation discussed at length.

Chapter 5

Physical validation of the 'sunflower' placement strategy

The previous chapter discussed in detail an innovative synthesis technique, the so-called 'sunflower' placement method. Due to its versatility, the applicability of the method was extended by allowing the use of a small number of sub-array types, a procedure that immediately yielded a significant reduction in the needed controls.

This effective array antenna synthesis method is now validated by means of a combination of measurements and off-line processing, allowing the simulation of very large arrays of the kind that is required by the demanding application defined in Appendix A. To this end, a specialized module was manufactured based on a high performance design of Thales Alenia Space and sub-arrays consisting of 1, 2, 3 or 4 such modules were assembled and measured. The results of these sub-array measurements will be firstly discussed in detail and then post-processed for simulating the large array designed with a sunflower law. The synthesized array performance will be evaluated for a number of relevant situations, thus demonstrating the suitability of the proposed array configuration for the mission that is aimed at. The performances of such an array are finally compared with a reference uniformly spaced array configuration. The chapter will be completed by concluding remarks.

5.1 Experimental setup

5.1.1 The choice for the sub-array configuration

The analysis in Paragraph 4.4.4 has clearly demonstrated the superior performances that are obtained by employing an even reduced number of sub-array types (i.e. 3 or 4) in the sunflower architecture. In view of a proper filling of the convex Voronoi cells, the sub-arrays were taken to have a hexagonal shape that makes use in an optimal manner of the convenient triangular lattice properties (see Appendix B). Based on this observation, the first choice for the physical implementation of the sunflower would have been the use of custom designed hexagonal sub-arrays of the type employed in Fig. 4.26. Nevertheless, the design and implementation of such specialized devices would have required a significant design and experimentation time while adding little conceptual novelty to this investigation. From this point of view, the use of off-the-shelf devices was deemed a much more effective choice. In view of the specific mission requirements (see Appendix A), a clear preference was given to array antennas providing excellent impedance matching properties in combination with circular polarization operation. However, an analysis of the market has shown that such modules are not easily available. The next best option was then to replicate a verified design that provided the needed functionality without requiring excessive production costs. This option turned out to be feasible, as hereafter described.

Discussions with the project partners at ESA-ESTEC and Thales Alenia Space have put forward the availability of a high performance circularly polarized 4×4 patches module in the Thales Alenia Space portfolio, the documentation of which the company was willing to hand over to TU Delft for manufacturing and testing. When compared with the initial placement experiments reported in Paragraph 4.4.4, the relevant module deviated in the sense that it had a quadrilateral, as opposed to hexagonal, shape. This required small adjustments of the array architecture that could be easily carried out due to the demonstrated versatility of the sunflower placement strategy. The quadrilateral shape, in turn, offered interesting opportunities, such as the assembling of sub-arrays with shapes better suited to beam-scanning over the rectangular area that encloses Europe (see Paragraph 5.2.2). Another deviation concerned the module's operational bandwidth that was centred around 7.5 GHz, significantly lower than the mission requirements in Table A.1. However, this operational bandwidth fitted optimally the characteristics of the IRCTR measurement facility – DUCAT (see Paragraph 5.1.4) – that is tuned to the X-band.

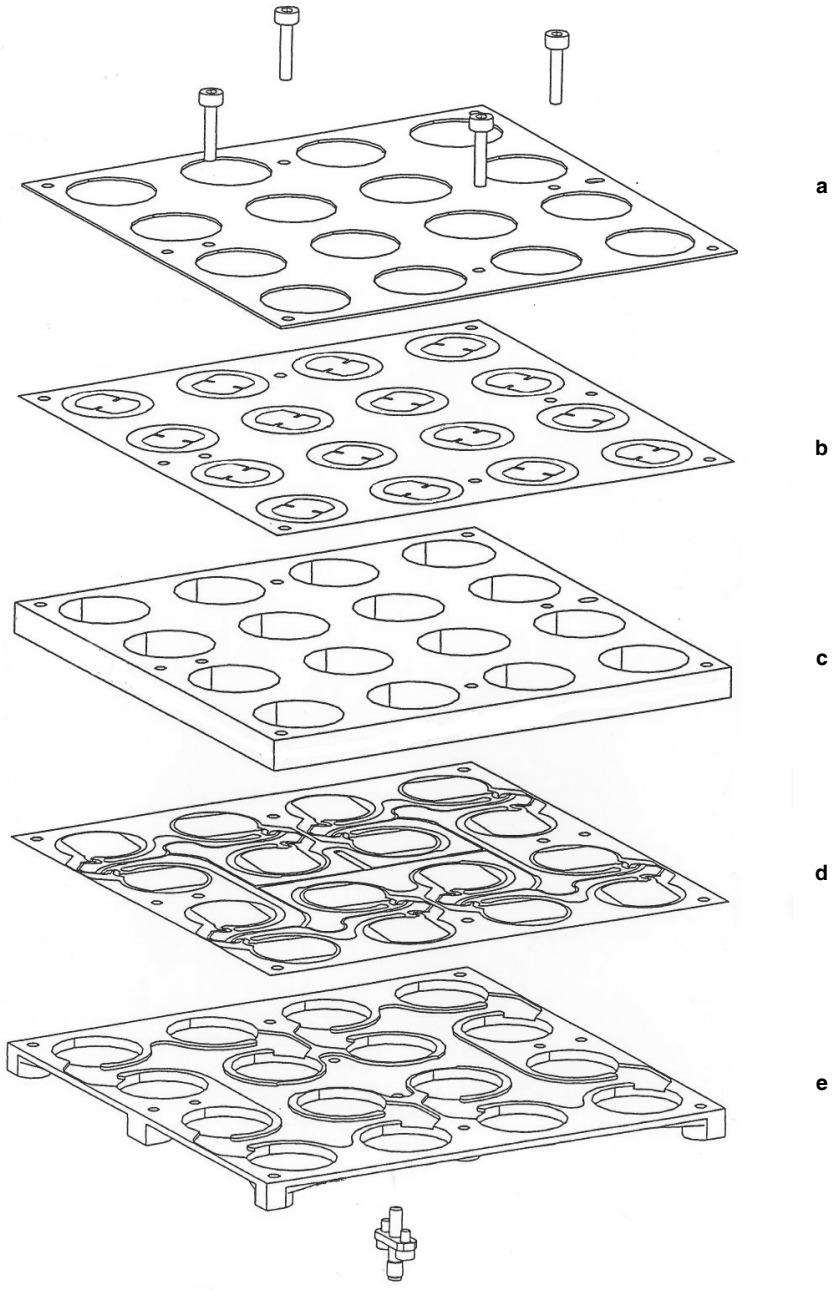

Figure 5.1: The structure of the manufactured tile. (a) Upper aluminum flange with circular apertures; (b) upper PCB layer with parasitic patches; (c) central aluminium layer with circular cavities and the upper part of the stripline cavities (obscured at the lower side of the plate); (d) lower PCB layer with active patches and routing stripline traces; (e) lower aluminium base with the back-side of the circular patches and the lower part of the stripline cavities.

In the followings, the manufactured basic tile will be firstly introduced. A brief description will be subsequentially given to the measurement panel employed for assembling the various sub-array variants. The measurements of the different sub-array configurations will be discussed and finally these results will be combined to compute the total array radiation pattern.

5.1.2 Manufactured basic sub-array – the tile

The basic tile (see Fig.5.1) was designed and firstly manufactured in Thales Alenia Space. By using the provided documentation it was replicated in four copies in the workshop of the Delft University of Technology, with parts of them being outsourced to CIRE in France. The tile consists of milled aluminium plates and etched copper plated microwave laminates that are stacked and fastened together. The elements comprised by the tile and their specific role are now presented, grouped by their function, by starting from the lower radiating layer (d) and the upper one (b) and ending with the aluminium layers (e), (c) and (a).

On the lower PCB layer the radiating patches and their feeding lines have been etched from a thin copper plated microwave laminate, as shown in level (d) in Fig. 5.1. The feeding of the active patches in the layer (d) is achieved by means of striplines that are etched on the same level. The metallic enclosures needed for creating the stripline have been milled from the aluminium panel above and below. The feeding signals are distributed via a fixed power distribution network that branches out from a single feeding connector (see Fig. 5.1). The distribution network was optimised at TAS for ensuring the extremely uniform amplitude and phase shifts that are needed by the individual radiators. Nevertheless, the fact that the tile has one single access port does not allow the measurement of individual elements and thus, such effects as the inter-element coupling could not be quantified. The upper PCB layer, level (b), accommodates 16 parasitic patches re-radiating the field received from the patches in the lower PCB. The particular relative rotation of the patches in the layers (b) and (d) together with a proper phase shift between the radiators, guarantees an almost perfect circular polarization in the main beam region.

The other three levels (a), (c), and (e) are realized in aluminium. In the lowest level ((e) in Fig. 5.1) part of the metal has been removed in order to create cavities around the patches at level (d). In the same way also the middle level (c) has been machined on the rear side (not visible in the figure) in order not to short circuit the feeding lines of level (d). The thick metal layer (level (c) in Fig. 5.1) creates perfectly round walls around

Figure 5.2: Completely assembled tile. The 16 parasitic patches are visible.

the patches ensuring that the patches in level (b) are excited via cylindrical circular waveguide modes. Finally, the last metal layer permits fastening the whole structure together, guaranteeing the rigidity and flatness of the structure and, in particular, of the radiating level (b) that would otherwise bend resulting in a distorted radiated field. Moreover, this final metallic flange suppresses the surface currents propagating at the free-space interface with the dielectric. Despite the fact that the layers (a), (c) and (e) are fabricated from aluminium, their largely hollow structure implies that their weight is quite low. Nevertheless, the metallic structure ensures structural rigidity that is extremely favourable for guaranteeing a stable, repeatable radiation performance. The completely assembled tile, shown in Fig. 5.2, is thus a robust and light structure.

5.1.3 The mounting panel for measurements

Two circular panels were designed in order to measure the radiation patterns of the different sub-arrays (see Figs. 5.3 and 5.4). The smaller one consists of a 8 mm thick circular, plastic panel with a diameter of 200 mm. The second panel consists of a 15 mm thick plastic disk, with a diameter of about 600 mm and several holes around the perimeter in positions such that a measurement of the pattern every $\phi = 15°$ becomes possible.

The pattern of small circular holes in the central area of the panel allow mounting the tiles in various positions. The larger holes are meant for providing the possibility to connect the feeding coaxial cables to the tile connectors. Their shape was chosen to allow maximum freedom for tile

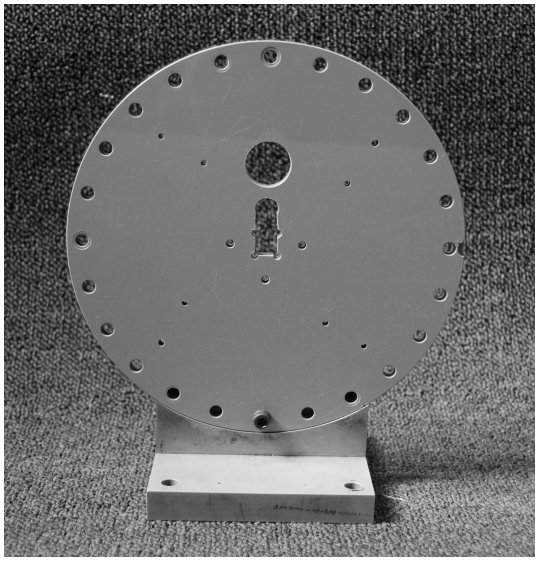

Figure 5.3: Small panel for the measurement of the single tile.

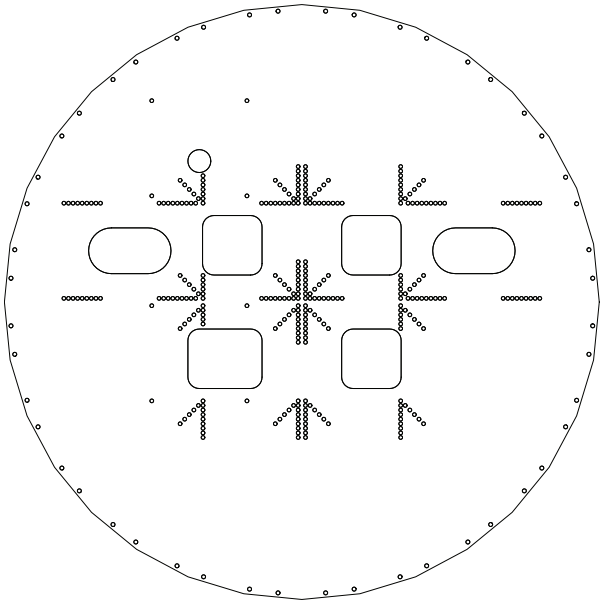

Figure 5.4: The front side of the larger measurement panel

placement, while ensuring the needed structural rigidity.

Whenever it was not possible to obtain a symmetrical mounting (with respect to the panel centre) of the sub-array to be measured, the position

of the mounting column along the x and y axis was adjusted such hat to minimize the placement error.

5.1.4 Measurement setup

IRCTR is endowed with an anechoic chamber facility of moderate size, $3\,\mathrm{m} \times 3\,\mathrm{m} \times 6\,\mathrm{m}$, (see Fig. 5.5) called Delft University Chamber for Antenna Tests (DUCAT). The self-made design was built by the faculty workshop in 1979 and was initially used for far-field off-line measurements of antennas that are small relative to the wavelength. Since 1992, the laboratory has been developing near-field antenna measurements for antennas that are large relative to the wavelength in DUCAT. Before the absorbers were placed, the entire chamber was covered with copper plates of 0.4 mm thickness thus forming a Faraday cage. There are three 30cm-deep pits in the floor, which are connected by ducts. In the pits, the far-field positioners and a near-field planar scanner are placed in such ways that their main bodies are below the surface. The distance between the two positioners is around 3.5 m and the distance between one of these and the near-field planar scanner is maximally 1.5 m. To maintain a completely shielded chamber, the doors are of a special design. They are not suspended on hinges, but pulled by pneumatic cylinders. The shielding of the chamber is for frequencies above 2 GHz up to 18 GHz and it is at least 120 dB all around. All walls are covered with pyramidically shaped absorbers. It is found that the walls have a reflection coefficient of less than -36 dB.

The DUCAT measurement system consists of time domain and frequency domain equipments. The frequency domain equipment allows measurements up to 50 GHz and includes the following components:

- PC for controlling the equipment and executing automated measurements controlling the antenna positioners.
- E8364B PNA Network Analyzer working from 10 MHz to 50 GHz with 104 dB of dynamic range, smaller than 0.006 dB trace noise and with a measurement speed smaller than 26 μs/point for 32 channels and 16,001 points.
- HP 8341 B synthesized sweeper (RF source); this accurate synthesized stepped sweeper provides 10 dBm of power in the frequency band from 10 MHz to 20 GHz.
- Standard Gain Horns at different frequency bands for the determination of the absolute gain of the antenna under the tests.

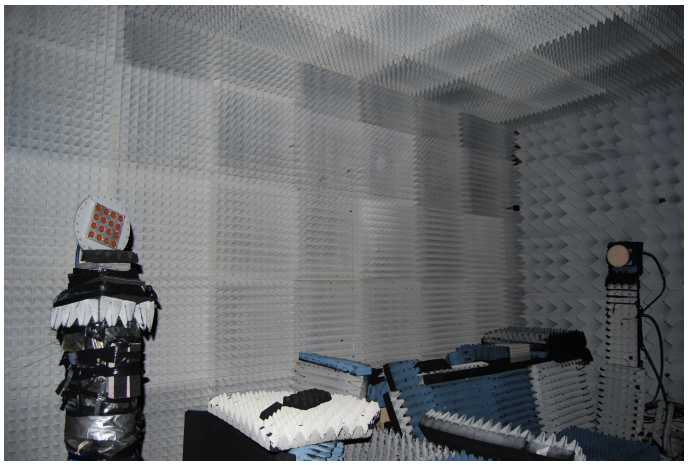

Figure 5.5: Set-up in the anechoic chamber for the sub-array measurements. On the left the measuring column with the small panel and one sub-array; on the right a standard horn.

5.2 Measurement results

This section discusses the measurement of the principal antenna parameters of the employed sub-arrays. Initially the single tile, constituting the basic brick in all sub-array types (see Paragraph 5.1.2), will be used to measure the scattering parameters and the polarization purity. The radiation pattern characteristics of the sub-array configurations will then be discussed.

5.2.1 Measurement of the tile parameters

In this paragraph the measurement of the scattering parameters and the polarization purity of the single tile sub-array are reported.

A first experiment concerned the assessment of the matching properties of the manufactured tiles and the coupling between two closely packed (in fact, touching) tiles over a relatively broad frequency range around the design frequency of 7.5 GHz. These parameters were measured at the corporate feeding ports of the tiles, yielding a two port system for which the standard S_{11} and S_{12} parameters defined in Paragraph 2.1.3 were accounted for. The measured results are reported in Fig. 5.6. The S_{11} behaviour evidences an operational bandwidth stretching between 6.8 GHz and 7.9 GHz for a (very demanding) $S_{11} < -20$dB condition. As for the coupling, measured with both the tile connectors in position down (see Fig. 5.8), its values

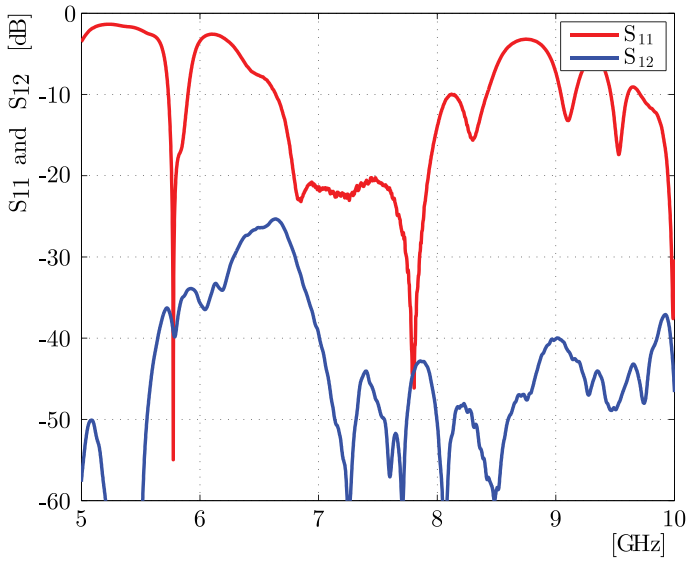

Figure 5.6: S_{11} and S_{12} parameter of the assembled tile measured in a frequency range around the operational one.

are below −30dB in the operational bandwidth and under −50dB at the design frequency. These low values can be explained by considering the distance between the tiles (minimum of $2.8\,\lambda$) and the directive pattern of the tile, as it will be shown in Paragraph 5.2.2. This experiment is be supplemented with two repeatability studies. To begin with, recall that four tiles were manufactured. It is then necessary to assess the spreading of the reflection coefficients pertaining to the four tiles, these results being collected in Fig. 5.7. The figure dewmonstrates that the replicated tiles behaviour is in good agreement with the one of the original tile, [1] even though the level of the four S_{11} curves is slightly worse than the one of the reference case and the curves are marginaly moved toward lower frequency. These two effects have been caused by the substitution of the not anymore available PCB material Arlon HI3003Q ($\epsilon_r = 3.9$ tickness = 0.1397 mm) used in the reference tile with the Arlon 25FR one ($\epsilon_r = 3.58$ tickness = 0.1524 mm).

The tile in Fig 5.1 is, in principle, symmetric. One simple way of checking the physical symmetry of the manufactured tile is by measuring the coupling between two neighbouring tiles for their 4 possible relative positions obtained by keeping one fixed (connector down in Fig. 5.8) and rotating the other by 90°. The relevant measurement results are shown in

[1] Measurements of the reference tile can not be distributed due to intellectual property issues.

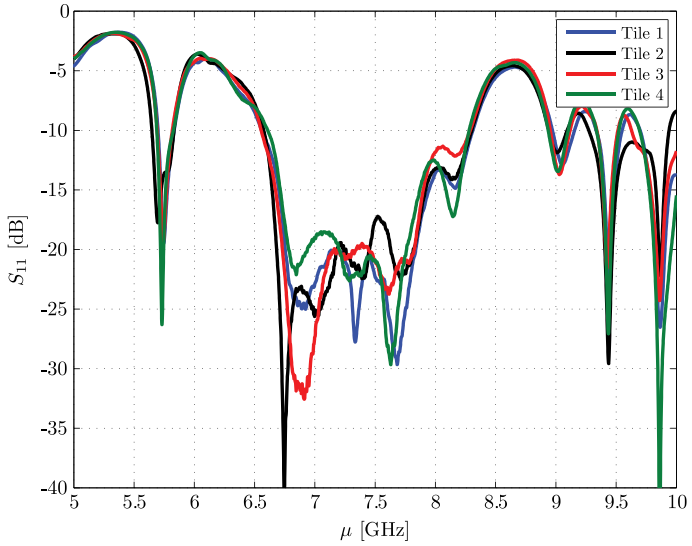

Figure 5.7: S_{11} parameter for the 4 tiles.

Fig. 5.9. Taken the preferred position as the one in which the connector is

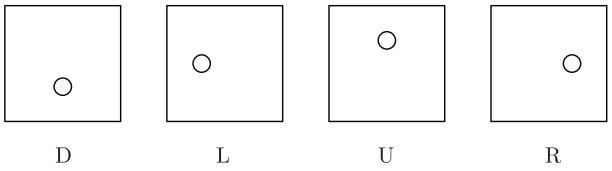

Figure 5.8: Four possible relative positions of the tile (with the connector Down, Left, Up and Right, respectively).

at its lower possible position, the four cases considered have been denoted in the legend as DD corresponding to the case of having both connectors in position down, DL for the second connector placed on the left, DR for the second connector placed on the right side and finally DU for the second connector placed on the top side of the sub-array tile. The four curves in the figure are quite similar, especially in the considered interval of operational frequencies.

The second experiment comes from the need to know the inter-tile coupling for variable spacing, a characteristic that is required by the sub-arrays in the *'sunflower'* architecture being located at largely variable spacing. The coupling was measured for the 'preferred' tile relative orientation at 3 frequencies in the operational bandwidth, the results being shown in Fig. 5.10. As expected and demonstrated by the figure, the coupling between the two

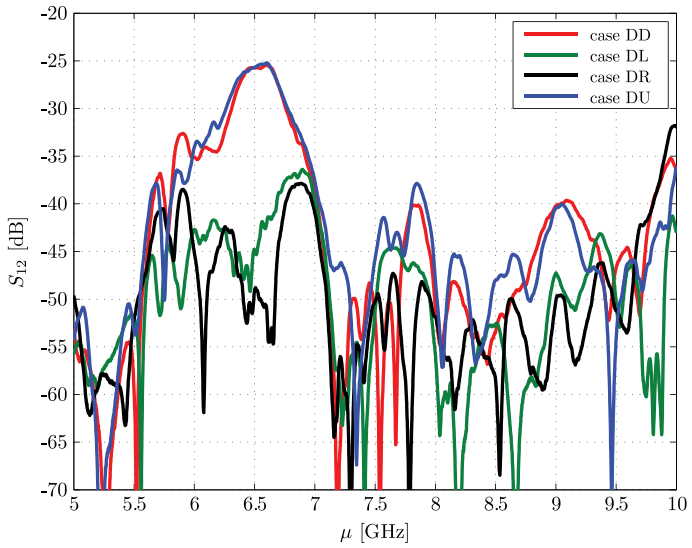

Figure 5.9: S_{12} parameter in the cases of having the two tiles in the possible four different relative orientations.

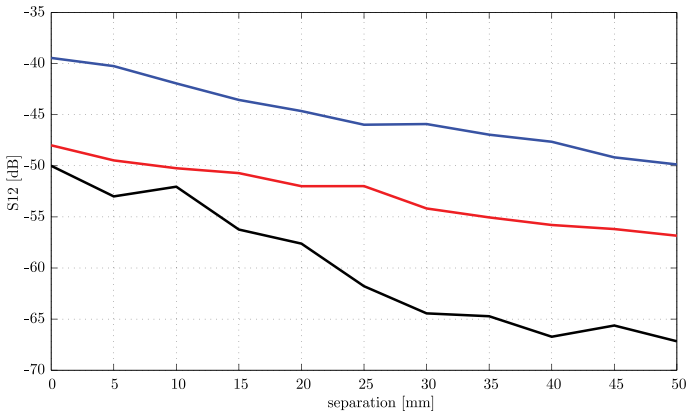

Figure 5.10: S_{12} for the central frequency 7.5 GHz – red curve, lowest 7 GHz – blue curve, highest 8 GHz – black curve, as function of the distance between two tiles.

identical tiles diminishes by increasing the relative distance between the radiator centres.

The third experiment concerned the polarization purity of the field radiated by the tile for two elevation angles $\theta = 0°$ (boresight) and $\theta = 4°$ corresponding to the maximum scanning angle that is of relevance for European geostationary satellite applications.

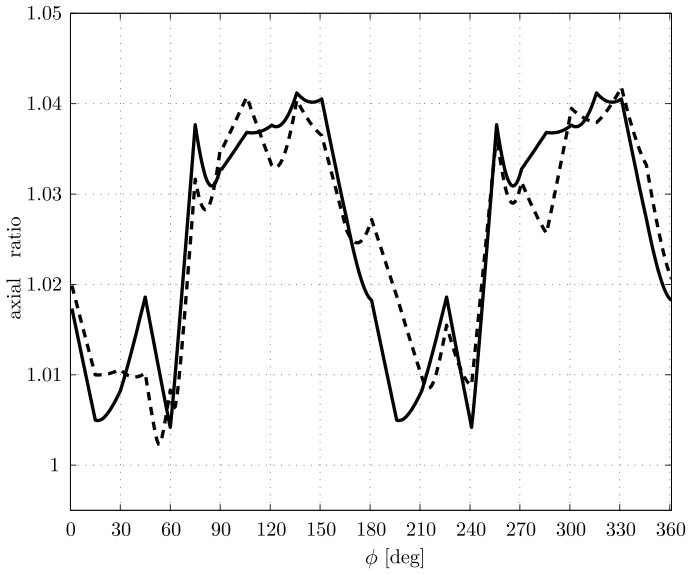

Figure 5.11: Axial ratio of the two field components for $\theta = 0°$ – continuous line, and $\theta = 4°$ – dotted line.

The polarization purity is examined by computing the axial ratio [2, (p. 67)] with the formula

$$\mathrm{AR}(\theta,\phi) = \frac{|\bar{\mathrm{AO}}(\theta,\phi)|}{|\bar{\mathrm{BO}}(\theta,\phi)|} \tag{5.1}$$

where $\bar{\mathrm{AO}}$ and $\bar{\mathrm{BO}}$ are the vectors identifying the polarization ellipse in Fig. 2.1, namely

$$|\bar{\mathrm{AO}}(\theta,\phi)| = \left\{\frac{1}{2}\left[|E_\theta(\theta,\phi)|^2 + |E_\phi(\theta,\phi)|^2 + \left[|E_\theta(\theta,\phi)|^4 + |E_\phi(\theta,\phi)|^4 + 2|E_\theta(\theta,\phi)|^2|E_\phi(\theta,\phi)|^2\cos(2\Delta)\right)\right]^{\frac{1}{2}}\right]\right\}^{\frac{1}{2}} \tag{5.2}$$

and

$$|\bar{\mathrm{BO}}(\theta,\phi)| = \left\{\frac{1}{2}\left[|E_\theta(\theta,\phi)|^2 + |E_\phi(\theta,\phi)|^2 - \left[|E_\theta(\theta,\phi)|^4 + |E_\phi(\theta,\phi)|^4 + 2|E_\theta(\theta,\phi)|^2|E_\phi(\theta,\phi)|^2\cos(2\Delta)\right)\right]^{\frac{1}{2}}\right]\right\}^{\frac{1}{2}} \tag{5.3}$$

From these expressions it can be easily seen that the axial ratio amount to 1 for the aimed at right hand circular polarization. Even though some little disalignement errors are present, the measured results, shown in Fig. 5.11 are in good agreement with the expected values.

5.2.2 Radiation pattern measurement results

The sub-division of a large planar array into a number of sub-arrays is an interesting topic from both theoretical and technological point of view. As shown in Chapter 4, the problem can be addressed in different ways, resulting in a wide spread of possible solutions. Note that, for industrial reasons, one should keep the number of different sub-arrays as low as possible. As concerns the size, sub-arrays that are large with respect to wavelength are preferred in order to reduce the number of active chains. Conversely, upper bounds of the sub-array dimensions also apply. One such limit follows from the FOV requirements since increasing the sub-array dimensions beyond a certain limit will result in a main beam that is too narrow for enabling the needed array beam scanning (see [11] for the correlation between the array size and main beam). Another upper bound follows from the observation that the sub-array dimensions determine the minimum inter-element spacing and may also influence the maximum inter-element spacing, the values of this spacing yielding the spatial extent of the region where high lobes, corresponding to GL in the case of uniform lattices, will appear.

The 4 chosen sub-array configurations and their radiation pattern behaviour are hereafter presented in detail.

Sub-array A

The first case concerns a configuration composed of only one tile (see Fig. 5.12). The small panel has been used to measure the radiation pattern in the anechoic chamber because of its more convenient dimensions and for allowing the possibility of a perfect alignment between the transmitting horn and the receiving tile. The measured pattern, shown in Fig. 5.13 validates the expected symmetry along $\phi = 0°$ and $\phi = 90°$, as easily noticeable from the contour plot. The main beam, covering the FOV, is quite large and flat in the region of interest guaranteeing an almost constant directivity for the complete area in the FOV. However, this value is quite reduced, reaching at boresight a maximum of 19.6 dB.

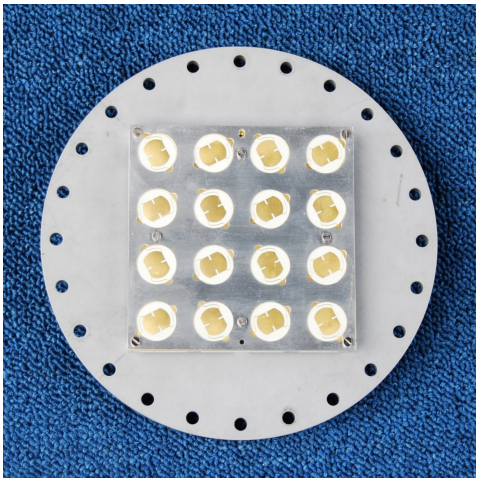

Figure 5.12: Sub-array configuration A

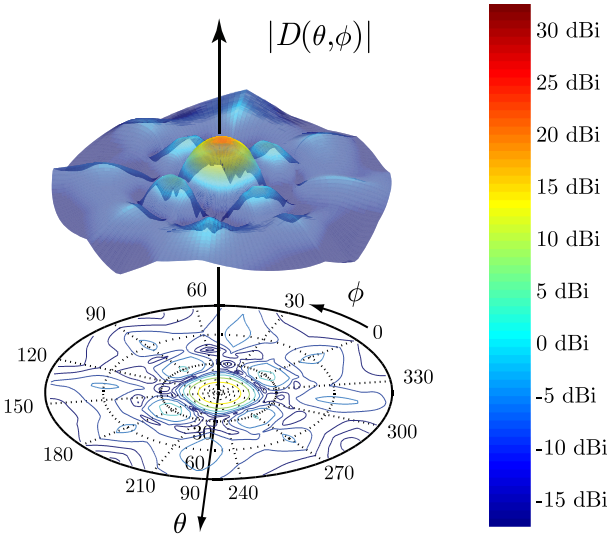

Figure 5.13: Three-dimensional view and contour plot of the directivity of sub-array A.

Sub-array B

The second case concerns a configuration composed of two tiles (see Fig. 5.14). The large panel has been used to measure the radiation pattern in the anechoic chamber as this configuration could not be accommodated on the small panel.

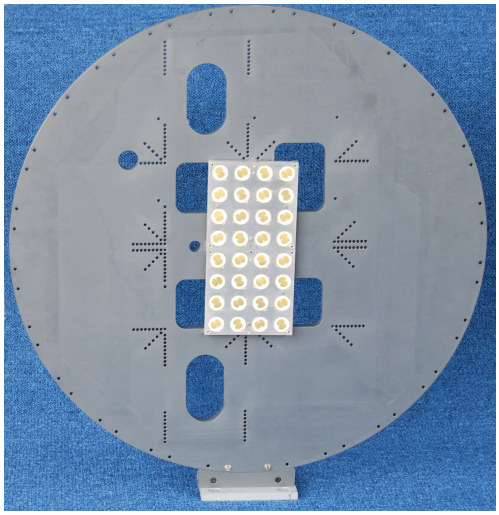

Figure 5.14: Sub-array configuration B

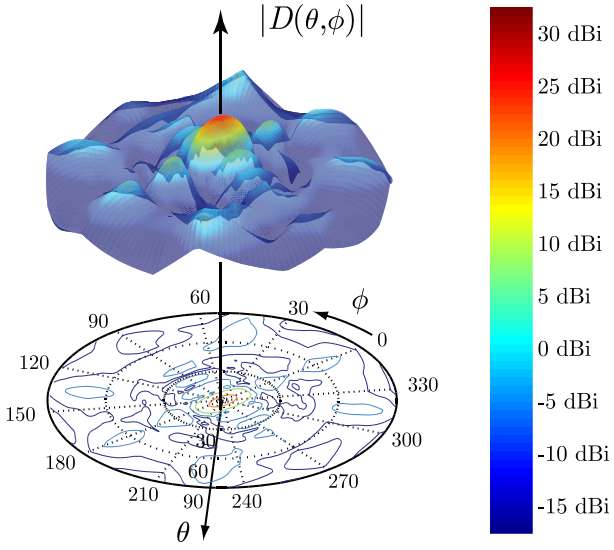

Figure 5.15: Three-dimensional view and contour plot of the directivity of sub-array B.

The measured pattern shown in Fig. 5.15 evidences a main beam enlonged along $\phi = 0°$, a natural consequence of the configuration's dimensions, since the vertical side is twice the horizontal one. In this case, the maximum directivity improves, when compared to the configuration with one tile only, by about 3 dB, reaching a maximum value of about 22.6 dB at boresight.

Sub-array C

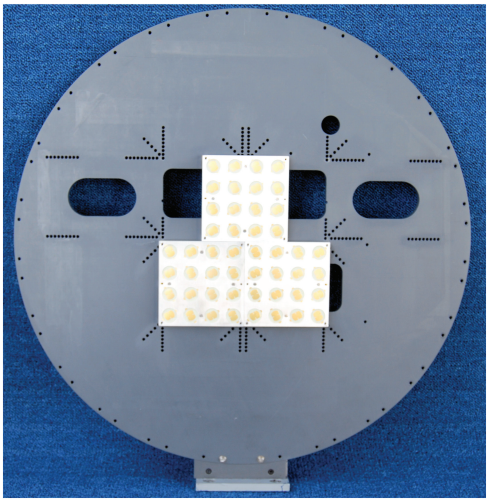

Figure 5.16: Sub-array configuration C

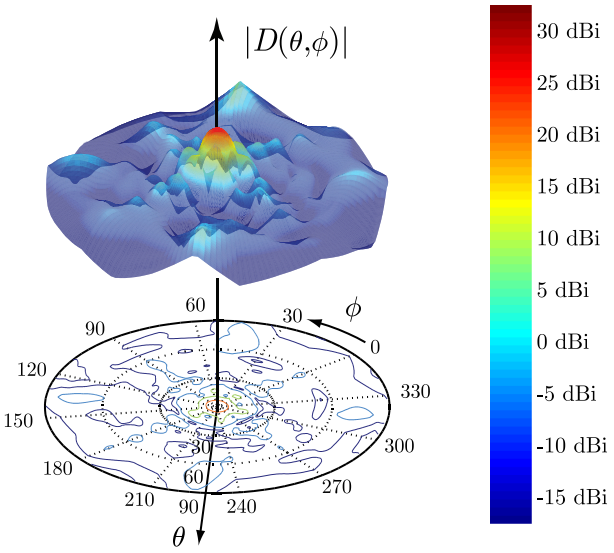

Figure 5.17: Three-dimensional view and contour plot of the directivity of sub-array C.

The third case concerns a configuration composed of three tiles (see Fig. 5.16). The large panel has been used to measure the radiation pattern in the anechoic chamber and, due to the sub-array not being symmetric, the measuring column position has been adjusted for each ϕ cut measurement

in order to minimize the allignement error. The measured pattern shown in Fig. 5.17 demonstrates a more circular main beam when compared with the previous case. The maximum directivity reaches in this case a maximum value of about 24.5 dB.

Sub-array D

The last presented case concerns a configuration composed of four tiles (see Fig. 5.18). The large panel has been used to measure the radiation pattern in the anechoic chamber because of the large dimensions of the configuration. No disalignement error was introduced in this case since the sub-array centre coincided with the panel's centre.

The measured pattern in Fig. 5.19 shows a quite rotationally symmetric main beam when compared with sub-arrays B and C. The maximum directivity is strongly increased, reaching a maximum value of about 25.5 dB at boresight. Nevertheless, due to the sub-array dimensions, the directivity abruptly drops around 5°.

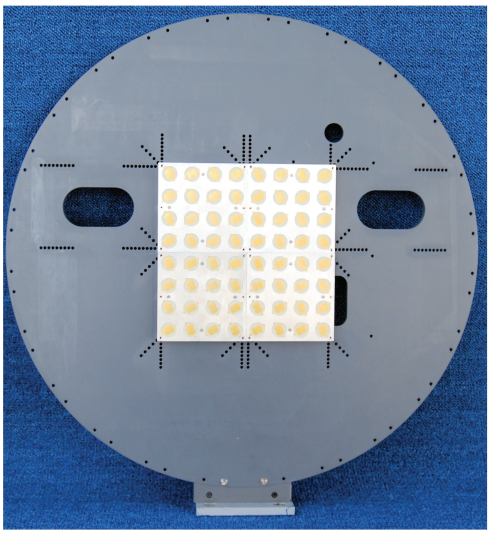

Figure 5.18: Sub-array configuration D

As anticipated at the beginning of this section, the advantages of each sub-array configuration become clear considering Fig. 5.20. When the antenna beam has to be scanned over the desired coverage it is important to choose carefully the sub-arrays to be employed in the array antenna, basing the choice not only on the value of the maximum directivity but also on that of the directivity at the end of coverage. In order to stress the latter

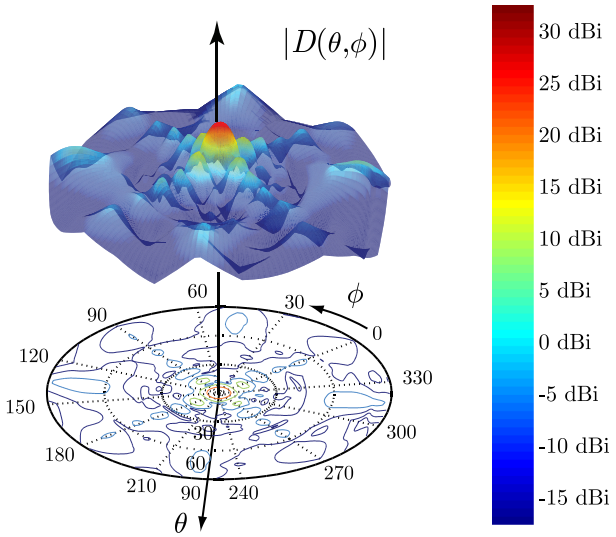

Figure 5.19: Three-dimensional view and contour plot of the directivity of sub-array D.

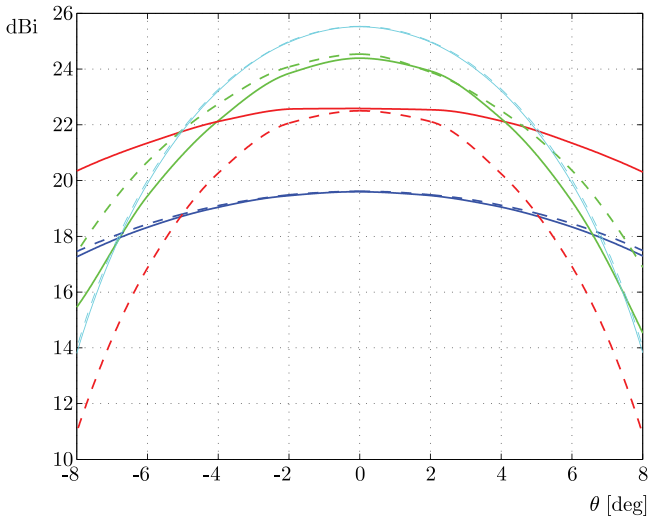

Figure 5.20: Pattern comparison between the several sub-array presented. Blue lines – one tile sub-array, red lines – two tiles sub-array, green lines – three tiles sub-array, cyan lines – four tiles sub-array. Continuous line – $\phi = 0°$, dotted line – $\phi = 90°$.

observation, with reference to the pattern multiplication scheme quantified in Eq. (2.17), the array factor is multiplied by the radiation intensity at each direction. In the case of large sub-arrays, the rapid fall off of the correspond-

ing radiation patterns in Fig. 5.19 will yield a similarly reduced maximum directivity when the beam is scanned towards the end of the coverage. It is essential to avoid the use of sub-arrays characterized by a large directivity variation over the complete FOV, the more so when, as in the case under study, there are stringent SLL requirements to be satisfied.

After these considerations, it can be concluded that sub-arrays of type D are, due to their dimensions, not suited for the application addressed in this work. The difference between the maximum directivity and the one at the FOV border shown in Fig. 5.20 is considerable. For this reason, only the sub-arrays A, B and C will be employed in the final configuration presented hereafter.

5.3 Sunflower final results

The most promising array configurations developed by means of the robust Sunflower placement strategy described in Paragraph 4.4.4 were combined with the sub-arrays studied in the previous sections for yielding a high performance (virtual) *Sunflower array demonstrator* that properly addresses the stringent requirements enumerated in Appendix A. In order to minimize costs, while demonstrating full functionality, the measured sub-array radiation patterns were used, as anticipated, in an off-line pattern multiplication scheme [2] for evaluating the radiation pattern and scanning capabilities of an array having the sub-arrays placed according to the Sunflower algorithm. Since the minimum distance between the sub-arrays in the considered configuration is about $3\,\lambda$, resulting in a reduced sub-array mutual coupling, the total array pattern computed as the superposition of the sub-array patterns was considered a good approximation of the real array pattern.

This analysis now proceeds by describing the specific choices made for assembling the demonstrator.

5.3.1 Design choices

Several possible new configurations, taking into account the particular characteristics of the manufactured sub-arrays, have been studied. Among them, one has been selected as a good compromise between a reduced number of active chains and performance, and it is hereafter discussed in detail.

The configuration of choice comprises sub-arrays of types A, B and C, only (see Fig. 5.21). By using the three types of sub-arrays shown in Fig. 5.21 it has been possible to better exploit the available antenna aperture with a

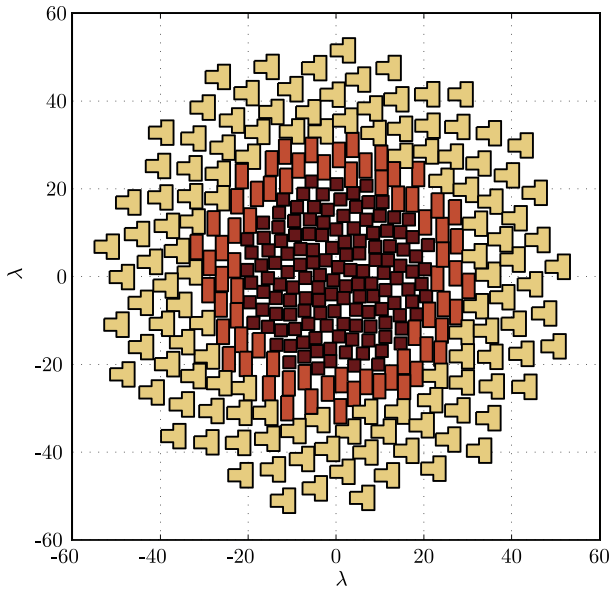

Figure 5.21: The proposed Sunflower array demonstrator. The three types of sub-arrays receive equal power

reduced number of active chains, and, at the same time, keep the complexity of the configuration low by using the same basic tile for assembling the three types of sub-arrays. The circular aperture of radius $R_{ap} = 53\,\lambda$ has been filled with 138 radiators of type A, 69 of type B and 125 of type C, for a total number of active chains equal to 332. The positions of these sub-arrays have been found, as already mentioned, with the *sunflower law* presented in Paragraph 4.3.3, considering a Taylor reference amplitude taper with SLL=30 dB and $\bar{n} = 3$ (see Appendix E).

5.3.2 Demonstrator performances

In order to check the chosen configuration performances against the specified requirements (see Appendix A), the radiation pattern was computed for the beam pointing at boresight and at Europe's edges.

The results achieved with the presented configuration are shown in Figs. 5.22 and 5.23. In the first one it is possible to appreciate how the taper applied to the sub-array positions can shape the pattern, reducing in a significant way the SLL in the desired field of view.

Two ϕ cuts have been plotted in Fig. 5.22 for the beam pointing at boresight, namely for $\phi = 0°$ and ϕ=90°. The radiation pattern result-

ing from the sunflower configuration can be considered almost rotationally symmetric over Europe ($\theta \in [-4°, 4°]$).

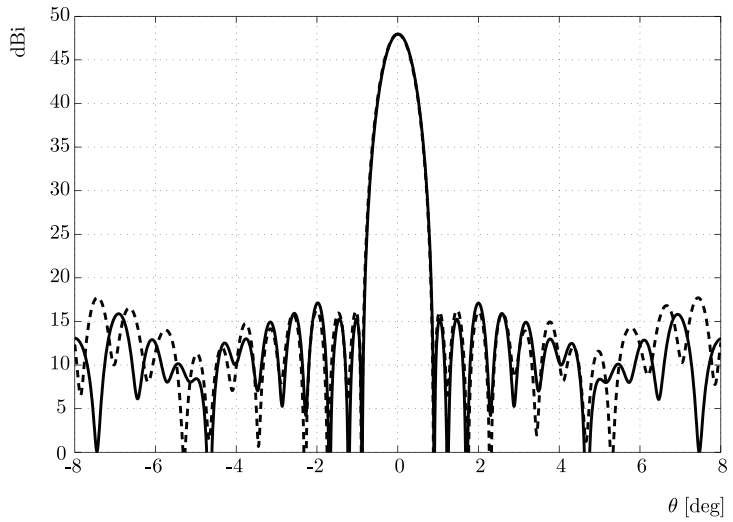

Figure 5.22: Radiation pattern at boresight for the achieved configuration in two ϕ cuts, $\phi = 0°$ – continuous line and $\phi = 90°$ – dotted line.

Figure 5.23 represents the array radiation pattern when the beam is pointing at Europe's edge. Thanks to the colour choice, with a threshold at the 20 dBi level, it is possible to notice that the SLL is not exceeding the requested level but remains under 19 dBi. In both cases, when the beam is pointing at boresight and when it points at the edges of Europe, the results achieved are satisfying the demanding requirements given in Table A.1.

In order to appreciate the advantages in terms of GL avoidance and reduction of the number of controls arising from the use of non-uniform arrays, a comparison between the proposed configuration and two classical array solutions (case 1 and case 2) is hereafter presented.

Comparison with uniform array case 1

In the first case the simple square tile (sub-array A in Paragraph 5.2.2) has been chosen as a radiator for the uniform configuration. An inter-element spacing equal to 3.3 λ was set in order to ensure an almost complete filling of the available aperture and, at the same time, a perfect fitting of the tiles in a triangular lattice (see Fig. 5.24). With this choice, using a 53 λ radius aperture as in the *sunflower array* case, 931 sub-arrays are employed. The GL, for the considered configuration, occur outside the desired FOV

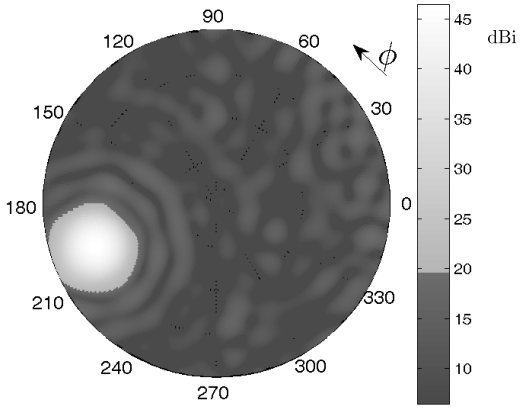

Figure 5.23: Pattern for the discussed array configuration when the beam is pointing at the Europe's edge.

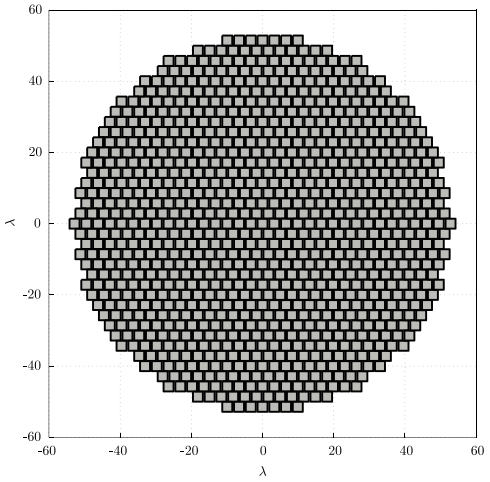

Figure 5.24: Position of the tiles in the reference array case 1.

(see Eqs. (2.26) and (2.27)). The same Taylor amplitude taper used as a reference for the non-uniform array design has been applied in the uniform array.

The patterns corresponding to the uniform and non-uniform arrays are shown in Fig. 5.25 All ϕ cut plots were superimposed for providing an indication of the overall array performances. It is interesting to notice that, while the two pattern behaviours are remarkably similar within the FOV,

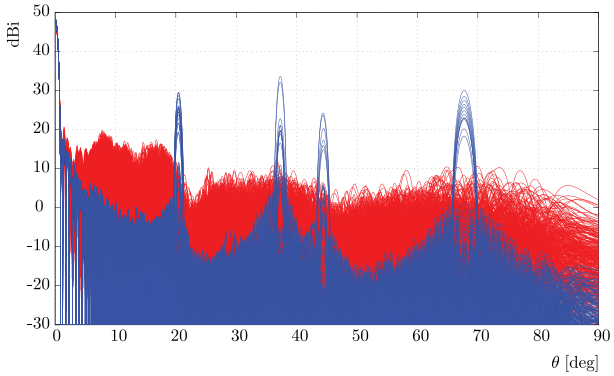

Figure 5.25: Directivity pattern for all the ϕ cuts for the beam pointing at boresight. Red – sunflower array; blue – uniform array case 1.

outside the Earth the pattern of the uniform array decreases until the GL appears around $\theta = 20°$ and the non-uniform array pattern rises with higher SLL with respect to the uniform configuration but without any GL. This becomes even clearer in Fig. 5.26, where the directivity patterns of the two arrays are plotted for the beam pointed at the Europe's edges.

The requirements and the results achieved with the amplitude-taper, uniform triangular lattice and with the proposed non-uniform array configuration are summarized in Table 5.1. It is evident how, by employing a non-uniform configuration, it is possible to obtain comparable or even better performance when compared to the uniform lattice case.

For example, it can be noted in Table 5.1 that while the non-uniform

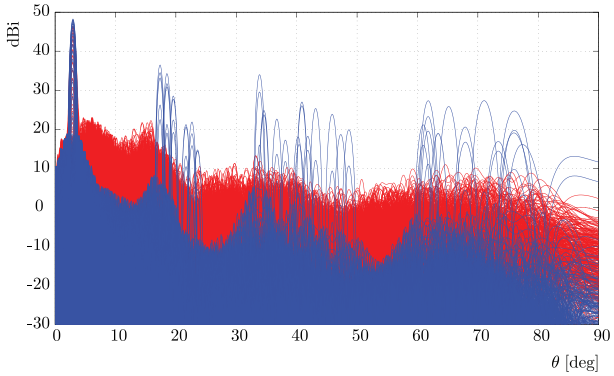

Figure 5.26: Directivity pattern for all the ϕ cuts for the beam pointing at Europe edges. Red – sunflower array; blue – uniform array case 1.

Table 5.1: Mission requirements and achieved results

	Required	Sparse	Periodic
SLL over Europe	<20 dBi	20.65 dBi	18.85 dBi
SLL over Earth	< 25 dBi	22.7 dBi	18.85 dBi
SLL over visible space	<30 dBi	22.7 dBi	**36.47 dBi**
EOC directivity	43.8 dBi	43.73 dBi	45.05 dBi
Number of sub-arrays		332	931

configuration is able to satisfy the stringent requirements over the complete visible space, the uniform array can not prevent the arising of grating lobes. These GL, even though reduced by the element factor, are still visible (see Fig. 5.26) and their values rendered this configuration not able to satisfy the imposed SLL specifications over the complete visible space. Moreover, with the proposed configuration it is possible to drastically reduce the number of active chains employed, resulting in a lighter and less expensive configuration.

Comparison with uniform array case 2

This procedure would result in a loss of directivity and has been discarded. A meaningful comparison would consist in using larger inter sub-array spacings and larger sub-arrays.

Unfortunately, the available, measured sub-arrays were not suited for

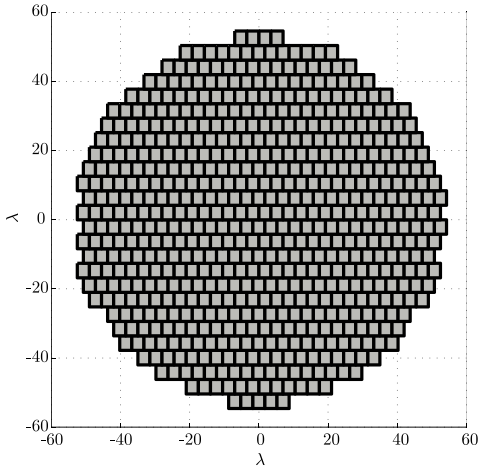

Figure 5.27: Position of the tiles in the reference array case 2.

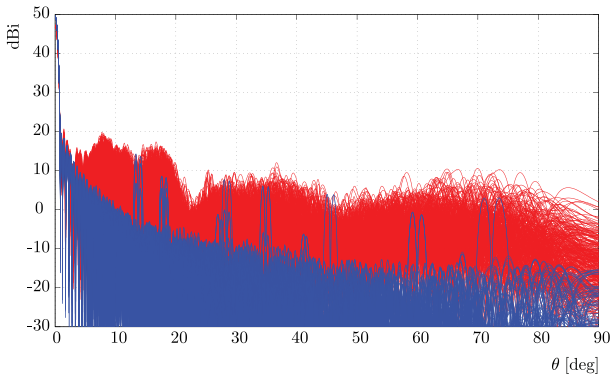

Figure 5.28: Directivity pattern for all the ϕ cuts for the beam pointing at boresight. Red – sunflower array; blue – uniform array case 2.

the comparison, being or too small (sub-array A) or too large (sub-array D). For the sake of completeness a new sub-array, composed of 30 elementary patches (similar to the basic ones described in Appendix F), arranged in 6 rows and 5 columns on a rectangular lattice, has been simulated with MATLAB. In this case no inter-element coupling and losses were taken into account and the radiated field is simply the superposition of the 30 elementary patch fields. Figure 5.27 shows how the new sub-arrays have been arranged on a triangular lattice, completely filling the $53\,\lambda$ radius available aperture. As expected, by increasing the sub-array distance GL arise closer to the main beam, when compared to the previous reference case (see Figs. 5.28 and 5.29). In this case, since the aperture is fully populated, it is possible to note an increment in the directivity, and, since larger sub-arrays have

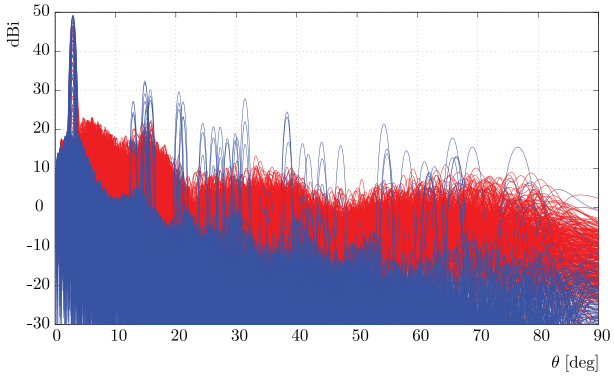

Figure 5.29: Directivity pattern for all the ϕ cuts for the beam pointing at Europe edges. Red – sunflower array; blue – uniform array case 2.

Table 5.2: Mission Requirements and Achieved Results

	Required	Sparse	Periodic
SLL over Europe	<20 dBi	20.65 dBi	19.6 dBi
SLL over Earth	< 25 dBi	22.7 dBi	119.6 dBi
SLL over visible space	<30 dBi	22.7 dBi	**32.5 dBi**
EOC directivity	43.8 dBi	43.73 dBi	45.8 dBi
Number of sub-arrays		332	601

been used, a reduction of the number of needed controls (see Table 5.2). At this point, with the inter-element spacing being dictated by the need to keep GL outside the FOV, no other possibility to further reduce the number of controls for the given aperture exists.

5.3.3 Concluding considerations

In this chapter the innovative *'sunflower' positioning algorithm* was validated by means of a combination of measurements and off-line processing. In this way it was possible to simulate the very large array needed for the application defined in Appendix A. Four sub-arrays composed of 1, 2, 3 or 4 basic modules (whose design was taken over from TAS) were assembled and measured. These results were then post-processed for simulating the large array, designed with a sunflower law. The synthesized array performance has been evaluated for several beam pointing positions, thus demonstrating the suitability of the proposed array configuration for the mission that is aimed at. Finally the performances of such an array have been compared with a reference uniformly spaced array configuration and the advantage of using the *sunflower* array are enlightened.

Several major considerations can be summarized from this chapter:

- The reduction of the needed active chains achievable by employing non-uniformly spaced arrays has been demonstrated.
- The feasibility of the *sunflower* array implementation with (off the shelf) sub-arrays has been proved.
- The possibility of a complete avoiding of the occurrence of GL with the proposed configuration has been confirmed.

Chapter 6

Conclusions

6.1 General conclusions and major result

In the field of satellite communication saving space on board, reducing costs and improving antenna performances are difficult tasks lately becoming of great importance. For this reason realizing a non-uniform direct radiating array (DRA) able to satisfy stringent requirements with a reduced number of active chains, all employing amplifiers working at the same point, has been considered by the author a challenging task to be addressed in this PhD work.

The aim of this investigation was to identify several array configurations characterized by a reduced complexity and cost with respect to conventional arrays or to reflector configurations. Moreover these arrays must satisfy stringent requirements of a communication mission from GEOstationary satellite, such as the ones catalogued in Appendix A. In particular, the work focused on transmit, planar, DRA with non-uniform element placement and a reduced number of controls. In order to limit the price and to diminish the losses on board of the satellite, the design minimized the number of amplifiers. Moreover all amplifiers driving the non-uniform configuration were taken to be identical and to operate at the same, optimised operational point. In this way, the system efficiency can be maximized, when compared to the case in which an amplitude taperis applied, by reducing the wasted power that would be transformed into heat and create additional problems related to the heat dissipation.

This dissertation started with the discussion of the pattern characteristics of uniform array. Since with a regularly spaced array it is impossible to shape the pattern without making use of amplitude taper, non-uniform

arrays have been introduced and their pattern behaviour discussed at length. Non-uniform arrays were proven to be able to shape the pattern according to imposed requirements and, at the same time, avoid the occurrence of GL. Several innovative techniques to design this particular class of arrays were proposed and compared.

Among them the *sunflower* positioning technique was chosen as the best one to deterministically design non-uniform planar arrays with really low SLL and a good rotational symmetry of the radiation pattern. This simple technique is based on the application of two separate laws for finding the radial and angular element positions. The first one comes directly from the relation established in the thesis between the amplitude taper and the density taper. Regarding the angular positioning law, the concept of optimal angular spreading, inherited from the natural world, has been applied to the sunflower array antenna in order to guarantee the sparsity of the element positions both in the radial and angular coordinates. This innovative technique was proven able to succesfully replicate all the amplitude taper laws considered in Chapter 4.

Then the *sunflower* synthesis technique has been generalized for employing in the same array differently sized sub-arrays. The two options of having equal amplitude feeding or equal power feeding for the different radiators were considered. In the first case the planar aperture was divided by means of a Voronoi tessellation associated with the sunflower positioning law and the cells were filled with the best fitting sub-arrays. For this purpose several sub-array kinds and shapes were considered, from the best fitting circular apertures to a limited number of more technologically easy to be implemented shapes. In the second case, the sub-array shape and kind can influence the positioning. This second approach was chosen for its easier technological implementation and used to design a large planar array able to satisfy the satellite mission requirements (see Appendix A). In order to physically validate the positioning principle of the *sunflower* array antenna, a demonstrator at a scaled frequency was manufactured and measured. More in detail, 4 different sub-arrays were assembled and their radiation patterns were superimposed in order to compute the total array radiated pattern. The measured and simulated results are in good agreement and have demonstrated the effectiveness of the approach. The final results confirmed the possibility to achieve with the *sunflower array antenna* a strong reduction of the number of controls while satyisfing the stringent requirement in Appendix A and completely avoiding the GL occurence.

6.2 Novelty aspects

- *Sunflower antenna*: a new array antenna configuration with excellent pattern behaviour, recognized as a household name in the international antenna engineering community. This antenna results to be more versatile than others in the literature [4] as it renders possible the control of the SLL.

- *Reduced number of controls*: When compared to a classic array antenna with similar pattern behavior, the sunflower array antenna makes use of a strongly reduced number of controls. In the examples considered in Chapter 5, the number of active chains employed was 50% and 30% of the ones of two uniform reference arrays.

- *Taper function*: The beam shaping that up to now was mainly achieved only by imposing an amplitude taper on the array excitations, has been replicated by resorting to other array parameters. It has been proved that element positions, amplitudes, phases and type of elements can equally contribute to the beam shaping.

- *A truly non-uniform array*: The sunflower analytical technique for designing an array with completely non-regular element locations has been successfully developed and validated both numerically and by physical experiments. The spacing between the elements has been proved to be truly non-uniform differentiating this technique from the array thinning techniques.

- *Simple one dimensional law to mimic an amplitude taper*: The particular placement of the elements in a planar array has been provided according to two simple independent equations, one for the distances of the elements from the centre and one for their location angles. In this work, it has been proved possible to obtain in an analytical way the positions of the elements in an array antenna that is able to satisfy stringent requirements by mimicking a reference amplitude taper.

- *Possibility to rigorously take into account differently sized radiators*: The chosen synthesis technique has been generalized in order to take into account the case of employing in the same array differently sized sub-arrays, all fed with the same input power. In this way, a better use of the available antenna aperture has been achieved and a reduction of the number of active chains has been obtained.

- *Synthesis techniques*: Several other analytical (Null-matching, Perturbative, Auxiliary Array Factor) and non-analytical (GA) techniques

for the non-uniform antenna array synthesis have been developed (see Chapter 3 and Appendix C) and have been proved able to successfully solve some particular satellite communication problems.

- *Hybrid synthesis technique*: the new AAF analytical technique (elaborated upon in Appendix C) has been demonstrated to be able to combine in a rigorous way amplitude, phase and space tapers in order to replicate patterns with particularly stringent constraints even by accounting for minimum inter-element spacing.

- *Natural laws*: The concept of optimal angular spreading was taken from the natural world and applied to the sunflower array antenna in order to guarantee the sparsity of the element positions in the angular coordinates. This resulted in an array whose pattern is able to satisfy the requirements in all the ϕ cuts.

- *Feasibility*: The sub-arrays for the real demonstrator have been implemented, certifying the feasibility of a 'low cost' non-uniform array realized with (mainly) 'off-the-shelf' technology. The behaviour of the proposed sub-arrays has been simulated and measured (Chapter 5).

- *Array formulas*: A collection of formulas relating the array element positions and excitations with the array radiation pattern characteristics, has been created and some new representations of the pattern relevant to the uniformly spaced array were added(see Chapters 2, 4, Appendix B).

6.3 Future work

The innovative work proposed in this dissertation created the basis for several interesting extensions and opened the way to the possible application of the *sunflower* array antenna in different areas.

An algorithm to check and avoid overlap between the sub-arrays has been successfully finalized. This takes into account the cases of employing sub-arrays of square or hexagonal shape and could be eventually extended in order to consider more sub-array shapes. In this way the complete algorithm sequence could be rendered automatic.

Sub-array shapes other than the ones considered in this dissertation could be considered in order to ensure a better fitting in the Voronoi cells. For example, instead of starting from grouping the tiles, the sub-arrays could be created starting from single patches. From an industrial point of view,

such an approach could result in a sizeable reduction of the number of active chains and in the avoidance of sub-array overlapping.

The Auxiliary Array Function (AAF) technique has been proved really efficient for the design of linear arrays where it is important to replicate a specified pattern. A possible future extension to the planar case could be considered in order to apply the technique to a wider class of problems.

The developed *sunflower* positioning law could be employed in areas other than satellite communication, as for example for radar surveillance applications.

Bibliography

[1] P. Atela, C. Gole, S. Hotton, "A Dynamical System for Plant Pattern Formation: Rigorous Analysis," in *Journal of Nonlinear Science*, vol. 12, Is. 6, pp. 641–676, Oct., 2002.

[2] C. A. Balanis, Antenna Theory: Analysis and Design, 3rd ed., New York: John Wiley & Sons Inc., 2005.

[3] M. G. Bray, D. H. Werner, D. W. Boeringer, D. W. Machuga, "Optimization of thinned aperiodic linear phased arrays using genetic algorithms to reduce grating lobes during scanning," in *IEEE Trans. Antennas Propag.*, vol. 50, Is. 12, pp. 1732–1742, Dec. 2002.

[4] D. W. Boeringer, "Phased array including a logarithmic spiral lattice of uniformly spaced radiating and receiving elements," *U.S. Patent No. 6433745 B1*, Silver Spring, MD, US, 13 Apr. 2002.

[5] G. Caille, Y. Cailloce, C. Guiraud, D. Auroux, T. Touya, M. Masmousdi, "Large Multibeam Array Antennas with Reduced Number of Active Chains," in *EuCAP 2007*, pp. 1–7, Edinburgh,11–16 Nov.2007.

[6] Y. Cailloce, G. Caille, I. Albert, J.M. Lopez, "A Ka-band direct radiating array providing multiple beams for a satellite multimedia mission," in *IEEE Proc. Phased Array Sys. and Tech., 2000*, pp. 403–406, 21-25 May 2000.

[7] S. I. K. Castiglioni, G. Toso, C. Mangenot, "Multi-beam antenna based on a single aperture using overlapped feeds," in *JINA 2004*, Nice, Nov. 2004.

[8] H. Chane, M. Frossard, R. Barbaste, P. Bosshard, T. Girard, P. Lepeltier, I. Albert, J. Sombrin, C. Mangenot, "Recent developments in feed array for Ka-band FAFR antenna," in *EuCAP 2006*, Nice, 6–10 Nov. 2006.

[9] R. Chantalat, P. Dumon, B. Jecko, M. Thevenot, T. Monediere, "Interlaced feeds design for a multibeam reflector antenna using a 1-D dielectric PBG resonator," in *IEEE AP-S2003*, The Ohio State University Columbus, Ohio, 22-27 June 2003.

[10] K. Chen, X. Yun, Z. He, and C. Han, "Synthesis of sparse planar arrays using modified real genetic algorithm," in *IEEE Trans on Antennas and Propagation*, vol. 55, pp. 1067–1073, Apr. 2007.

[11] C. I. Coman, I. E. Lager, and L. P. Ligthart, "Design considerations in sparse array antennas," in *Proc. 3^{rd} European Radar Conference – EuRAD*, pp. 72–75, Manchester, UK, Sep. 2006.

[12] H. S. M. Coxeter, *Regular polytopes*, 3rd ed. New York: Dover Publications, Inc., 1973.

[13] D. J. Daniels, *Ground penetrating radar*, 2nd ed. The Institution of Engineering and Technology, London, 2004.

[14] C. L. Dolph, "A current distribution for broadside arrays which optimizes the relationship between beamwidth and sidelobe level," in *Proc. of the IRE*, vol. 34, No. 6, pp. 335–348, Jun. 1946.

[15] R. A. Dunlap, *The Golden Ratio and Fibonacci Numbers*, Singapore: World Scientific Publishing Co., Pte., Ltd., 1997.

[16] R. S. Elliott, "The Theory of Antenna Arrays, Ch. 1, Vol. 2 in Microwave Scanning Antennas, R. C. Hansen, (ed.), New York: Academic Press, 1966, p. 44–45.

[17] R. S. Elliott, *Antenna theory and design*, Englewood Cliffs, Prentice-Hall, 1981.

[18] J.O. Erstad, S. Holm, "An Approach to Design of Sparse Array Systems," in *Proc. 1994 IEE Symp. Ultrasonic*, Cannes, France.

[19] L. J. Fogel, A. J. Owens, M. J. Walsh, *Artificial Intelligence through Simulated Evolution*, Wiley, New York, 1966.

[20] D. E. Golberg, *Genetic Algorithms in Search, Optimization and Machine Learning*, Addison-Wesley, Reading, 1989.

[21] P. W. Hannan, " The element-gain paradox for a phased array antenna," *IEEE Trans. Antennas Propag.*, vol. 12, Is. 4, pp. 423–433.

[22] R. C. Hansen, *Phased Array Antennas*, New York: John Wiley and Sons, Inc., 1998.

[23] R. Harrington, "Sidelobe reduction by nonuniform element spacing," *IEEE Trans. Antennas Propag.*, vol.9, pp. 187–192, Mar. 1961.

[24] R. L. Haupt, "Unit circle representation of aperiodic arrays," *IEEE Trans. Antennas Propag.*, vol. 43, pp. 1152–1155, Oct. 1995.

[25] R.L. Haupt, "Thinned Arrays Using Genetic Algorithms," in *IEEE Trans. Antennas Propagat.*, vol. 41, no. 2, Feb. 1993, pp. 993–999.

[26] R.L. Haupt, J.J. Menozzi, C.J McCormack, "Thinned arrays using genetic algorithms," in *AP-Symposium 1993*, vol. II, pp. 712–715, Jun 28-Jul.2 1993 .

[27] F. Hodjat, S. Hovanessian, "Nonuniformly spaced linear and planar array antennas for sidelobe reduction," in *IEEE Trans. Antennas Propag.*, vol. 26, pp. 198–204, Mar. 1978.

[28] J. Holland, *Adaptation in Natural and Artificial Systems*, Michigan Press, 1975.

[29] J. O. Erstad, S. Holm, "An approach to the design of sparse array system," in *IEEE Proc. Ultrasonics Symp. 1994*, vol. 3, pp. 1507–1510, 4 Nov. 1994.

[30] A. Ishimaru, "Theory of Unequally-Spaced Arrays," in *IEEE Trans. Antennas Propag.*, vol. 10, Is. 6, pp. 691–702, Nov. 1962.

[31] A. Ishimaru, Y. S. Chen, "Thinning and broadbanding antenna arrays by unequal spacings," in *IEEE Trans. Antennas Propag.*, vol. 13, pp. 34–42, Jan. 1965.

[32] T. Ismail, M. Dawoud, "Null steering in phased arrays by controlling the element positions," in *IEEE Trans. Antennas Propagat.*, vol. Ap-39, pp. 1561–1566, Nov. 1991.

[33] M. V. Ivashina, M. N. Kehn, P. Kildal, R. Maaskant, "Decoupling efficiency of a wideband vivaldi focal plane array feeding a reflector antenna," in *IEEE Trans. Antennas Propag.*, vol. 57, Is. 2, pp. 373–382.

[34] H. Schjaer-Jacobsen, K. Madsen "Synthesis of Nonunifonnly Spaced Arrays Using a General Nonlinear Minimax Optimization Method," in *IEEE Trans. Antennas Propag.*, vol. 24, Is. 4, pp. 501–506, Jul. 1976.

[35] E. Jahnke, F. Emde, F. Losch, *Tables of Higher Functions*, McGraw-Hill Book Company, Inc., New York, N. Y., p. 251, 1960.

[36] A. J. Jerri, "The Shannon sampling theorem-Its various extensions and applications: A tutorial review," in *Proc. IEEE*, vol. 65, n. 11, pp. 1565–1596, Nov. 1977.

[37] G. P. Junker, S. S. Kuo, C. H. Chen "Genetic Algorithm Optimization of Antenna Arrays with Variable Interelement Spacings," in *IEEE Trans. Antennas Propag.*, vol. 24, Is. 4, pp. 501–506, Jul. 1976.

[38] W. K. Kahn, "Element efficiency: a unifying concept for array antennas," in *IEEE Antennas Propag. Magazine*, vol. 49, n. 4, pp. 48–56, Aug. 2007.

[39] M. N. Kehn, M. V. Ivashina, P. Kildal, R. Maaskant, "Definition of unifying decoupling efficiency of different array antennas: Case study of dense focal plane array feed for parabolic reflector," in *Int. J. Electron. Commun. (AEU)*, 2009, 10.1016/j.aeue. 2009.02.011.

[40] J. Kennedy, R. Eberhart, "Particle swarm optimization", in *IEEE conf. Neural Networks 1995*, vol. 4, pp. 1942–1948, Dec. 1995.

[41] B. P. Kumar, G. R. Branner "Design of Unequally Spaced Arrays for Performance Improvement," *IEEE Trans. Antennas Propag.*, vol. 47, Is. 3, pp. 511–523, Mar. 1999.

[42] S. S. Kuo, G. P. Junker, T. K. Wu, C. H. Chen "A density taper technique for low side lobe applications of hex array antennas," in *IEEE Proc. Phased Array Sys. and Tech., 2000*, pp. 493–496, 21-25 May 2000.

[43] V. K. Lakshmeesha, V. V. Srinivasan, V. Venkatesh, S. Pal, "C-Band Microstrip Planar Array for Spaceborne Microwave Remote Sensing," in *21st EUMA conference 1991*, pp. 763–768, 9–12 Sep. 1991.

[44] A. Lasserre, P. Lepeltier, C. Mangenot, M. Dejus, "Antennes bord pour application multimedia en bande Ka," in *JINA 2004: 13th international symposium on antennas*, 8–10 No. 2004.

[45] L. P. Ligthart, "A New Numerical Approach to Planar Phased Arrays,", in *5th EuMC*, Hamburg, Germany, 1975.

[46] Y. Lo, "A spacing weighted antenna array," in *IRE Int. Convention Record*, vol. 10, Part 1, pp. 191–195, March 1962.

[47] Y. T. Lo, S. W. Lee "A study of space-tapered arrays," *IEEE Trans. Antennas Propag.* vol. 14, Is.1, pp. 22–30, Jan. 1966.

[48] N. Llombart, A. Neto, G. Gerini, M. Bonnedal, P. De Maagt, "Impact of Mutual Coupling in Leaky Wave Enhanced Imaging Arrays," in *IEEE Trans. Antennas Propag*, vol. 56, No. 4, April 2008.

[49] N. Llombart, A. Neto, G. Gerini, M. Bonnedal, P. De Maagt, "Leaky wave enhanced feeds arrays for the Improvement of the Edge of Coverage Gain in Multi beam Antennas," in *IEEE Trans. Antennas Propag*, vol. 56, No. 5, May 2008.

[50] R. J. Mailloux, *Electronically Scanned Array*, Morgan and Claypool Pub., 2007.

[51] R. J. Mailloux, *Phased Array Antenna Handbook*, Artech House, Boston, 2005.

[52] R. J. Mailloux, "On the use of metallized cavities in printed slot arrays with dielectric substrates," in *IEEE Trans. Antennas and Propagat.*, vol. AP-35, n. 5, May 1987, pp. 477-487.

[53] R. J. Mailloux, S. G. Santarelli, T. M. Roberts, D. Luu, "Irregular Polyomino-Shaped Subarrays for Space-Based Active Arrays,' in *International Journal of Antenna and Propagat.*, vol. 2009, ID 956524, doi:10.1155/2009/956524.

[54] A. L. Maffett, "Array factors with nonuniform spacing parameter," *IRE Trans. Antennas Propag.*, vol. 10, pp. 131–136, Mar. 1962.

[55] C. Mangenot, P. Lepeltier, J.L. Cazaux, J. Maurel, "Ka-band fed array focal reflector receive antenna design and development using MEMS switches," JINA Conference 2002, Vol. II, pp. 337–345, Nov. 12–14 2002.

[56] C. Mangenot, G. Toso, M.C. Viganó, A.G. Roederer, "Non-periodic Direct Radiating Arrays for Multiple Beam Space Telecommunication Missions," in *IEEE Antennas Propagat. Symp.* pp. 3149–3152 San Diego, CA, USA, Jul.7-11 2008.

[57] J. C. Maxwell, *Treatise on Electricity and Magnetism*, vol 1 and 2, 3rd ed., Oxford, 1904.

[58] T. A. Milligan, *MODERN ANTENNA DESIGN*, 2nd ed., John Wiley and Sons Inc. Pub, New Jersey, 2005.

[59] Jr. H. P. Muhs, C. K. Watson, "Slot antenna with face mounted baffle," *U.S. Patent No. 4499474*, February 12, 1985.

[60] A. Okabe, B. Boots, K. Sugihara, S. N. Chiu, *Spatial Tessellations*, 2nd ed., Chichester: John Willey and Sons Ltd, 1999.

[61] D. M. Pozar, *Microwave engineering*, 3rd ed., John Willey and Sons Ltd, 2005.

[62] J. Robinson, Y. Rahmat-Samii, "Particle swarm optimization in Electromagnetics," in *IEEE Trans. Antennas Propag.*, vol. 52, n. 2, Feb. 2004.

[63] G. Ruggerini, G. Toso, P. Angeletti, "An Innovative Multibeam Antenna based on an Active Aperiodic Lens," in *EuCAP 2010*, Barcelona, Apr. 12–16 2010.

[64] P. Sattari, N. Hejazi, "Array pattern null steering using genetic algorithm by element position perturbations," in *Conf. Electrical and Computer Engineering, CCECE*, pp. 423–428, 2008.

[65] H. Schantz, *The art and science of ultrawideband antennas*, 1st ed., Artech House, 2005.

[66] M. Simeoni, M.C. Viganó, I. E. Lager, "Open-ended Triangular Waveguide Antenna," in *IEEE Antennas Propagat. Symp.*, pp. 3149-3152 San Diego, CA, USA, Jul.7-11 2008.

[67] B. Steinberg, "The peak sidelobe of the phased array having randomly located elements," in *IEEE Trans. Antennas Propag.*, vol. 20, n. 2, pp. 129–136, Mar. 1972.

[68] B. Strait, "Antenna arrays with partially tapered amplitudes," in *IEEE Trans. Antennas Propag.*, vol. 15, n. 5, pp. 611–617, Sep. 1967.

[69] T. Taylor, "Design of circular apertures for narrow beamwidth and low sidelobes," in *IEEE Trans. Antennas Propag.*, vol. 8, Is. 1, pp. 17–22, Jan. 1960.

[70] *The International System of Units (SI)*,NIST Special Publication 330, 2008 Edition, Barry N. Taylor and Ambler Thompson, Editors.

[71] C. H. Tang, "On a Design Method for Nonuniformly spaced Arrays," *IEEE Trans. Antennas Propag.*, vol. 13, pp. 642–643, Jul. 1965.

[72] G. Toso, P. Angeletti, C. Mangenot, "A Comparison of Density and Amplitude Tapering for Transmit Active Arrays," in *EuCAP 2009*, Berlin, Mar. 23-27 2009.

[73] G. Toso, M.C. Viganó, P. Angeletti, "Null-Matching for the design of linear aperiodic arrays," in *IEEE Antennas Propagat. Symp.*, pp. 3149–3152, Honolulu Hawai USA, Jun.10-15 2007.

[74] N. Toyama, "Optimization of aperiodic array patterns using GA and SDA," in *IEEE Antennas Propag.Symposium 2005*, vol. 2A, pp. 69–72, 3-8 Jul. 2005.

[75] A. Trucco, F. Repetto, "A stochastic approach to optimizing the aperture and the number of elements of an aperiodic array," in *OCEANS '96. MTS/IEEE*, vol.3, pp. 1510–1515, 23–26 Sep. 1996.

[76] H. Unz, "Linear Arrays with arbitrarily distributed elements," *IEEE Trans. Antennas Propag.*, vol. 8, Is.2, pp. 222–223, Mar. 1960.

[77] W. H. Von Aulock, "Properties of phased arrays," in *Proc. IRE*, vol. 48, pp. 1715–1727, 1960.

[78] M. C. Viganó, I. E. Lager, G. Toso, C. Mangenot, G. Caille, "Projection based methodology for designing non-periodic, planar arrays," in *Proc. 38th European Microwave Conference – EuMC*, pp. 1624–1627, Amsterdam, The Netherlands, October 2008.

[79] M.C. Viganó, G. Toso, S. Selleri, C. Mangenot, P. Angeletti, G. Pelosi, "GA Optimized Thinned Hexagonal Arrays for Satellite Applications," in *IEEE Antennas Propagat. Symp.*, pp. 3165–3168, Honolulu Hawai USA, Jun. 10-15 2007.

[80] M.C. Viganó, G. Toso, S. Selleri, C. Mangenot, P. Angeletti, G. Pelosi, "Direct Radiating Arrays for satellite application thinned with Genetic Algorithm," in *29th ESA Antenna Workshop on Multiple Beams and Reconfigurable Antennas*, Apr. 18–20 2007.

[81] M.C. Viganó, M. Simeoni, I.E. Lager, "Radiation properties of array antennas deployed on hexagonal lattices," in *30th ESA Antenna Workshop*, Noordwijk, The Netherlands, May 27-30 2008.

[82] M.C. Viganó, G. Toso, G. Caille, C. Mangenot, I. E. Lager, "Sunflower array antenna with adjustable density taper," in *International Journal of Antenna and Propagat.*, vol. 2009, ID 624035, doi:10.1155/2009/624035.

[83] M.C. Viganó, G. Toso, G. Caille, C. Mangenot, I. E. Lager, "Spatial density tapered sunflower antenna array," in *EuCAP 2009*, Berlin, Mar. 23-27 2009.

[84] J. L. Volakis, *Antenna Engineering Handbook*, 4th ed., New York: McGraw-Hill Companies, 2007.

[85] R. E. Willey "Space Tapering of Linear and Planar Arrays," *IEEE Trans. Antennas Propag.* vol. 10, Is. 4, pp. 369–377, Jul., 1962.

[86] Standard regulation ETSI EN 301.790 in *www.etsi.org*.

[87] Antenna Standards Committee of IEEE Antennas and Propagation Society, "IEEE Standard Definitions of Terms for Antennas," New York: The Institute of Electrical and Electronics Engineers, Inc., 1983.

[88] Computer Simulation Technology, www.cst.com.

Appendix A

Mission requirements

In this appendix the requirements for the antenna under study in this investigation, generating a multi-beam coverage from a geostationary satellite, are presented. Most of this technical data relates to the mission ESA - Domino II and the Thales Alenia Space experience in this field [6, 8, 44, 55]. Aim of the satellite payload is to guarantee the link between a set of terminals and gateways in the field of view of the satellite. The payload, following the DVB-RCS standard for the uplink and the DVB-S for the downlink [86], connects the gateways to the relevant user beams and the different users between themselves.

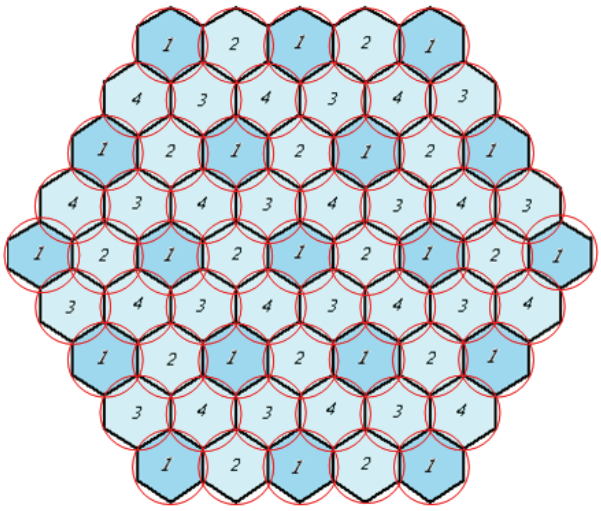

Figure A.1: Scheme of the frequency re-use for the considered application (4 sub-bands indicated by their number 1, 2, 3, and 4).

The frequency band selected for the application is Ka, as the C and Ku, traditionally used for satellite communications, are almost saturated. For this reason the antennas analysed in this investigation are designed to work between 19-20 GHz in transmission (from satellite to Earth) and from 29 to 35 GHz in uplink (from Earth to satellite).

This frequency bandwidth has been divided into 4 sub-bands in order to adopt the well-known 1:4 frequency reuse scheme, as shown in Fig. A.1. In this way it is possible to illuminate all Europe at the same time with spot beams of reduced dimensions (see Table A.1). This results in an increment of the system capacity, at the expense of more stringent requirements to be satisfied in terms of inter-beam isolation.

The classical sub-division of the complete Europe into 64 overlapping beams, based on the frequency re-use scheme discussed, is presented in Fig. A.2.

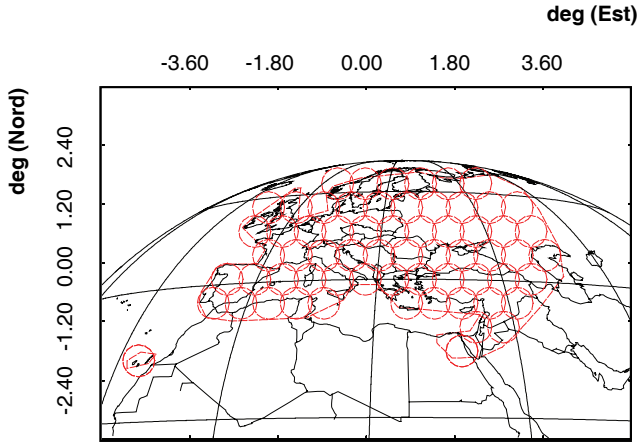

Figure A.2: European multibeam coverage in a 1:4 frequency re-use scheme viewed from a geostationary satellite. The red circles represent the spot to be illuminated; their distances and dimensions are listed in Table A.1.

In this PhD investigation the attention has been focused on Direct Radiating Array for transmitting the signal from the satellite to the user on Earth. In order to use in reception an antenna of reduced dimensions and power, it is usually requested from the TX antenna a high EIRP (as anticipated in Chapter 1). This requirement is represented by the Edge Of Coverage (EOC) value in Table A.1, i.e. the minimum allowed value for the directivity inside the spot beam. For a visual explanation of the EOC quantity reported in Table A.1 and widely used in this investigation, refer

to Fig. A.3. In the same figure, the concept of C/I, has been sketched. Two definitions of the C/I are available in the literature:

- the *C/I single entry* that expresses the ratio between the level of the carrier signal at the EOC and the interfering signal at the same frequency coming just from one of the multiple beams adopting the same frequency.
- The *aggregate C/I* indicates instead the ratio between the carrier signal level and the level of the cumulative interfering signal, taking into account all contributions of the several beams using the same frequency.

In this work the C/I parameter has been converted into an appropriate SLL, as noted in Table A.1.

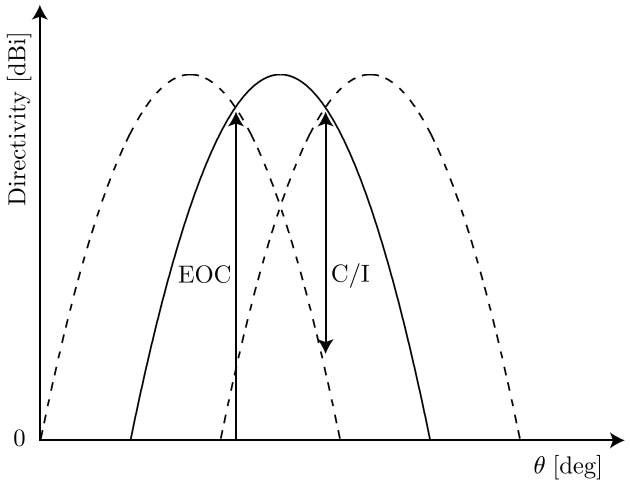

Figure A.3: Definition of EOC and C/I.

From a Geostationary (GEO) satellite, the visible part of Earth can be covered by an angle $\approx 17°$. For this reason, in order to illuminate a limited portion of the Earth, as for example it happens when only Europe or CONUS coverage are needed, the antenna FOV can be further reduced. Hence, the typical choice of inter-element distance equal to $\lambda/2$ can be substituted by a solution characterized by a larger inter-element spacing.

For the analysed ESA mission Domino II [6], the multi-beam coverage is limited to Europe and, since this region is approximately enclosed by a rectangle of sides 8° and 4°, only $\theta \in (-4°, 4°)$ is considered. Therefore, the main objective in the antenna design is to shape the pattern in this

Table A.1: Mission Requirements

Number of spots	64
Spot diameter	0.65°
Inter-spot distance	0.56°
Rx band	29.5 – 30.0GHz
Tx band	19.7 – 20.2GHz
Frequency reuse	1:4
EOC gain	43.8dBi
SLL1 over the interfering areas	20dBi
SLL2 over the Earth	25dBi
SLL3 over the whole visible space	30dBi

limited angular region and avoiding, at the same time, GL occurrence over the complete Earth (see the values of SLL1 and SLL2 in Table A.1). In order to satisfy this last constraint, a maximum inter-element spacing equal to 4 λ, in case of a uniform triangular lattice, is allowed. In this way, the first main lobe replicas (GL) occur at $\theta = 30°$ for $\phi = 0°$ and $\theta = 16.77°$ for $\phi = 90°$, according to Eqs. (2.26) and (2.27).

Appendix B

Side lobe level and Grating lobe level in uniform lattice arrays

In this appendix, a collection of useful properties of the patterns relevant to uniform lattice arrays, are provided. Rectangular, triangular and hexagonal lattice arrays will be hereafter presented and discussed. Firstly some general explanation about the Grating Lobes will be given in the Paragraph B.1, then the pattern characteristics in terms of SLL and GLL will be presented for each of the mentioned regular lattice array configurations.

B.1 Grating Lobes

In an array antenna several elements radiate at the same time resulting in a phased summation of the waves coming from the different radiators. This summation can be destructive in some directions and constructive in other ones. If the inter-element spacing in the array is constant, then the pattern is periodic and several lobes as high as the main beam will appear at locations that depend on the lattice geometry. These high energy lobes, created in directions other than the main lobe one, are denoted as *grating lobes*. Having the same height of the main lobe, the GL can not be distinguished from the main beam, generating, in this way, interferences and energy losses. For these reasons the GL occurrence has to be avoided.

In order to have a better understanding of the GL appearance and positions, it is convenient to introduce the so called *sine plane* or $k_x - k_y$ plane

[77] where $k_x = \sin(\theta)\cos(\phi)$ and $k_y = \sin(\theta)\sin(\phi)$. As easily recognizable from the k_x and k_y definitions, this representation gives a proper handle to describe the bidimensional, discrete Fourier transform of the current distribution. In general, with this representation it is possible to have a clear understanding of the pattern behaviour through its contour plot, not only in the two main planes but in all the directions, even when the beam is pointed away from boresight. The visible region is, in this case, limited to a unit circle: the points inside this disk correspond to angular regions in the visible space, while the ones outside correspond to the invisible space. By increasing the frequency or the inter-element spacing the pattern diagram on the $k_x - k_y$ plane keeps the same behaviour but shrinks, resulting in including more and more pattern inside the visible space area.

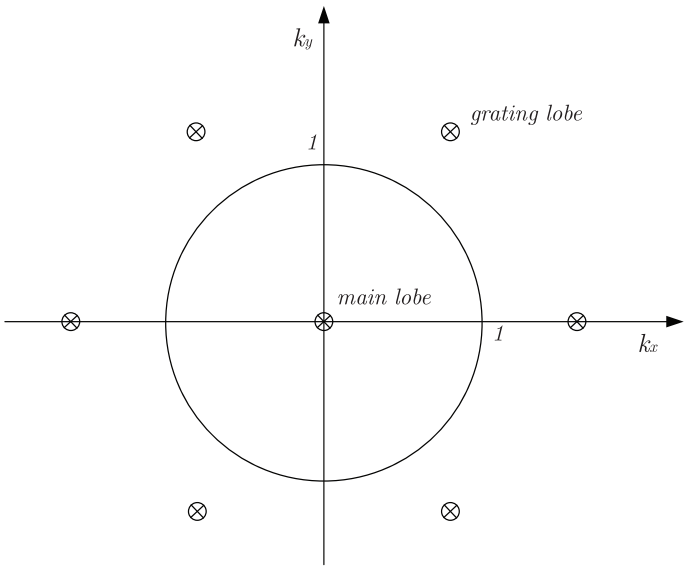

Figure B.1: Main lobe and Grating lobe positions in the k_x and k_y plane.

When the main beam is pointed in a direction different than boresight, the full diagram, except for the unitary circle, rigidly moves in the direction where the beam points. In this way, it may happen that the unit circle encloses GL that were not appearing in the visible space before; this is, for example, the case when the inter-element spacing $\lambda/2 \leq d \leq \lambda$ and a beam scan up to 90° is considered.

With this representation choice the GL appear at positions related to the inverse of the inter-element distances; the larger the spacing along a certain ϕ cut, the closer to the main lobe the GL will occur along that ϕ cut. This can be easily understood by considering $\theta_{\mathrm{GL}} = \sin^{-1}\left(\lambda/\bar{d}_{\phi}\right)$ (see

Eq. (B.3)) where $\bar{d_\phi}$ is the constant spacing of the element projection along a certain ϕ cut.

In order to completely avoid the onset of GL the inter-element distance has to be chosen non-periodic. In this last case, the GL will not appear in the way described before, being the spacing between the samples non-periodic.

B.2 Rectangular lattice array antennas

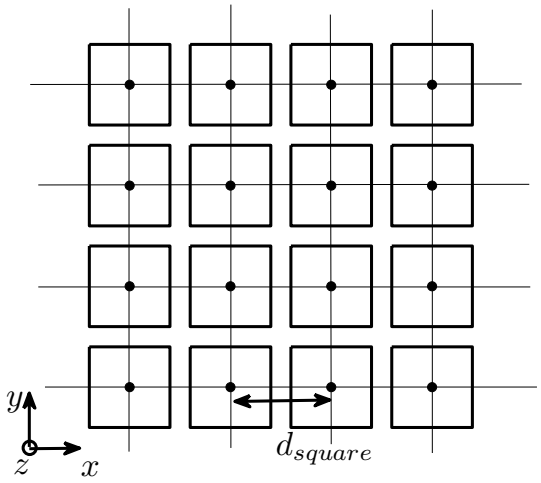

Figure B.2: Square grid array.

In theory, according to [12], just three different uniform lattices are able to subdivide a plane into regular uniform polygons: square, triangular and hexagonal lattices. As the regular square lattice can be regarded as a particular case of the rectangular one for $d_x = d_y = d_{\text{square}}$ (see Fig. B.2), this section will focus on this more general category of array configurations.

Rectangular arrays with rectangular lattices can be seen, as already mentioned in Paragraph 2.3.1, as a linear series of one-dimensional arrays along the Ox or Oy axes (see Fig. B.3). For this reason, in the case of uniform element excitations, the SLL for the ϕ directions $\phi = 0°$ and $\phi = 90°$ is the same as for a linear uniform array, namely about 13 dB under the maximum value [51]. Along all other ϕ directions the SLL is lower, [78]. This can be explained easily by writing the Array Factor AF of the planar array with

elements placed on a rectangular grid as

$$AF(\theta,\phi) = I_0 \sum_{l=0}^{L-1} \exp\left[\mathrm{j}k\left(l\tilde{d_x}\sin(\theta)\cos(\phi)\right)\right] \sum_{m=0}^{M-1} \exp\left[\mathrm{j}k\left(m\tilde{d_y}\sin(\theta)\sin(\phi)\right)\right] \tag{B.1}$$

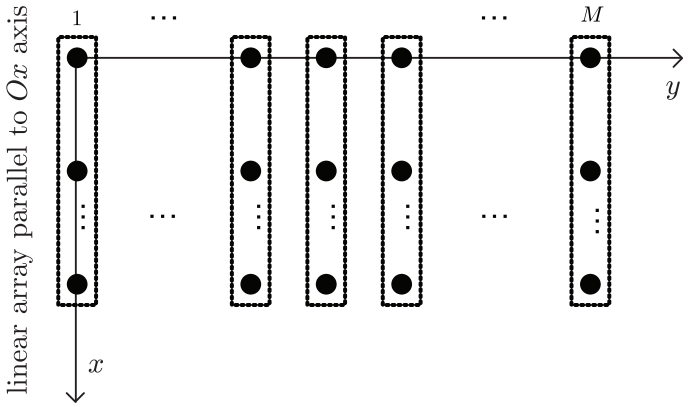

Figure B.3: Planar array as the series of M linear arrays parallel to the x axis.

In this case the excitations have been considered constant with value I_0, but the formula can be used essentially in the same way for an array whose excitations are simply the product of independent amplitude distributions along the two main axes, $I_{lm} = I_l I_m$

$$AF(\theta,\phi) = \sum_{l=0}^{L-1} I_l \exp\left[\mathrm{j}k\left(l\tilde{d_x}\sin(\theta)\cos(\phi)\right)\right] \sum_{m=0}^{M-1} I_m \exp\left[\mathrm{j}k\left(m\tilde{d_y}\sin(\theta)\sin(\phi)\right)\right] \tag{B.2}$$

From Eq. (B.2) it is clear how the SLL along the x and y axes will obey to the eventually imposed amplitude taper laws, respectively I_l and I_m. Along any other generic ϕ cuts $\tilde{\phi}$ the AF will be given by the product of the two AFs corresponding to the two linear (perpendicular) arrays along the main axes x and y in the particular direction $\tilde{\phi}$. From this we can conclude that, on a rectangular grid array, the highest SLL occurs for $\phi = 0°$ or $\phi = 90°$. In the specific case of uniform illumination and rectangular aperture this SLL

is equal to -13 dB, while in the case of circular aperture the SLL is equal to -17 dB [51].

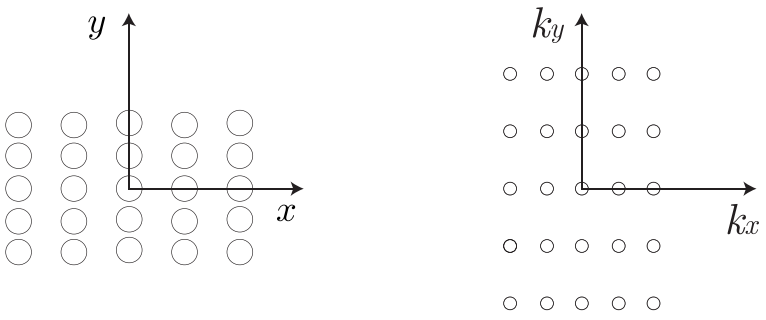

Figure B.4: Element placing on a rectangular grid and corresponding GL positions in the $k_x - k_y$ plane.

In the case of a square spacing d, grating lobes appear at

$$\theta_{\text{GLsquare}} = \sin^{-1}\left(\frac{\lambda}{d}\right). \tag{B.3}$$

When the inter-element distance is different along the Ox and Oy axis, Eq. (B.3) can still be used substituting to d, d_x or d_y.

The same results can be achieved by regarding the rectangular lattice as a particular case of the rhomboidal one, that is the one created by two axes with a generic angle γ between them. In this case, taken the direction of the first axis as ϕ_1 and the direction of the second axis as ϕ_2 , and distances between the elements on the first axis as d_1 and on the second one as d_2, it can be easily demonstrated that GL will occur on planes $\phi = \phi_1 + s_1(90° - \gamma)$ with $s_1 = 1, 2, ...$ at an angular distance θ_{GL1} related to

$$\frac{\tilde{d_1}\sin(\gamma)}{\lambda} = \frac{p_1}{\sin(\theta_0)\cos(\phi_0) - \sin(\theta_{GL1})} \quad p_1 = \pm 1, \pm 2, ... \tag{B.4}$$

and on planes $\phi = \phi_2 + s_2(90° - \gamma)$ with $s_2 = 1, 2, ...$at an angular distance θ_{GL2} related to:

$$\frac{\tilde{d_2}\sin(\gamma)}{\lambda} = \frac{p_2}{\sin(\theta_0)\cos(\phi_0) - \sin(\theta_{GL2})} \quad p_2 = \pm 1, \pm 2, ... \tag{B.5}$$

This notation can be easily applied to triangular lattices as well.

B.3 Triangular lattice array antennas

This lattice (in which the distance between the element is taken to be d_t) can be seen as the superposition of two identical rectangular lattices with element distance along the Ox axis $d_x = \sqrt{3}d_t$ and along the Oy axis $d_y = d_t$. One of the two rectangular, identical lattices is shifted, when compared to the other one, over $\delta_x = \sqrt{3}/2d_t$ along the Ox axis and over $\delta_y = d_t/2$ along the Oy axis. The array pattern can be easily computed, in case of uniform illumination, as the sum of the patterns of the two rectangular grid arrays

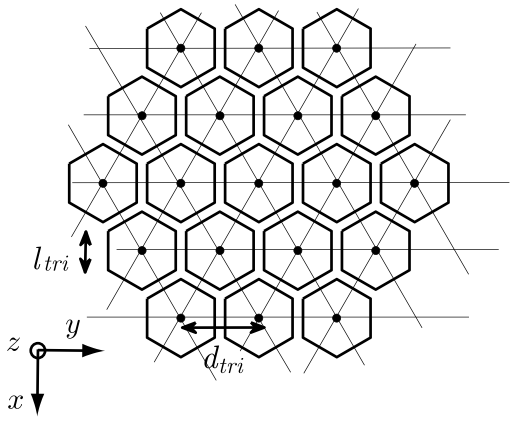

Figure B.5: Triangular grid array.

$$AF(\theta,\phi) = I_0 \sum_{l_1=0}^{L_1} \sum_{m_1=0}^{M_1} \exp\left\{ \mathrm{jk}\left[\mathrm{l_1 \tilde{d}_x} \sin(\theta)\cos(\phi) + \mathrm{m_1 \tilde{d}_y} \sin(\theta)\sin(\phi) \right] \right\}$$
$$+ \sum_{l_2=0}^{L_2} \sum_{m_2=0}^{M_2} \exp\left\{ \mathrm{jk}\left[(\mathrm{l_2 \tilde{d}_x} + \delta_x)\sin(\theta)\cos(\phi) + (\mathrm{m_2 \tilde{d}_y} + \delta_y)\sin(\theta)\sin(\phi) \right] \right\}. \tag{B.6}$$

Even with this lattice configuration, in the specific case of uniform illumination and rectangular apertures (see Fig. B.6) the SLL is equal to -13 dB, while in the case of circular apertures the SLL is equal to -17 dB [51]. As it may be observed in Fig. B.7, this SLL property, already mentioned in the previous section, does not depend on the kind of lattice chosen, but, as long as the lattice is uniform, on the aperture shape only. In the examples considered a rectangular aperture has been populated by isotropic radiators

deployed on a regular triangular lattice. As it appears from Fig. B.7, along the two main ϕ cuts, $\phi = 0°$ and $\phi = 90°$, the radiation pattern behaves in a similar way in terms of SLL.

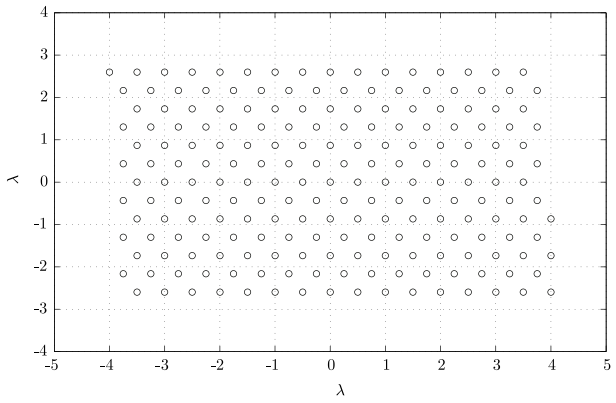

Figure B.6: Element placing on a rectangular aperture, the radiators are deployed on a triangular grid.

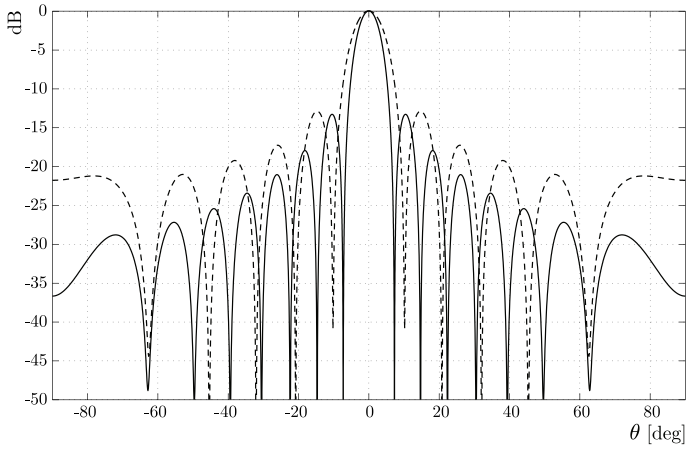

Figure B.7: Pattern of the configuration in Fig. B.6. Continuous line – $\phi = 0°$; dotted line – $\phi = 90°$.

As previously mentioned, when uniform lattices are adopted, the position of the GL is related to the inverse of the inter-element spacing. In this case, the lattice does not change if a rotation around ϕ of 60° is applied; moreover a constant spacing between the elements can be found by projecting the radiators' position along $\phi = 0°, 30°, 60°, \ldots$.

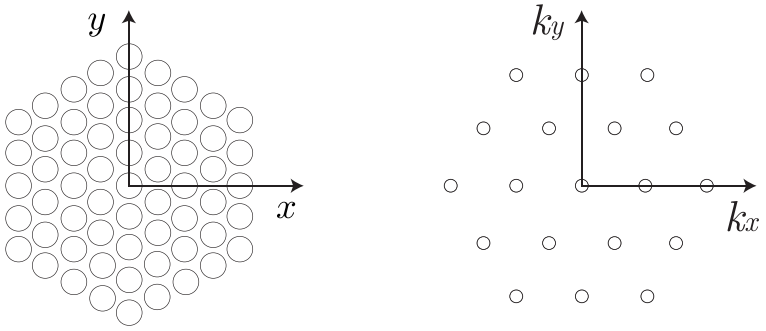

Figure B.8: Element placing on a triangular grid and corresponding GL positions in the $k_x - k_y$ plane.

For these reasons, the positions of the GL are determined by

$$\frac{\tilde{d_t}\sin(60^\circ)}{\lambda} = \frac{p_1}{\sin(\theta_0)\cos(\phi_0) - \sin(\theta_{\mathrm{GL}\ \phi=0^\circ})} \quad p_1 = \pm 1, \pm 2, ... \tag{B.7}$$

$$\frac{\tilde{d_t}\cos(60^\circ)}{\lambda} = \frac{p_2}{\sin(\theta_0)\sin(\phi_0) - \sin(\theta_{\mathrm{GL}\phi=30^\circ})} \quad p_2 = \pm 1, \pm 2, ... \tag{B.8}$$

where (θ_0, ϕ_0) is the direction where the beam is pointing (see [51] p. 184).

The same results can be achieved, as already mentioned in the previous section, by making use of Eqs. (B.4) and (B.5).

B.4 Hexagonal lattice array antennas

Hexagonal lattice arrays are another possible configuration for the complete regular tessellation of the available space. This kind of lattice has not been used frequently in the past because of the shape of the polygon associated to the lattice. In fact, triangular polygons are not easy to be filled by common radiators without significant space losses. If a triangular element is employed in the array, this particular lattice becomes interesting and to has several advantages, as for example a larger available area per polygon, if compared with the rectangular and triangular lattices characterized by the same inter-element distance, potentially increasing the individual antenna gain [66]. As the hexagonal lattice has not been extensively used, the formulation regarding this kind of configuration is not documented in the literature. For this reason the general expression of the radiated field is reported here as well as some details about the GL onset in this type of array antennas.

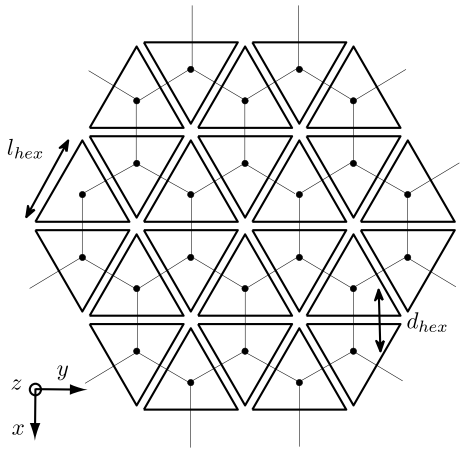

Figure B.9: Example of space sub-division thanks to an hexagonal lattice.

The radiated field can be written for this particular lattice as

$$E(\theta,\phi) = \tilde{f}(\theta,\phi) \sum_{l=0}^{L-1} \sum_{m=0}^{M-1} I_{lm} \exp\left\{ \mathrm{j}k \left[(\mathrm{mod}(m,2) + 4l)\, \tilde{d_x} \sin(\theta)\cos(\phi) + \right.\right. \\ \left.\left. + \; m\tilde{d_y} \sin(\theta)\sin(\phi) \right] \right\} \tag{B.9}$$

where the operator $\mathrm{mod}(q,w)$ gives the reminder of the division q/w and the element identified by the indexes (l,m) is the $(l+1)^{\mathrm{th}}$ radiator along the $(m+1)^{\mathrm{th}}$ column parallel to the Ox axis. The constant spacings d_x and d_y, depicted also in Fig. B.10, are related to the inter-element spacing d_h in such a way that $d_x = d_h/2$ and $d_y = \sqrt{(}3)/2d_h$.

The grating lobe positions can be computed for the x axis by considering the element location projections on the y axis as an array of sub-arrays composed of 2 elements only (see Fig. B.11). As the pattern of the total array would be the multiplication of the pattern of the array and that of the sub-array, grating lobes occur only when both the array and the sub-array patterns exhibit a maximum at the same θ angle. While the sub-array with element distance $d_h/2$ has its own maximum at $\theta_{max\ sub} = \sin^{-1}\left(\frac{\lambda}{d_h/2}\right)$, the inter sub-array distance $3d_h/2$ would cause 3 times more frequent (in the $\sin(\theta)$ domain) maximum peaks. Summarizing, GL appear at

$$\theta_{\mathrm{GLhex}} = \sin^{-1}\left(\frac{\lambda m}{d/2}\right) \quad \text{for } \phi = k60^\circ \,\text{and}\, m = 1,2... \text{ and } k = 1,2,3... \tag{B.10}$$

Their positions are represented by the black dots in Fig. B.12 in the

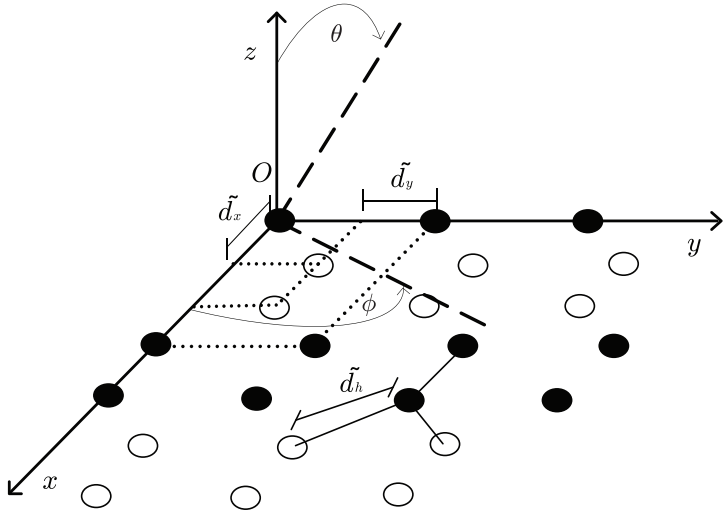

Figure B.10: Side view of the discussed hexagonal lattice array.

$k_x = \sin(\theta)\cos(\phi)$ -$k_y = \sin(\theta)\sin(\phi)$ space. At

$$\theta_{\text{HLhex}} = \sin^{-1}\left(\frac{\lambda n}{3d/2}\right) \quad \text{for } \phi = k60^\circ \text{ and } n \neq 3, 6, 9... \text{ and } k = 1, 2, 3... \tag{B.11}$$

appear high lobes (HL) (represented by grey dots in Fig. B.12), that are the result of the product of the array factor grating lobes and a value of the sub-array factor different from zero or from maximum. At $\phi = k60^\circ$ and for n multiples of 3, case considered in Eq. (B.10), GL will occur both at sub-array and array level resulting in GL for the total array configuration. Along the Oy axis, as it occurs also in the already presented triangular lattice case, the element position projections fall every $d\sqrt{3}/2$ (see Fig. B.11). This results in GL appearing at

$$\theta_{\text{GLhex}} = \sin^{-1}\left(\frac{\lambda}{d\ \sqrt{3}/2}\right) \quad \text{for } \phi = 30^\circ + k60^\circ\ k = 1, 2, 3... \tag{B.12}$$

In Fig. B.12 a visual sketch of the HL and Gl is given; the unitary circle corresponding to the visible region has been plotted as a reference.

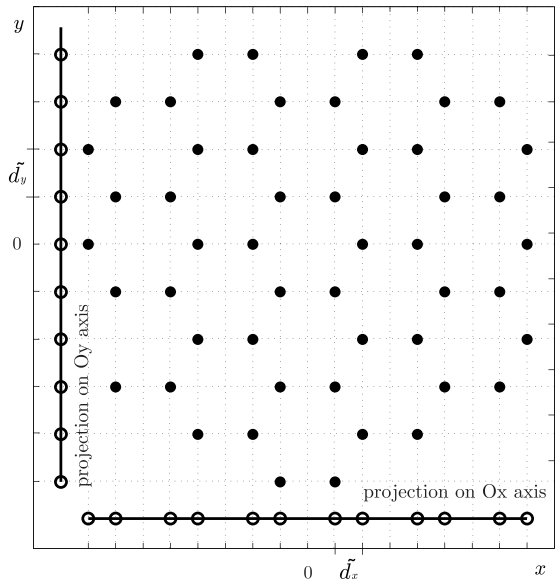

Figure B.11: Element positions and their projections on the coordinate axes.

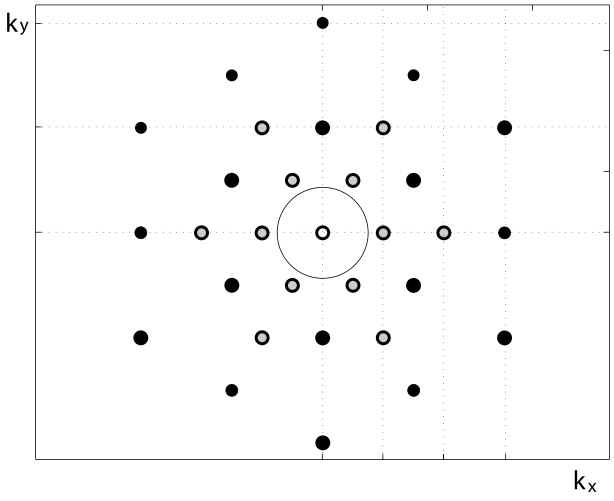

Figure B.12: Grating lobes positions in $k_x k_y$ plane.

Appendix C

Design and optimization techniques

This chapter elaborates on the mathematical details of the different design non-uniform array synthesis techniques that were introduced in Chapter 3.

C.1 Stochastic approaches

Recently, global optimisation algorithms such as Simulated Annealing (SA), Genetic Algorithm (GA), Particle Swarm Optimisation (PSO) have become more and more popular in every research field, the array antenna optimisation included. In view of its wide use in antenna engineering, this section will mainly focus on the discussion of GA techniques.

C.1.1 Simulated Annealing

As in most of the stochastic optimisation methods, the idea of SA comes from the natural world: liquid water becomes ice, heals, through a cristallization process in which the system is in every moment almost in a situation of thermo-dynamic equilibrium. A system state is chosen to be the next one if its energetic level is less then the one of the previous ice crystal configuration. In an analogous way, the algorithm selects a new antenna configuration if the value of the cost function is less than the one characterizing the previous configuration [5, 75].

C.1.2 Particle Swarm Optimization

PSO is an optimization technique developed for the first time in 1995 [40]. It is a method quite similar to GA but based on the information sharing in a group of animals. The animal population, in this case, collaborate in order to find the best solution by sharing the info about their personal best location found and the global one of the swarm [62].

C.1.3 Genetic Algorithms

GA are related to a mathematical model based on the natural selection and reproduction principles. This kind of computation models were known already in the Sixties [19], but it was in 1975 with Holland's book [28] that they were used for the first time not for solving a specific problem but as a tool to optimize a generic class of problems. The aim of Holland's method is to evolve an initial random population according to laws belonging to the natural world in order to find the global optimum. As in biology it is well known that some genetic sequences are better than other, i.e. with higher probability of survival and reproduction, in the same way some individuals of a population are considered better in terms of a fitness function, compared to others.

Before describing the principal characteristics and the operations involved by GA, it is useful to introduce and explain some terminology directly imported from the vocabulary of biology.

- Chromosome: It represents a possible solution of the problem, assimilated to an element of the population. It is usually coded by means of transforming the relevant information into a string of bits. In the case of an array whose elements just have two possible states (on or off), it represents a particular binary configuration of the array element alimentations.

- Population: It is a set of chromosomes, hence a set of possible solutions. The population will change and "improve" at each generation.

- Gene: It is one bit or a small set of adjacent bits that code the single variables in the chromosome. In an array whose excitations are just ones or zeros, they correspond to the amplitudes of the different radiators, being zero for the switched off elements, and one for the active ones.

- Generation: Each iteration of the algorithm is called generation; during this process the chromosomes of the population evolve.

- Parents: Some chromosome, among the best ones according to a fitness function, are chosen at each generation to mate and create in this way new chromosomes, usually called children.

- Cross-over: It is the mating action used by parents to combine their genes and create new chromosomes.

- Mutation: As it happens in the real world, a gene can, with a low probability, change without apparent reasons. In the case considered hereafter this would lead to a simple inversion between one and zero or vice versa. More in general, the gene changes in a different one.

- Elitism: A procedure to prevent the lost of the best individuals of a generation, an effect that is statistically possible due to cross-over and mutation. With this procedure the best individuals of each generation are compared with the best ones of the previous generation. If the old ones are better than the worst individuals of the new generation, the new ones are deleted and the best ones of the old generation are preserved in the new generation. If elitism is adopted, the cost function value will monotonically decrease (or increase) at every generation.

Several versions of the GA exist, but most of them contain some common basic steps. These fundamental steps are listed in Fig. C.1.3. The first step of the algorithm, even before the initializations of the population, is the coding. A proper choice of the code will render the algorithm faster and more efficient. Usually a binary code is chosen, but this is not a rule. If the parameter to be coded is not discrete, then the choice of a proper number of bits to represent the parameters is really important for preventing significant quantization errors. In the case for which this GA was designed the antenna feeding can only assume two values, zero or one and, for this reason, the binary code has been chosen.

The most important step in the algorithm shown in Fig. C.1.3 is the definition of a cost function, a law that gives the possibility to determine the suitability of a particular configuration. From a genetic point of view, this value expresses the capability of a certain individual of the generation to survive and procreate. From an antenna-point of view it expresses how well a particular configuration satisfies the imposed requirements. It is obvious that, as the choice of the cost function will strongly affect the results, this step of the algorithm is of particular importance. In the case of the GA

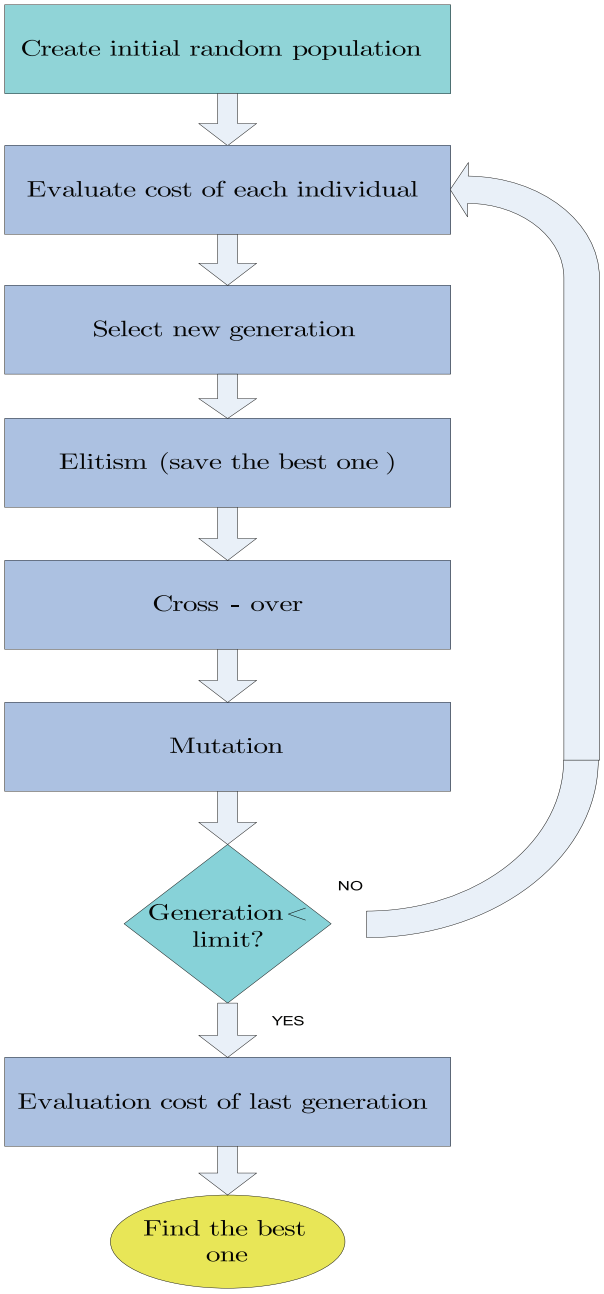

Figure C.1: Flow Chart scheme of the Genetic Algorithm

under study, the cost function was expressed as

$$f_{cost} = a_1 f_1 + a_2 f_2 + a_3 f_3 + a_4 f_4 \tag{C.1}$$

in which f_1 evaluates the difference between the effectively obtained and the prescribed directivity at the EOC D_{EOC}, i.e. 43.8 dBi; f_2 and f_3 measure the exceeding of the SLL D_{20} with respect to the prescribed SLL for $D_{\max} - 20$ in the close interfering and the far beams, respectively; and f_4 takes into account the total number of elements switched on N_{on} over the possible total number of elements deployed on the aperture N_{tot}.

$$f_1 = b_1^{43.8-D_{\mathrm{EOC}}} \tag{C.2}$$

$$f_2 = b_2^{D_{20}-(D_{\max}-20)} \tag{C.3}$$

$$f_3 = b_3^{D_{20}-(D_{\max}-20)} \tag{C.4}$$

$$f_4 = b_4^{N_{on}/N_{tot}} \tag{C.5}$$

The weighting coefficients $a_1, a_2\ a_3\ a_4$ and $b_1, b_2\ b_3\ b_4$ are empirically selected for ensuring a good compromise between the four assessed features. By changing them it is possible to modify the cost function and, in this way, achieve different array configurations.

C.2 Null matching procedure

The aim of this synthesis technique is to design a non-uniform array in such a way that its nulls occur at prescribed angles. Firstly, the technique has been applied to replicate a reference linear Dolph-Chebyschev array pattern [14]; then it has been extended to the planar case. As known, the array factor for a symmetric linear array composed of an even number of element, may be expressed in a series of cosine terms

$$AF(\theta) = 2\sum_{k=1}^{N/2} a_k \cos\left[\frac{2\pi}{\lambda} x_k \sin(\theta)\right] \tag{C.6}$$

where a_k and x_k represent the excitation of the k-th pair of elements and its coordinate, respectively. In the case of using an odd number of radiators in the array it is possible to apply the same procedure by expressing the array factor as

$$AF(\theta) = 1 + 2\sum_{k=1}^{(N-1)/2} a_k \cos\left[\frac{2\pi}{\lambda} x_k \sin(\theta)\right]. \tag{C.7}$$

For a Dolph-Chebyschev array the null positions are

$$\theta_p = 2\cos^{-1}\left\{\frac{\cos\left[\pi/2(2p-1)/(N-1)\right]}{\cosh\left[\cosh^{-1}(\mathrm{SLL})(N-1)\right]}\right\} \quad p = 1, 2...N-1 \tag{C.8}$$

where SLL represents the sidelobe level. Imposing the array factor of the unknown, equally-fed, non-uniform array equal to zero at the positions of the nulls of the pattern of the Dolph-Chebyshev array, one obtains

$$2\sum_{k=1}^{N/2}\cos\left[2\pi\frac{x_k}{\lambda}\sin(\theta)\right] = 2\sum_{k=1}^{N/2}c_k\cos\left[\pi\left(\frac{2k-1}{2}\right)\sin(\theta_p)\right] \quad p = 1, 2...N-1 \tag{C.9}$$

Solving (C.9) amounts to deriving the locations x_k of the non-uniformly spaced array elements. The mathematical problem may turn out to be ill-posed and the system of real transcendental equations represented by (C.9) may not admit real solutions.

For this reason, the exact solution of (C.9) is replaced by a minimization problem aiming at determining the best approximation of the exact solution, this minimization problem being more robust and numerically stable. The target optimization function is taken to be the maximum deviation (in terms of the absolute value) of the sparse array pattern from the zero-crossing condition at the angular positions corresponding to the nulls of the target Dolph-Chebyshev array. This cost function is minimized with a vectorial min-max optimization defined by the expression

$$\min_{[x_1,\ldots,x_M/2]}\max_p\left|\sum_{k=1}^{N/2}\cos\left[2\pi\frac{x_k}{\lambda}\sin(\theta_p)\right]\right| \tag{C.10}$$

This technique is particularly useful when the synthesis aims at designing a linear array with deep nulls in the pattern or specific values at given angular locations.

C.3 Perturbative technique

Another interesting category of synthesis techniques is the pertubative one. In general, under this category are grouped methods that, starting from a given configuration, slowly arrives to an optimal one by varying the element positions in the array with small increments at each step.

The method hereby presented has been developed for linear non-uniform arrays and it has been mostly used by the author in conjunction with the null-matching technique. Starting from the positions found with the previously described algorithm it was possible to find, in a fast and accurate way, the best solution that is close to the initial one. This synthesis algorithm can also be used alone, starting from a uniform configuration. However, in this case larger computational times or a reduced accuracy has to be considered, and more care should be placed at the imposed objective values of the pattern.

By making use of Eqs. (C.6) and (C.7), a square matrix can be written by imposing the value of the AF to be equal to some assigned values at N/2 particular θ angles.

$$2\sum_{n=1}^{N/2}\cos\left[\frac{2\pi}{\lambda}d_n\sin(\theta_t)\right] = 2\sum_{n=1}^{N/2}\cos(X_{n,t}) = W_t, \quad \text{for } t = 1,\ldots,N/2, \tag{C.11}$$

Then, considering that

$$\cos(\gamma) = \cos(\alpha) - \sin(\alpha)(\gamma-\alpha) \quad \text{for}\gamma \to \alpha \tag{C.12}$$

every term of the matrix $\cos(X_{n,t})$ can be expressed as

$$\cos(X_{n,t}) = \cos(\alpha_{n,t}) - \sin(\alpha_{n,t})(X_{n,t} - \alpha_{n,t}) \tag{C.13}$$

where

$$X_{n,t} - \alpha_{n,t} = \frac{2\pi}{\lambda}\sin(\theta_t)(d_n - d_{n,\mathrm{ITER}}) = \frac{2\pi}{\lambda}\sin(\theta_t)\Delta_n. \tag{C.14}$$

The proposed synthesis techniques finds in an iterative fashion the position d_n from the one at the previous step $d_{n,\mathrm{ITER}}$ by inverting the discussed matrix. At each step it has to be ensured that Δ_n is a small value. In case it is not, in order to apply rigorously the method, the terms W_t have to be chosen not too different from the values of the pattern at the given angle θ_t of the configuration at the previous step. These values W_t can be modified during the routine.

C.4 Array synthesis using the Auxiliary Array Function

In this section, emphasis is put on another analytical design technique aimed at the synthesis of a linear array having a prescribed array factor.

C.4.1 Auxiliary Array Function

Let us first consider the array factor of a antenna consisting of N_a radiators deployed over a line

$$AF(\vartheta) = \sum_{n=1}^{N_a} \bar{A}_n e^{j(k_0 \bar{x}_n \sin\vartheta + \bar{\alpha}_n)}, \tag{C.15}$$

with k_0 denoting the propagation constant in free space, and $\bar{I}_n = \bar{A}_n e^{j\bar{\alpha}_n}$ the excitation coefficient (amplitude and phase) of the $n-$th antenna located at $x = \bar{x}_n$. As it can be readily inferred, the expression in (C.15) may be regarded as the Riemann sum approximating the integral auxiliary array function defined as

$$F_A(\vartheta) = \int_0^{q_{\max}} A(q)\, e^{j[2\pi\xi(q)\sin\vartheta + \alpha(q)]} dq \tag{C.16}$$

where $\xi(q)$, $A(q)$, $\alpha(q)$ are the continuous normalized positioning, amplitude and phase functions, respectively, generalizing the discrete quantities $\bar{x}_n$, $\bar{A}_n$, $\bar{\alpha}_n$ appearing in (C.15). Similarly, q is the continuous version of the index n relevant to antenna elements forming the array, ranging from 0 to a suitable maximum value $q_{\max}$. After setting for shortness $\psi = 2\pi\sin\vartheta$, the auxiliary array function is re-written as

$$F_A(\psi) = \sum_{m=1}^{M} F_{A_m}(\psi), \tag{C.17}$$

with

$$F_{A_m}(\psi) = \int_{q_{m-1}}^{q_m} A_m(q)\, e^{j[\psi\xi_m(q) + \alpha_m(q)]} dq \tag{C.18}$$

being the contribution relevant to the $m-$th interval $[q_{m-1}, q_m]$. In each of the M intervals the continuous normalized positioning, amplitude and phase functions are assumed to be linearized according to the following expressions

$$\begin{bmatrix} \xi_m(q) \\ A_m(q) \\ \alpha_m(q) \end{bmatrix} = \begin{bmatrix} \hat{\xi}_{m-1} \\ \hat{A}_{m-1} \\ \hat{\alpha}_{m-1} \end{bmatrix} + \frac{q - q_{m-1}}{\Delta q} \begin{bmatrix} \widehat{\Delta\xi}_m \\ \widehat{\Delta A}_m \\ \widehat{\Delta\alpha}_m \end{bmatrix} \tag{C.19}$$

where $\hat{\beta}_m = \beta(q_m)$, $\widehat{\Delta\beta}_m = \hat{\beta}_m - \hat{\beta}_{m-1}$ for $\beta = \xi, A, \alpha$, and $\Delta q = q_m - q_{m-1} = q_{\max}/M$. As it can be easily inferred, the larger the number M of

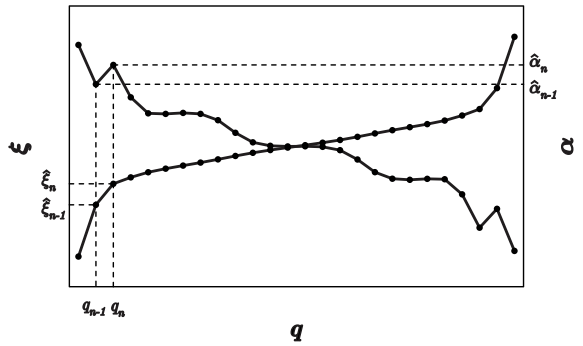

Figure C.2: Piecewise linear approximation of the normalized positioning $\xi(q)$ and phase $\alpha(q)$ functions. The same discretization procedure is applied to the amplitude function $A(q)$, not shown here for sake of clearness.

intervals dividing the domain $[0, q_{\max}]$, the better will be the accuracy of the described discretization procedure on the positioning, amplitude and phase functions.

It is straightforward to show that, under the considered assumptions, the general term $F_{A_m}(\psi)$ can be evaluated in a closed form as follows

$$\begin{aligned} F_{A_m}(\psi) = \frac{\Delta q}{\left(\psi\widehat{\Delta\xi}_m + \widehat{\Delta\alpha}_m\right)^2} \Big[& e^{j\left(\psi\hat{\xi}_m+\alpha_m\right)} \Big\{ \Big[1 + \\ & - j\left(\psi\widehat{\Delta\xi}_m + \widehat{\Delta\alpha}_m\right) \Big] \hat{A}_m - \hat{A}_{m-1} \Big\} + \\ & - e^{j\left(\psi\hat{\xi}_{m-1}+\alpha_{m-1}\right)} \Big\{ \hat{A}_m - \Big[1 + j\left(\psi\widehat{\Delta\xi}_m + \right. \\ & \left. + \widehat{\Delta\alpha}_m\right) \Big] \hat{A}_{m-1} \Big\} \Big]. \end{aligned} \tag{C.20}$$

To derive a fully analytical formulation, aimed at mimicking the objective array factor mask $F_O(\psi)$, it is convenient to carry out the synthesis procedure directly in the Fourier transform domain $\mathcal{F}\{\cdot\}$. By making judicious use of the shift property of the operator $\mathcal{F}\{\cdot\}$, one can readily obtain

$$\begin{aligned} \tilde{F}_{A_m}(H) = \mathcal{F}\{F_{A_m}(\psi)\} = \int_{-\infty}^{+\infty} F_{A_m}(\psi)\, e^{j\psi H} d\psi = \\ = \left|\tilde{F}_{A_m}(H)\right| e^{j \arg\left\{\tilde{F}_{A_m}(H)\right\}} \end{aligned} \tag{C.21}$$

where

$$\left|\tilde{F}_{A_m}(H)\right| = 2\pi\Delta q \frac{\hat{A}_{m-1}\left(H+\hat{\xi}_m\right) - \hat{A}_m\left(H+\hat{\xi}_{m-1}\right)}{\widehat{\Delta\xi}_m^2} \cdot \cdot P_{\widehat{\Delta\xi}_m}\left(H+\hat{\xi}_{m-\frac{1}{2}}\right) \tag{C.22}$$

$$\arg\left\{\tilde{F}_{A_m}(H)\right\} = \left[\hat{\alpha}_{m-1} - \frac{\widehat{\Delta\alpha}_m}{\widehat{\Delta\xi}_m}\left(H+\hat{\xi}_{m-1}\right)\right] \cdot P_{\widehat{\Delta\xi}_m}\left(H+\hat{\xi}_{m-\frac{1}{2}}\right) \tag{C.23}$$

$P_\Delta(H)$ denoting the pulse distribution having the width Δ and centered at the origin $H = 0$. It is worth noting that, by virtue of the proper piece-wise linearization of the continuous normalized positioning, amplitude and phase functions, each term $F_{A_m}(\psi)$ is Fourier-transformed into a function with compact support centered at $H = -\hat{\xi}_{m-\frac{1}{2}} = -\left(\hat{\xi}_{m-1}+\hat{\xi}_m\right)/2 = -\left(\hat{\xi}_{m-1}+\widehat{\Delta\xi}_m/2\right)$ and having the width $\widehat{\Delta\xi}_m$. By observing that the supports of the modulated pulse functions $\tilde{F}_{A_m}(H)$ are not overlapping, it is evident that the following equality holds true

$$\left|\tilde{F}_A(H)\right| = \left|\sum_{m=1}^{M}\tilde{F}_{A_m}(H)\right| = \sum_{m=1}^{M}\left|\tilde{F}_{A_m}(H)\right|. \tag{C.24}$$

A similar property is featured by the argument $\arg\left\{\tilde{F}_A(H)\right\}$ of the Fourier-transformed auxiliary function. Thanks to this, as it will be shown in the next paragraph, the proposed array synthesis technique turns to be rigorous and straightforward without resorting to any optimization procedure.

C.4.2 Evaluation of the Array Tapering Functions

The array synthesis is carried out by enforcing $\tilde{F}_A(H) = \tilde{F}_O(H)$ or, equivalently, $\tilde{F}_{A_m}(H) = \tilde{F}_O(H)$ in each interval $H \in \left[-\hat{\xi}_m, -\hat{\xi}_{m-1}\right]$ with $m = 1, 2, \ldots, M$. This implies that

$$\int_{\hat{\xi}_{m-1}}^{\hat{\xi}_m}\left|\tilde{F}_O(-H)\right|dH = \int_{\hat{\xi}_{m-1}}^{\hat{\xi}_m}\left|\tilde{F}_{A_m}(-H)\right|dH =$$

$$= 2\pi\int_{q_{m-1}}^{q_m}A_m(q)\,dq = \pi\Delta q\left(\hat{A}_{m-1}+\hat{A}_m\right) \tag{C.25}$$

where the continuous amplitude function $A(q)$ is assumed to be greater than or equal to a given threshold $A_{\min} \geq 0$. Besides, to address a possible physical constraint regarding the minimal inter-element spacing $d_{\min}$, an additional condition is to be imposed on the first derivative of the normalized positioning function $\xi(q)$, namely

$$\xi'(q) \geq \xi'_{\min} = \frac{N_a}{q_{\max}} \frac{d_{\min}}{\lambda_0} \tag{C.26}$$

with $\lambda_0 = 2\pi/k_0$ being the free-space wavelength. As it can be noticed, the array synthesis relies on the solution of the Eq. (C.25), involving the unknown quantities $\hat{\xi}_m$ and $\hat{A}_m$ in a sequential way, starting from the given values $\hat{\xi}_0$ and $\hat{A}_0 = A_{ref} \geq A_{\min}$. In order to meet the afore-mentioned requirement, the following parameter depending on the assigned mask $\tilde{F}_O(H)$ and the minimal normalized inter-spacing $\widehat{\Delta\xi}_{\min} = \xi'_{\min}\Delta q$ is evaluated for each index m

$$L_m = \int_0^{\widehat{\Delta\xi}_{\min}} \left| \tilde{F}_O\left(-H - \hat{\xi}_{m-1}\right) \right| dH. \tag{C.27}$$

In the case when L_m is larger than the amplitude-related threshold, the spacing $\widehat{\Delta\xi}_m$ is taken to be exactly $\widehat{\Delta\xi}_{\min}$ and a suitable amplitude tapering has to be enforced in such a way that Eq. (C.25) is satisfied. That is the case for

$$\hat{A}_m = -\hat{A}_{m-1} + \frac{1}{\pi\Delta q} L_m. \tag{C.28}$$

If $L_m < \pi\Delta q \left(\hat{A}_{m-1} + \hat{A}_{\min}\right)$ the amplitude coefficient $\hat{A}_m$ can be taken equal to the reference value A_{ref}, and the normalized position $\hat{\xi}_m$ is derived by solving the following equation

$$\int_{\hat{\xi}_{m-1}}^{\hat{\xi}_m} \left| \tilde{F}_O(-H) \right| dH = \pi\Delta q \left(\hat{A}_{m-1} + A_{ref}\right). \tag{C.29}$$

In this case, the spacing $\widehat{\Delta\xi}_m$ turns out to be larger than $\widehat{\Delta\xi}_{\min}$, resulting in a mask-driven sparseness of the array. The solution of Eq. (C.29) can be obtained using any analytical or numerical method. As it can be noticed, the balanced combination between amplitude and positioning tapering is strongly affected by the requirement on the minimal inter-spacing $d_{\min}$, as well as on the required number N_a of antenna elements.

Once the piecewise linear approximation of the positioning distribution is derived, the phase quantities $\hat{\alpha}_m$ can be easily evaluated by en-

forcing $\arg\left\{\tilde{F}_A(H)\right\} = \arg\left\{\tilde{F}_O(H)\right\}$ or, equivalently, $\arg\left\{\tilde{F}_{A_m}(H)\right\} = \arg\left\{\tilde{F}_O(H)\right\}$ in each node $H = -\hat{\xi}_m$, thus obtaining via Eq. (C.23)

$$\hat{\alpha}_m = \arg\left\{\tilde{F}_O\left(-\hat{\xi}_m\right)\right\}, \text{ for } m = 1, 2, \ldots, M \tag{C.30}$$

Let us now focus on the selection of the parameter $\hat{\xi}_0$. To this end, a suitable energy criterion can be conveniently adopted by determining the value $\hat{\Xi}_0 > 0$ satisfying

$$\int_{-\hat{\Xi}_0}^{\hat{\Xi}_0} \left|\tilde{F}_O(H)\right|^2 dH = \kappa \int_{-\infty}^{+\infty} \left|\tilde{F}_O(H)\right|^2 dH \tag{C.31}$$

with $\kappa < 1$ being a given threshold affecting the accuracy of the proposed synthesis procedure. Besides, in case the maximum array aperture is requested to be $D_{\max}$, the mentioned parameter can then be taken as

$$\hat{\xi}_0 = \min\left\{\hat{\Xi}_0, \frac{D_{\max}}{2}\right\}. \tag{C.32}$$

If no requirements on the maximum array size are provided, $\hat{\xi}_0$ can be readily selected as $\hat{\Xi}_0$.

Finally, the quantities $\bar{x}_n$ and $\bar{A}_n$, $\bar{\alpha}_n$ appearing in the expression of the array factor in (C.15) can be computed in a straightforward manner by uniformly sampling the relevant normalized positioning, amplitude and phase functions respectively in the points

$$Q_n = \left(n - \frac{1}{2}\right)\frac{q_{\max}}{N_a}, \tag{C.33}$$

with $n = 1, 2, \ldots, N_a$.

It is pointed out that the proposed technique features an excellent versatility in handling array design problems with given constraints on both the maximum aperture dimension and the minimum inter-element spacing with no need for any optimization procedure.

Appendix D

Spirals: Fermat and Fibonacci spirals

Spirals are one of the most common regular shapes in nature: from the snail shell, to the sunflower seed placement (see Fig. D.1), to the Milky way arms. Different kinds of spirals are known in the literature. Using a spiral placement for the elements of a planar array guarantees a good spreading of the energy associated to the side and grating lobes. Furthermore, a spiral lattice permits obtaining a quite uniform filling of a given aperture compared to other planar lattices like the ones organized in rings.

A well known spiral is the Fermat spiral (Fig. D.2) which has the property of enclosing equal areas within every turn. Its equation can be expressed in polar coordinates as:

$$\rho = a\sqrt{\phi'} \tag{D.1}$$

where ρ is the distance from the spiral center, and ϕ' is the angle that identifies the point position with respect to the x axis; the parameter a controls the distance between the spiral turns.

This spiral is quite often found in nature. In particular, there are leafs and seeds whose positions can be obtained by sampling a Fermat spiral equation, i.e.

$$\rho = \sqrt{n}b \tag{D.2}$$

$$\phi' = \frac{2\pi n}{c} \tag{D.3}$$

and when it is important having a uniform subdivision of the space the parameters b and c are closely related to the Golden Ratio , also known as

Figure D.1: Picture of a sunflower; the placement of the seeds in the central part is according to the discussed Fermat spirals.

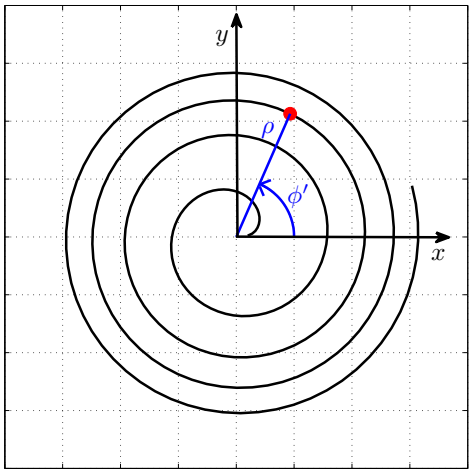

Figure D.2: The Fermat spiral and its associated coordinate system.

Fibonacci number since it represents the solution of the Fibonacci quadratic equation. For instance, the leaves around the stem use this positioning to share in an optimal way the space and the light [1].

The Fibonacci sequence is known since 1202 A.D. thanks to Leonardo son of Bonaccio from Pisa and his book Liber Abaci. This sequence has been widely analyzed and applied in different fields: from the description of particular plants to computer science, from crystallography to electrical engineering. By solving the Fibonacci quadratic equation [15]:

$$\beta^2 A_n = \beta A_n + A_n \tag{D.4}$$

the following two roots are obtained

$$\beta_1 = \frac{\sqrt{5}+1}{2} = \tau \tag{D.5}$$

$$\beta_2 = \frac{1-\sqrt{5}}{2} = -\frac{1}{\tau}. \tag{D.6}$$

In most of the applications the first value has been used, but to characterize the spiral both of them are usable. The divergence angle, also referred to as the golden angle, is defined as

$$golden\ angle = \frac{360^\circ}{\beta_1^2} = 360^\circ - \frac{360^\circ}{\beta_2^2}. \tag{D.7}$$

Because this value is irrational, it is impossible to have two or more elements in the spiral array characterized by the same ϕ angle. The element packing result to be efficient. Interesting Fermat spirals could be also the ones with other irrational coefficients like $\sqrt{2}$. In the patent [4] β_1 is used for the element disposition along the spiral according to the formulation presented in Eqs. (4.1) and (4.2). As it can be easily noticed, the positions of the elements in the sunflower array depend only on n via a trivial equation.

The second type of spirals employed in this study is the Fibonacci one, namely a particular kind of logarithmic spiral, where the ratio between radii evaluated at each 90° degrees is related to the golden ratio number. It is interesting to note that in a sunflower array configuration, when the elements are placed on a Fermat spiral at every β_1 degrees, the elements form a set of clockwise and one of anti-clockwise Fibonacci spirals (see Figs. D.3 and D.4). The numbers of spirals belonging to the two sets are two consecutive terms of the Fibonacci series as it can be appreciated by counting the clockwise spirals in Fig. D.3 and the anticlockwise ones in Fig. D.4, 5 and 8, respectively. Another particular characteristic of this configuration is that the number of spirals in each set is exactly related to which of the Fermat spiral element have to be connected to create the set of Fibonacci spiral. As example, it is possible to note how the first of the 5 spirals in the first set in Fig. D.3, is created by connecting the elements with numbers 1, 6, 11, 16 and 21, whose relative difference is again 5.

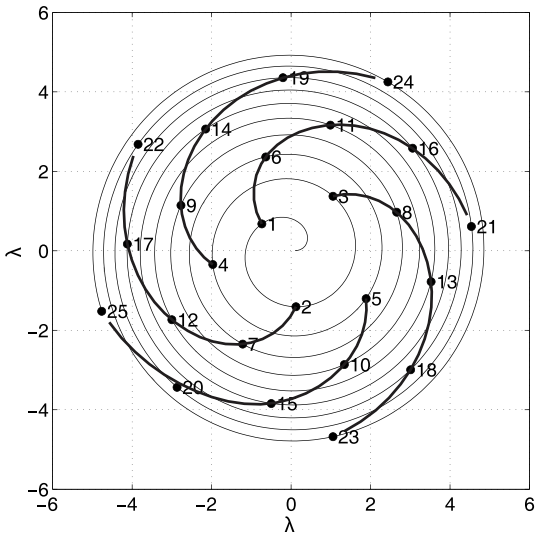

Figure D.3: Clockwise Fibonacci spirals.

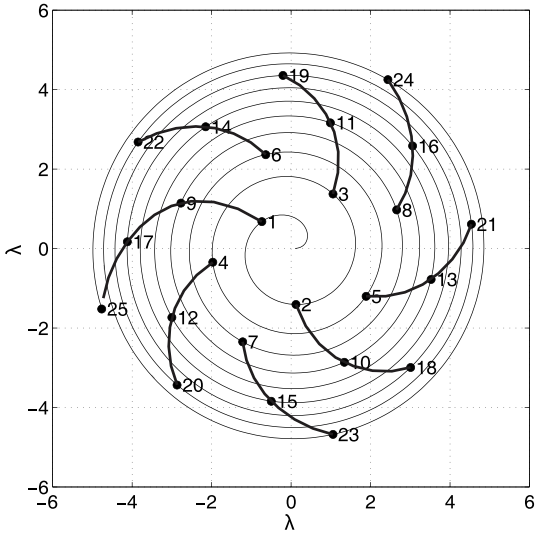

Figure D.4: Anti-clockwise Fibonacci spirals.

Appendix E

Taylor amplitude distribution

This appendix discusses briefly the well known Taylor amplitude taper law that was extensively used in this dissertation as reference distribution. By imposing weights on the element excitations according to the Taylor distribution, it is possible to shape the radiation pattern of a linear, uniform array and obtain a predefined SLL. The Taylor synthesis technique starts from considering the position of the nulls in the array radiation pattern. In order to achieve a lower SLL, the first $\bar{n}-1$ zeros in the $\sin(\theta)$ domain, hereafter indicated as z_n, $n=1,\ldots,\bar{n}-1$, are substituted by the first $\bar{n}-1$ zeros of the Chebyschev polynomial and, in this way, moved away from the main lobe. This results in a lower level of the side lobes and in an increment of the main beam width. The number $\bar{n}$ controls how many of the side lobes are modified by the synthesis.

The use of the Taylor tapering starts by imposing the required SLL that is then employed for evaluating the parameter

$$B = 1/\pi \cosh^{-1}\left[10^{\mathrm{SLL_{dB}}/20}\right] \tag{E.1}$$

where $\mathrm{SLL_{dB}}$ denotes the SLL expressed in dB. The positions of the new nulls then follow as

$$z_n = \frac{\bar{n}\sqrt{B^2+(n-0.5)^2}}{\sqrt{B^2+(\bar{n}-0.5)^2}} \quad \text{for } n=1,2,..,\bar{n}-1 \tag{E.2}$$

and the corresponding array AF [51] reads

$$\mathrm{AF}(z,B,\bar{n}) = \frac{\sin(\pi z)}{\pi z}\prod_{n=1}^{\bar{n}-1}\frac{1-z^2/z_n^2}{1-z^2/n^2}. \tag{E.3}$$

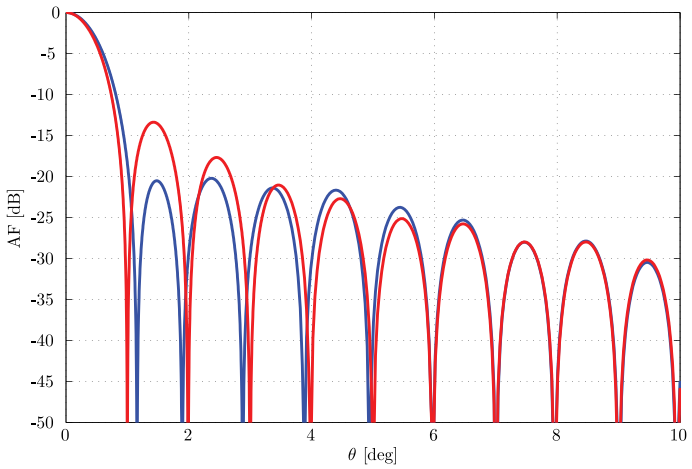

Figure E.1: Array factor of an array with uniform amplitude distribution – red line, Taylor distribution ($\bar{n}$=6, SLL=20) – blue line.

For understanding the effect of the Taylor tapering, Fig. E.1 presents a comparison between the normalized array factors of two uniformly spaced arrays, one with uniform illumination (red line) and the other with a Taylor tapered one (blue line), the amplitude tapering being evaluated considering $\mathrm{SLL_{dB}} = 20\,\mathrm{dB}$ and $\bar{n} = 6$. The plot clearly evidences the shifting of the nulls, the reduction of the maximum SLL and the modification of the beam width in the case of the amplitude tapered array.

Figure E.2 illustrates the effect of the choice for the $\mathrm{SLL_{dB}}$ and $\bar{n}$ parameters on the Taylor amplitude tapering. Two cases are examined, starting from a reference taper calculated for $\bar{n}$=6 and $\mathrm{SLL_{dB}} = 20\,\mathrm{dB}$ (the red curve in Fig. E.2). Firstly, by keeping the $\mathrm{SLL_{dB}}$ constant, increasing the number of modified nulls $\bar{n} - 1$ results in an amplitude distribution that is no longer monotonically decreasing when moving from the center, the amplituded increasing towards the aperture edges as suggested by the green arrow in Fig. E.2. If the distribution is then replicated by means of a non-uniform array, the element density toward the edges will increase accordingly. Secondly, by maintaining $\bar{n}$ fixed, increasing the desired $\mathrm{SLL_{dB}}$ results in an increasingly steep amplitude variation, indicated by the cyan arrow in Fig. E.2. This corresponds to a larger variation in the amplitude values range and, when the distribution is used as a reference for achieving the locations of an equivalent non-uniform array, it results into a larger difference between the minimum and the maximum inter-element spacing.

It is now clear that a proper choice of the two parameters is fundamental for the design of an easily implementable array.

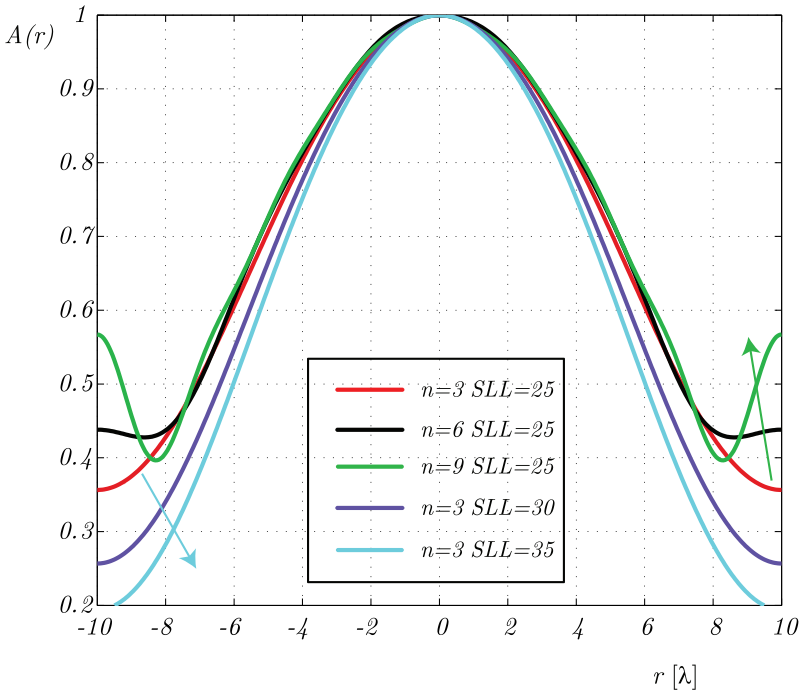

Figure E.2: Taylor amplitude distribution for different SLL and $\bar{n}$.

This technique has been extended by Taylor [69] to the case of a planar circular array by considering the new null positions as

$$z_n = \frac{\mu_{\bar{n}}\sqrt{B^2 + (n-0.5)^2}}{\sqrt{B^2 + (\bar{n}-0.5)^2}} \tag{E.4}$$

where $\mu_{\bar{n}}$ are the natural nulls of the $J_1(\pi z)/(\pi z)$ function. In this case the total array factor can be expressed as [51]

$$\mathrm{AF}(z, B, \bar{n}) = 2\frac{J_1(\pi z)}{\pi z}\prod_{n=1}^{\bar{n}-1}\frac{1 - z^2/z_n^2}{1 - z^2/\mu_{\bar{n}}^2}. \tag{E.5}$$

A study of the behaviour of the aperture amplitude distribution could be conducted in this case as done before for the linear distribution case and it would lead to the same conclusions.

Appendix F

Patch design

Hereafter the elementary radiator used for the simulation of the configurations presented in Paragraph 4.4 will be shortly introduced and discussed. All the results presented have been obtained with the commercial software CST (Computer Simulation Technology) [88].

F.1 Radiator design

In view of a possible sub-array implementation, in which the feeding line is deployed on a different layer with respect to the several radiators, the feeding architecture for the presented antenna has been selected to be a suspended stripline.

The radiator, working in a frequency band centered at 10 GHz, will provide a right hand circular polarization.

The radiator consists of a metal square with side length 5.9 mm with two of the opposite edges being cut, as shown in Fig. F.1, in order to create the proper phase shift between the field components and, consequently, to obtain the desired polarization. A Roger RO4003 high frequency circuit material with a thickness of 1.524 mm and a dielectric constant $\epsilon_r = 3.66$ is used as substrate.

Figure F.2 shows the S11 parameter in the frequency band of interest. It is possible to notice that the presented radiator is well matched in a bandwidth of about 0.75 GHz.

The radiating patch is enclosed in a cavity created by several metal pins. In this way the coupling between two neighbouring elements can be

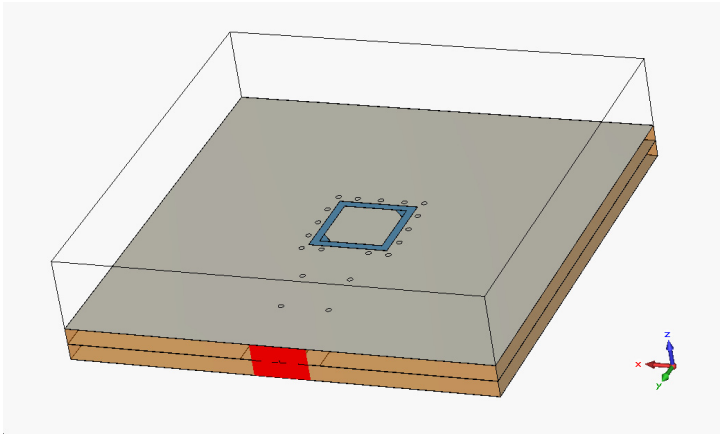

Figure F.1: Perspective view of the patch antenna.

reduced and, at the same time, it is possible to reduce the patch dimension. Thanks to the cavity, the substrate choice and to the selected feeding structure, the lenght of the patch side could be reduced up to about $\lambda_0/5$. As a result, the presented patch could be efficiently included in an array environment with stringent space requirements where the elements need to be closely packed together.

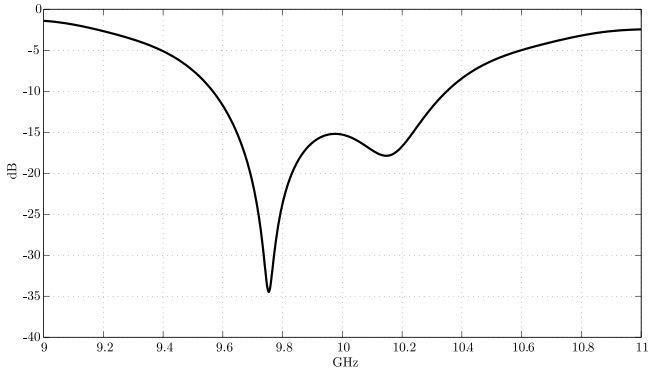

Figure F.2: S11 parameter of the proposed antenna.

The axial ratio between the two field components and their phase difference are shown in Fig. F.3. The plot demonstrate that, in the FOV, the radiation replicates with good accuracy the circular polarization that was aimed at.

Finally the patch directivity is shown in Fig. F.4. It is characterized by a maximum of 7.4 dBi and by a almost flat behavior of the directivity values

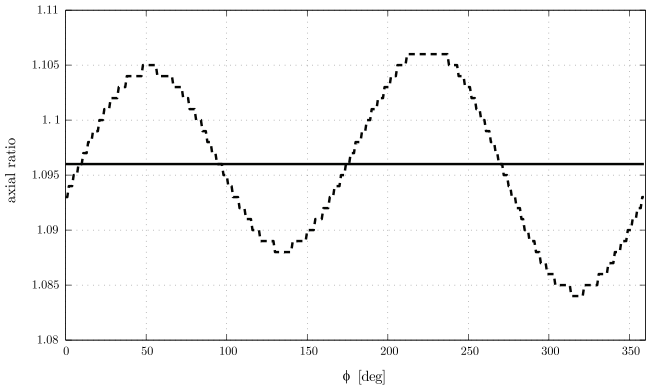

Figure F.3: Axial ratio of the proposed patch antenna for $\theta = 0°$ – continuous line , $\theta = 4°$ – dotted line.

in the first theta degrees, corresponding in Paragraph 4.4 to the considered FOV.

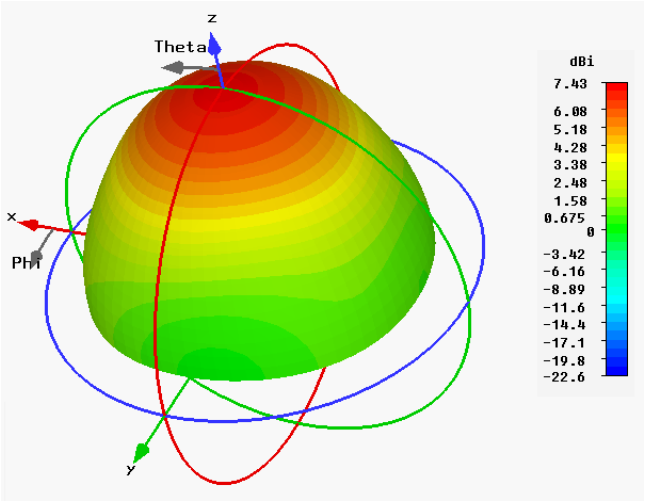

Figure F.4: Directivity pattern of the square patch in Fig. F.1.

Summary

Saving space on board, reducing costs and improving the antenna performances are tasks of outmost importance in the field of satellite communication. In this work it is shown how a non-uniformly spaced, direct radiating array designed according to the so called '*sunflower*' law is able to satisfy stringent requirements with a reduced number of active chains, all employing amplifiers working at the same, optimised, operation point.

The aim of this PhD thesis is to identify several array configurations characterized by a reduced complexity and cost when compared with conventional arrays or to reflector configurations. These arrays must satisfy stringent requirements of a GEOstationary satellite communication mission, especially in terms of a minimum directivity to be guaranteed in several spot beam areas and sidelobe levels to be kept below an assigned value.

The dissertation starts with the discussion of the pattern characteristics of regularly spaced array. Since regularly spaced arrays do not allow pattern shaping without making use of an amplitude distribution, non-uniformly spaced arrays are introduced and their pattern behaviour is discussed at length. These arrays are proven to offer the freedom for shaping the pattern according to the imposed requirements and, at the same time, avoid the occurrence of grating lobes. Several innovative techniques for designing this particular class of arrays are proposed and compared.

Among them, the *sunflower* positioning technique is chosen as the best candidate to deterministically design non-uniform planar arrays with really low sidelobe levels and a good rotational symmetry of the radiation patterns. This simple technique is based on the application of two separate laws for finding the radial and angular element positions. The first one comes directly from the relation established in the thesis between the amplitude distribution law and the density distribution one. Regarding the angular positioning law, the concept of optimal angular spreading, inherited from the natural world, is applied to the *sunflower* array antenna in order to guarantee the sparsity of the element positions both in the radial and angular coordinates.

This angular sparsity is achieved by ensuring that each element of the array is placed at a different angular position. The *sunflower* synthesis technique is then generalized for employing differently sized sub-arrays in the same aperture. Two different options are presented, in which the sub-arrays composing the *sunflower* array have the same amplitude or the same power. In the first one, the planar aperture is divided into convex cells associated with the spatial locations obtained by means of the *sunflower* positioning. These cells are then filled with the best fitting (regular) sub-arrays. In this sense, several shapes are experimented with, ranging from circular ones to some that present clear technological advantages. In the latter case, the selected sub-arrays may induce a slight alteration of the rigorous *sunflower* placement. However, the easier technological implementation makes them the preferred choice for the design of the large planar array that is able to satisfy the satellite mission requirements.

In order to physically validate the positioning principle of the *sunflower* array antenna, a demonstrator at a scaled frequency has been manufactured and measured. Four different sub-arrays are assembled starting from a standard 4x4 square, circularly polarized tile, and their radiation patterns are superimposed in order to compute the total array radiated pattern. Measurements and simulated results are shown to be in very good agreement.

The dissertation attests the *sunflower* placement technique as an innovative, successful, deterministic method for designing large arrays. This technique can be complemented with a modular sub-array design, the combination of the two yielding an effective instrument for implementing highly demanding antennas, such as those required by satellite communication applications.

Samenvatting

Ruimtebesparing aan boord, kostenverlaging en antenne prestatieverbetering zijn de meest belangrijke taken in satelliet communicatie. In dit werk wordt getoond hoe een direct-stralende apertuur bestaande uit een niet-uniform verdeeld antenne stelsel en ontworpen naar het zogenaamde 'Zonnebloem' model, het mogelijk maakt aan strenge voorwaarden te voldoen waarbij het aantal actieve structuren beperkt blijft en alle gebruikte versterkers zijn ingesteld op het zelfde geoptimaliseerde werkingspunt. Het doel van dit proefschrift is om verschillende array configuraties, gekenmerkt door gereduceerde complexiteit en beperking in kosten, te onderscheiden en te vergelijken met conventionele arrays of met reflector configuraties. De array configuraties moeten aan de strenge voorwaarden van een GEO-stationaire Satelliet communicatiemissie voldoen, met name de minimale bundelende werking (directiviteit) in de verschillende nauwe antenne bundels (spot beams) moet worden gegarandeerd en de maximale waarden van de zijlussen moeten aan vooraf gestelde eisen voldoen. De dissertatie begint met de bespreking van stralingsdiagram kenmerken van een uniforme array. Omdat deze arrays geen diagram modellering toestaan zonder gebruik te maken van een amplitude verdeling, worden niet-uniforme arrays gentroduceerd en hun diagram gedrag uitvoerig bediscussieerd. Deze arrays hebben bewezen een extra vrijheidsgraad te geven om het diagram te modelleren volgens de opgelegde voorwaarden en tegelijkertijd ongewenste bundels (zogenaamde grating lobes) te voorkomen. Verschillende innovatieve technieken voor het ontwerp van deze specifieke groep arrays worden voorgesteld en besproken. Zo is de techniek waarbij antenne elementen worden geplaatst conform het 'Zonnebloem' model verkozen als het beste concept om op deterministische wijze niet-uniforme, vlakke arrays te ontwerpen die stralingsdiagrammen hebben met lage zijlussen en goede rotatiesymmetrie. Deze eenvoudige techniek is gebaseerd op de toepassing van twee verschillende wetten voor het vinden van de radiale en hoek element posities. De eerste komt direct uit de relatie, ontwikkeld in the thesis, tussen de wet die de amplitude verdeling beschrijft en de wet voor de dichtheidsverdeling. Met betrekking tot de

wetmatigheid van de hoek positionering wordt het concept van maximale hoekspreiding, zoals die ook voortkomt in de natuur, toegepast op de 'Zonnebloem array' antenne om zorg te dragen voor de schaarste van element posities in zowel de radiale als hoek cordinaten. Deze hoek schaarste wordt bereikt door te verzekeren dat ieder element van de array wordt geplaatst op een verschillende hoekpositie. De 'Zonnebloem synthese' techniek wordt dan gegeneraliseerd door het opstellen van in grootte verschillende sub-arrays in dezelfde apertuur. Twee verschillende oplossingen worden gepresenteerd, waarin de sub-arrays, die de uiteindelijke 'Zonnebloem array' bepalen, of dezelfde amplitude of hetzelfde vermogen hebben. In de eerste situatie is de vlakke apertuur verdeeld in convexe cellen geassocieerd met de ruimtelijke locaties, welke zijn verkregen door middel van de 'Zonnebloem' positionering. Deze cellen worden vervolgens gevuld met de best passende reguliere sub arrays. Op deze wijze kan met verschillende vormen worden gexperimenteerd, varirend van circulair tot vormen die technologische voordelen hebben. In de tweede situatie kunnen de geselecteerde sub-arrays leiden tot een kleine wijziging van de strikte 'Zonnebloem' plaatsing. Echter de eenvoudige technologische implementatie zorgt ervoor dat de tweede situtatie de voorkeur heeft voor het ontwerp van een grote, vlakke array die het mogelijk maakt aan alle voorwaarden te voldoen die een satelliet missie vereist. Om daadwerkelijk fysiek het positionering principe van de 'Zonnebloem array' te valideren is een demonstratiemodel op een geschaalde frequentie vervaardigd en gemeten. Vier verschillende sub-arrays zijn geassembleerd beginnend bij een standaard, circulair gepolariseerde 4x4 vierkante tegel. De stralingsdiagrammen van de sub-arrays worden gebruikt om het totale stralingsdiagram te kunnen berekenen. Metingen en gesimuleerde resultaten worden getoond en zijn in goede overeenstemming met elkaar. Het proefschrift getuigt ervan dat de 'Zonnebloem' plaatsingstechniek een innovatieve, succesvolle, deterministische methode is voor het ontwerpen van grote arrays. Deze techniek kan worden gecompleteerd met een modulair sub-array ontwerp. De combinatie van deze twee leveren een effectief instrument voor de implementatie van antennes die moeten voldoen aan strikte voorwaarden, zoals gesteld bij satelliet communicatie applicaties.

Acknowledgements

Few hours from leaving The Netherlands and starting a new life this seems the most appropriate time to write some acknowledgments. I'm sorry if in the rush of the last moment I am forgetting to mention somebody.

I'd like to start by thanking Dirk-Jan, for his amazing love and his constant caring presence that makes me so confident for the future. I'm also grateful for all the support that I always get from my family, even if they live quite far away I can always count on them.

I would like to thank the friends in Leiden that in these years were my second family. Annalisa, without you and your phone calls my days will be a bit sad and empty. Mariel, Salvatore, Giorgio, Caroline, Francesca, Valerio, Filippo and Ilaria, thanks for all the wonderful moments, dinners and games we had together.

A special thanks goes also to all the members of the 'presidential' family, thanks for bringing so much happiness in the dutch grey days.

I also want to mention here the Seido Karate group that always enspired me to continue my training of mind, body and spirit.

Surely I cannot forget about my 'forever-lasting' friends in Florence, Valentina A., Luisa, Silvia, Valentina G. and Camilla, thanks to you I really know what friendship is and what it means to miss someone.

I'm also grateful to my friends and colleagues from Delft: Simone, Alex, Dana, Massimiliano, Francesco, Tim, Jordi, Amer and many others, in particular my office mate Pascal for being always so patient and helpful, Yann for his friendship that goes much behond the paranimf duties, and Diego for being the proof that there is still hope in the world of research.

For their professional and personal help I'd like to thank my many supervisors. I'm particularly thankful to Prof. Ligthart and Dr. Roederer for making possible and believing in this PhD, Gerard Caille for his support and caring especially during my period at Thales and Cyril Mangenot for

his constant presence in my academic life.

Special thanks go to Giovanni Toso for these 5 years of enthusiastic and stimulating guidance and for introducing me to the world of satellite antennas.

Finally I'd like to thank Hansi Lager for his advises and help in writing this thesis, his honesty (a quality not to be underestimated in this world) and his special sense of humor.

About the Author

M.Carolina Viganó was born in Florence, Italy the 15th February 1982. She completed her master degree study with the Engineering University of Florence in April 2006, with a mark of 110 *cum laude*. The final master degree project was carried out at the European Space Agency in The Netherlands (September 2005 – March 2006), and resulted in the master degree thesis "Optimization of thinned array antennas for multi-beam coverage". After the successfull period as stagiaire she continued her research at ESA as Young Graduate Trainee in the Antenna Section, mainly involved in the research of flat top sub-arrays and array synthesis techniques. After one year she accepted a position as contractor with Moltek as Antenna Engineer at ESA. In September 2007 she started a PhD on satellite antennas at the Technical University of Delft, financially supported by Thales Alenia Space France and ESA ESTEC. During the last three years she has been working mainly on analytical array synthesis techniques for the designing of non-regular array architectures. Several important results have been presented in journal papers and at international conferences. She is currently working for JAST, ViaSat researching on phased planar array antennas for satellite mobile terminals.

Author's pubblications

Journal and book

1. M. C. Viganó, G. Toso, G. Caille, C. Mangenot, I. E. Lager, "Sunflower array antenna with adjustable density taper," in *Int. Journal of Antenna and Propagation*, vol. 2009, ID 624035, doi:10.1155/2009/624035.

2. M. C. Viganó, C. Mangenot, G. Toso, G. Caille, A.G. Roederer, I.E. Lager, L.P. Ligthart "Sunflower Antenna: synthesis of sparse planar arrays for satellite applications," in *WiSE End Symposium*, Wassenaar,

4 March 2010.

3. D. Caratelli, M. C. Viganó, "Analytical Synthesis Technique for Uniform Amplitude Linear Sparse Arrays,", submitted to *Radio Science*

4. D. Caratelli, M. C. Viganó, "A Novel Deterministic Synthesis Technique for Constrained Sparse Array Design Problems," submitted to *Transactions on Antennas and Progations*

Conference papers

1. M. C. Viganó, G. Toso, S. Selleri, C. Mangenot, P. Angeletti, G. Pelosi, "Thinned hexagonal arrays for satellite application optimized with genetic algorithm," in *VI edition of the Mediterranean Microwave Symposium and Italian National Meeting on Electromagnetics (XVI RiNEm)*, Genova, Italy, Sept. 2006.

2. M. C. Viganó, G. Toso, S. Selleri, C. Mangenot, P. Angeletti, G. Pelosi, "GA Optimized Thinned Hexagonal Arrays for Satellite Applications,", in *IEEE Antennas and Propagation Symposium pp. 3165–3168*, Honolulu Hawai USA, Jun. 10–15, 2007.

3. G. Toso, M. C. Viganó, P.Angeletti, "Null-Matching for the design of linear aperiodic arrays," in *IEEE Antennas and Propagation Symposium pp. 3165–3168*, Honolulu Hawai USA, Jun. 10–15, 2007.

4. M. C. Viganó, G. Toso, G. Pelosi, S. Selleri, "Ottimizzazione di Array Snelliti per Applicazioni Satellitari," presented at *XIII giornata di Studio sullIngegneria delle Microonde*, Fisciano, Salerno, 14–15 May 2007.

5. G. Toso, M. C. Viganó, C. Mangenot, A. G. Roederer, "Recent Work at ESA-ESTEC on Array Synthesis for Space Applications," in *IEEE Antenna and Propagation, Benelux Chapter*, Delft, the Netherlands, 18 Oct. 2007.

6. G. Caille, I. Lager, L. P. Ligthart, C. Mangenot, A. G. Roederer, G. Toso, M. C. Viganó, "Aperiodic Arrays for Multiple Beam Satellite Applications," in *11th International Symposium on Microwave and Optical Technology*, Monte Porzio Catone, Italy, 17–21 Dec. 2007.

7. C. Mangenot, G. Toso, M. C. Viganó, A. G. Roederer, "Non-periodic Direct Radiating Arrays for Multiple Beam Space Telecommunication Missions," in *IEEE Antennas Propagation Symposium* pp. 3149–3152, San Diego, CA, USA, Jul.7–11 2008.

8. M. Simeoni, M. C. Viganó, I. E. Lager, "Open-ended Triangular Waveguide Antenna," in *IEEE Antennas Propagation Symposium*, pp. 3149–3152, San Diego, CA, USA, Jul.7–11 2008.

9. M. C. Viganó, I. E. Lager, G. Toso, C. Mangenot, G. Caille, "Projection based methodology for designing non-periodic, planar arrays," in *European Microwave Week*, Amsterdam, The Netherlands, Oct. 27–31, 2008.

10. M. C. Viganó, G. Toso, G. Caille, C. Mangenot, I. E. Lager, "Spatial density tapered sunflower antenna array," in *European Conference on Antennas and Propagation* 2009, Berlin, Mar. 23–27 2009.

11. M. C. Viganó, G. Caille, G. Toso, C. Mangenot, I. E. Lager, "Sparse planar array synthesis technique for satellite applications,", in *IEEE Antennas Propagation Symposium* 2010, Toronto, 11–17 July 2010.

12. M. C. Viganó, D. Caratelli, "Analytical Synthesis Technique for Uniform Amplitude Linear Sparse Array", in *IEEE Antennas Propagation Symposium* 2010, Toronto, 11-17 July 2010.

13. M. C. Viganó, G. Toso, P. Angeletti, I.E. Lager, A. Yarovoy, D. Caratelli, "Sparse Antenna Array for Earth- Coverage Satellite Applications," in *European Conference on Antennas and Propagation* 2010, Barcelona, 12–16 April 2010.

14. M. C. Viganó G. Caille, C. Mangenot, I. E. Lager, G. Toso, "Sunflower Sparse Array for space applications: from design to manufacturing," in *European Conference on Antennas and Propagation* 2010, Barcelona, 12–16 April 2010.

Other conference/workshop contributions

1. M. C. Viganó, G. Toso, S. Selleri, C. Mangenot, P.Angeletti, G. Pelosi, "Direct Radiating Arrays for satellite application thinned with Genetic Algorithm," in *29th ESA Antenna Workshop on Multiple Beams and Reconfigurable Antennas*, Noordwijk, The Netherlands, Apr. 18–20, 2007.

2. M. C. Viganó, G. Toso, P.Angeletti, "Null-Matching for the synthesis of sparse arrays," in *29th ESA Antenna Workshop on Multiple Beams and Reconfigurable Antennas*, Noordwijk, The Netherlands, Apr. 18–20, 2007.

3. M. C. Viganó, G. Toso, C. Mangenot, "Direct Radiating Array with Quasi-Flat-Top Pattern Sub-array," in *29th ESA Antenna Workshop on Multiple Beams and Reconfigurable Antennas*, Noordwijk, The Netherlands, Apr. 18–20, 2007.

4. M. C. Viganó, "Direct Radiating arrays with quasi-flat-top pattern Sub-arrays," *Tech. Report TEC-EEA/2006.108MCVI*,ESA ESTEC, Noordwijk, The Netherlands, Feb. 2007.

5. M. C. Viganó, M. Simeoni, I.E. Lager, "Radiation properties of array antennas deployed on hexagonal lattices," in *0th ESA Antenna Workshop on Antennas for Earth Observation, Science, Telecommunication and Navigation Space Missions,*, Noordwijk, The Netherlands, May 27–30 2008.

6. M. C. Viganó, I. E. Lager, G. Caille C. Mangenot, G. Toso, "Sunflower array for multi-beam applications,", in *32nd ESA Antenna Workshop on Antennas for Space Applications*, Noordwijk, The Netherlands, Oct. 5–8 2010.

7. D. Caratelli, M. C. Viganó, G. Toso, P. Angeletti, "Analytical Placement Technique for Sparse Arrays,", in *32nd ESA Antenna Workshop on Antennas for Space Applications*, Noordwijk, The Netherlands, Oct. 5–8 2010.

Glossary

AF	Array Factor, 33
$A_{\mathbf{sub}_n}$	Amount of amplitude at the single elementary radiator in the n^{th} sub-array, 63
$A_{\mathbf{tot,sub}_n}$	Total amount of amplitude at the n^{th} sub-array, 63
$C_{n,m}$	Coupling coefficient, 24
D	Directivity, 26
$\mathcal{D}_M$	maximum directivity, 30
E	Electric Field, 29
FNBW	First-Nulls BeamWidth, 26
G	Gain, 27
HPBW	Half-Power BeamWidth, 26
$I_l m$	alimentation of the element with indexes l m in the planar array antenna, 35
I_n	excitation of the n^{th} antenna, 29
K_n	Amount of current enclosed by the radii R_{n-1} and R_n, 54
N	Total number of sub-arrays, 58, 63
$\bar{N}_n$	Number of elementary radiators composing the n^{th} sub-array, 63
$P_{\mathbf{in}}$	Input power, 24
$P_{\mathbf{rad}}$	Power radiated, 24
$P_{\mathbf{sub}}$	Power fed to the n^{th} sub-array, 63
U	Radiation intensity, 26
R_{ap}	Radius of the available antenna aperture, 53
a_n	module of the excitation of the n^{th} antenna, 30
d_n	distance of the n^{th} element from the origin O, 21
$\tilde{d}_x$	distance between two elements on the x axis, 34

$\tilde{d}_y$	distance between two elements on the y axis, 34
f	frequency, 21
f_n	element factor of the n^{th} antenna, 29
α_n	phase of the n^{th} antenna, 30
η	efficiency, 24
θ	angle from the axis z and the plane xOy, 21
ϕ	angle from the axis x to the projection of the direction of observation on the plane xOy, 21

Index

BFN, 13

C/I, 123
CONUS, 12

DRA, 14, 107

EIRP, 15
EOC, 122

FAFR, 12
FOV, 71, 158

GA, 41, 42, 138
GL, 15, 36, 37, 39
Golden Ratio, 51, 149

HPA, 13, 43

IRCTR, 19

LHCP, 28

Null-matching procedure, 44, 141

Patch antenna, 65, 82, 84, 105, 157
Perturbative technique, 46, 142
PSO, 41, 138

RHCP, 28

SLL, 31, 36, 39, 55, 127, 130, 142
Spiral, 52, 53, 149
Sub-array, 5, 58, 61, 82, 93, 94, 96

Thinning, 43